CHATTER DETECTION AND PREVENTION IN HIGH-SPEED MILLING

A Dissertation presented to the Faculty of the Graduate School
University of Missouri

In Partial Fulfillment
Of the Requirement of the Degree

Doctor of Philosophy

---

by
JOSEPH KENNEDY

Dr. Roger Fales, Dissertation Supervisor

MAY 2011

ACKNOWLEDGEMENTS

I would like to thank my advisor and committee chair Dr. Roger Fales for his contribution to this research. Dr. Fales has mentored me throughout my Graduate career, and this dissertation would not have been possible without his guidance and contributions. I would also like to thank my committee members Dr. Kluever, Dr. El-Gizawy, Dr. Smith, and Dr. Chicone for their time, advice, and assistance in obtaining my Doctorate. Finally, I would like to thank all faculty and staff in the Mechanical and Aerospace Department that have made my colligate career as memorable and enjoyable as it has been.

TABLE OF CONTENTS

LIST OF ILLUSTRATIONS

Figure **Page**

LIST OF TABLES

Table **Page**

NOMENCLATURE

Symbol	Description
a	acceleration of the tool tip [m/s^2]
$\boldsymbol{a}$	position and velocity of one element
$\boldsymbol{A}$	matrix defining the discrete time system for TFEA stability analysis
b	depth of cut [m]
$\boldsymbol{b}$	vector of b values [m]
b_c	current depth of cut [m]
$b_{desired}$	desired current depth of cut [m]
b^*	depth of cut at which a bifurcation occurs [m]
$\boldsymbol{B}$	matrix defining the discrete time system for TFEA stability analysis
c	damping of the tool/spindle = $c_{x,y}$ [N-s/m]
c_{est}	estimate of the damping of the tool/spindle [N-s/m]
$c_{x,y}$	damping of the tool/spindle in the x and y-directions [N-s/m]
$\boldsymbol{C}$	matrix of damping values in the x and y directions
d	distance from the stability bound for the control system to change Ω
df	incremental feed rate (feed rate per time step) [m]
dt	time step = 1e-6 sec
D	diameter of the tool = 1.27×10^{-2} m
$\boldsymbol{D}$	matrix defining the discrete time system for TFEA stability analysis
E	Young's Modules [GPa]
f	feed rate [m/rev]

f_i .....initial feed rate = 1.27×10^{-4} m/rev

F_h.....experimental force signal from the hammer test [N]

$\boldsymbol{F}$, $\boldsymbol{L}$, $\boldsymbol{H}$, $\boldsymbol{M}$.....partial derivative matrices of the Kalman filter equations

F_c .....resultant cutting force [N]

F_n .....normal cutting force [N]

F_{np} .....normal cutting force for p^{th} tooth [N]

F_t .....tangential cutting force [N]

F_{tp} .....tangential cutting force for p^{th} tooth [N]

F_x.....cutting force in the x-direction [N]

F_y.....cutting force in the y-direction [N]

g_p .....step function for the p^{th} tooth

h.....radial immersion = 3.81×10^{-4} m

h_n .....lip depth [m]

i .....length w = 1 or 4

I .....Moment of inertia [m^4]

j .....length of v = 1

k.....stiffness of the tool/spindle = $k_{x,y}$ [N/m]

k_{est}.....estimate of the stiffness of the tool/spindle [N/m]

$k_{x,y}$.....stiffness of the tool/spindle in the x and y-directions [N/m]

$\boldsymbol{K}$ .....Kalman filter gain matrix or matrix of stiffness values in the x and y directions

K_n .....normal cutting pressure = 1.87×10^8 N/m^2

K_t .....tangential cutting pressure = 5.36×10^8 N/m^2

L .....length of workpiece = 986 mm

m.....mass of the tool/spindle = $m_{x,y}$ [kg]

m_{est}.....estimate of the mass of the tool/spindle [kg]

$m_{x,y}$.....mass of the tool/spindle in the x and y-directions [kg]

$\boldsymbol{M}$.....matrix of mass values in the x and y directions

N.....number of cutting teeth = 2 teeth

p.....tooth pass

p_r .....number of previous revolutions used in calculating rms_{rev}

$\boldsymbol{P}^-$ .....covariance matrix of the estimation error $\hat{x}^-$

$\boldsymbol{P}^+$ .....covariance matrix of estimation error $\hat{x}^+$

$\boldsymbol{Q}$ .....covariance matrix of the process noise

$\boldsymbol{R}$ .....covariance matrix of the measurement

Rot .....rotation of the tool [revolutions]

r.....radius of the tool = 6.35×10^{-3} m

r_s.....radius of the tool shaft 5.71×10^{-3} m

rms_{rev} .....average root-mean-square of X for each tool revolution[m]

r_1.....radius of the tooth #1 = 6.35×10^{-3} m (nominal)

r_2.....radius of the tooth #2 = 6.35×10^{-3} m (nominal)

R_v.....number of simulated tool revolutions

S_t.....number of simulated steps-per-revolution

t .....current time [s]

t_{est} .....time at which EKF estimates and TFEA diagrams are found [s]

T .....time step for Kalman filter algorithms = 1e-6 s

$\boldsymbol{u}$ .....force input vector = u_x [N]

u_x .....force input in the x-direction for Kalman filter algorithms [N]

U_p .....position of the p^{th} tooth tip w.r.t. the workpiece [m]

$\boldsymbol{U}_{old}$ .....vector of the previous tooth passes in the x-direcion [m]

$\boldsymbol{v}$ .....measurement noise vector $[v]= [v_x]$

v_x .....measurement noise = 0

V_p.....position of the p^{th} tooth tip w.r.t. the workpiece [m]

$\boldsymbol{V}_{old}$ .....vector of previous tooth passes in the y-direction [m]

$\boldsymbol{w}$.....process noise vector $[w] = [w_x]$ or $[w] = [w_x, w_K, w_C, w_K]$

w_C .....artificial noise term for $x_5 = 0$

w_K .....artificial noise term for $x_4 = 0$

w_M.....artificial noise term for $x_3 = 0$

w_x .....process noise = 0

$\boldsymbol{Q}$.....$\boldsymbol{A}^{-1}\boldsymbol{B}$

$\boldsymbol{x}$.....state array $[x_1, x_2]^T = [\, X\, , \dot{X}\,]^T$,

$[x_1, x_2, x_3, x_4, x_5]^T = [\, X\, , \dot{X}\, , m, k, c]^T$, or $[x_1, x_2]^T = [X, Y]^T$

X.....tool deflection in the x-direction [m]

$\boldsymbol{X}$.....vector of X values [m]

X_m .....once-per-revolution deflection of the tool in the x-direction [m]

X_{mean} .....X_{mean} value of a first-order polynomial evaluated at b_m

X_n.....once-per-tooth-pass deflection of the tool in the x-direction [m]

$\hat{x}^-$ .....priori (prior) estimate of X

$\hat{x}^+$ .....posteriori (subsequent) estimate of X

$\boldsymbol{v}$.....velocity array

y .....measurement scalar = [X]

Y.....tool deflection in the y-direction [m]

$\boldsymbol{Y}$.....vector of Y values [m]

Y_m .....once-per-revolution deflection of the tool in the y-direction [m]

Y_n.....once-per-tooth-pass deflection of the tool in the y-direction [m]

Ω.....spindle speed [rpm]

Ω_c .....current spindle speed [rpm]

Ω_{nom}.....nominal spindle speed [rpm]

ω_p .....instantaneous chip thickness for the p^{th} tooth

ω_1 .....chip thickness for tooth #1

ω_2 .....chip thickness for tooth #2

θ_{in} .....entry angle of the cutting tooth [rad]

θ_{out}.....exit angle of the cutting tooth [rad]

θ_p.....angle of the p^{th} cutting tooth [rad]

τ.....time step (time between consecutive tooth passes) [s]

γ.....nonlinear relation between ω_p and the cutting forces (F_{tp} and F_{np})

$\phi(\psi)$ .....trial function

ψ.....the "local" time on the j^{th} element for the TFEA analysis

ABSTRACT

In this work, two separate mathematical models, a traditional and new model, are presented for an end-milling process. The traditional model assumes circular tool motion, while the new model accounts for trochoidal tool motion resulting from the feed of the workpiece past the rotating tool. Simulated bifurcation diagrams are generated using each model and compared to experimental results. An extended Kalman filter (EKF) algorithm is created for estimating the states and model parameters of the milling process given the tool deflections in the x and y-directions and rotational angle. Once parameter estimates are calculated, stability analysis is performed to generate the stability bound of the system as a function of the spindle speed and depth of cut. A control system is designed for a simulated milling process that uses updated EKF parameter estimates to track the stability bounds of the system through time. Through knowledge of these stability bounds, the spindle speed and/or feed rate are varied to avoid instability (i.e. avoid the onset of chatter vibrations). This control system is unique in its ability to adapt to changing system dynamics. A chatter detection method is also given based on the root-mean-square (RMS) value of the once-per-tool deflection data. This method cannot avoid chatter vibrations form forming; however, it can detect and quantify the severity of chatter vibrations.

By comparing simulated and experimental results, the new milling model is found to more accurately predict the dynamics and stability of an actual milling operation. End milling contains a subcritical bifurcation resulting in hysteresis of the bifurcation point. Consequently, both chatter and chatter-free tool vibrations can exist for a single set of

milling conditions. Stability jumps within the hysteresis region are shown to be possible. The experimental tool deflection data collected shows signs of runout in the tool/spindle of the milling machine. Therefore, modifications to the new milling model are made to simulate runout in the analytical results (these results better match the tool dynamics from experimental tests). The EKF model parameter estimates of experimental and simulated deflection data are found to be accurate within 6.5% of their nominal values at a constant spindle speed and depth of cut. However, due to linear time-invariant assumptions in the milling model, the parameter estimates change as the spindle speed and depth of cut are varied. Therefore, parameter estimates must be updated in order to provide an accurate stability bound for the current state of the milling operation. Using updated stability information, the control system is able to keep the simulated milling processes chatter-free over large depth of cut ranges. Finally, tracking RMS values of the once-per-revolution tool deflection is shown effective in detecting the onset of chatter and gaging the chatter vibration magnitude.

Chapter 1 INTRODUCTION

In this chapter, an overview of previous milling research, a description of the milling system, and the motivation for and contributions obtained in this research are discussed. A literature review of previous milling, chatter detection/prevention, and parameter estimation research is given in Section 1.1. Background information on high-speed end milling and chatter vibrations, the motivation behind this research, and research objectives are presented in Sections 1.2, 1.3, and 1.4, respectively. In Section 1.5, the contributions that this research provides are discussed. Finally, Section 1.6 provides an overview of the work presented in this dissertation.

1.1 LITERATURE REVIEW

The following is a literature review of work performed in the areas of milling, chatter, stability analysis, and parameter estimation. The development of the mathematical milling models used in this research is first discussed in Section 1.1.1. Stability analysis techniques used in defining stable and unstable parameter rations in the milling process are given in Section 1.1.2. Methods used for detecting and avoiding chatter vibrations is also given here. Finally, Section 1.1.3 provides background literature for the development of various parameter estimation techniques.

1.1.1 THE MILLING MODEL

Early milling research is based on orthogonal cutting, where the direction of the cutting force, chip thickness, and tool dynamics do not change with time [1, 2]. From this research, frequency-domain models were developed for determining the exact

stability boundaries for turning and the approximate stability boundaries for milling [3]. Milling is a process that has multiple cutting teeth, a rotating tool, multiple degree-of-freedom (DOF) tool dynamics, and varying cutting forces and chip thicknesses [4]. Considering these milling characteristics further complicates the analysis of the milling operation. The 1-DOF orthogonal cutting analysis given by Tlusty [1] and Tobias [2] was expanded by Altintas [5-7] to a 2-DOF frequency domain algorithm for end-milling. This model accounts for tool motion in the *x* and *y*-directions (see Fig. 1) and uses a truncated Fourier series to approximate the entry and exit angles of the milling tool.

In this research, two separate 2-DOF mathematical models are used in simulating the milling process, a traditional and new model. Both models use equations given by Altintas [5-7] for calculating the forces exerted on the tool as it enters and exits the workpiece (these forces are a function of the instantaneous chip thickness, radial immersion, and cutting coefficients). The difference between the two models comes in the calculation of the chip thickness. The traditional model assumes circular tool motion of the tool with fixed entry and exit angles. The chip thickness equation used for this model is given by Mann [8-10] and Insperger [11]. The new chip thickness model allows for varying entry and exit angles (i.e. accounts for tool motion discontinuity) and accounts for the trochoidal motion of the tool caused by the feed of the workpiece past the tool. Radhakrishan [12-15] developed the new chip thickness model at the University of Missouri.

1.1.2 CHATTER DETECTION AND PREVENTION

The explanation for machine–tool chatter was first given by Tlusty [1], Tobias [2], and Merritt [16] as "regeneration of waviness" in the cut surface. Their research

provided the groundwork for the development of stability lobe diagrams. In the work of Weck [17] and Gather [18], frequency domain methods are used in computing stability lobe diagrams that indicate stable and unstable regions as a function of the control parameters (i.e., spindle speed and depth of cut). An important result from these analyses was the ability to identify stable cutting regions in which larger metal removal rates can be obtained by cutting at higher spindle speeds. Using the 2-DOF frequency domain model given by Altintas [7] provides accurate stability predictions except for cuts with very low radial immersion [3]. Low radial immersion milling was investigated by Davies [19] where a 1-DOF model was formed using a discrete "map" in order to predict the existence of stability regions and to characterize the transitions from stable to unstable regions. The discrete model given by Davies [19] was later expanded by Bayly [20] to use time finite element analysis (TFEA) in generating stability lobe diagrams. The 1-DOF TFEA method presented by Balyl [20] was expanded to a 2-DOF method [3, 4, 21]. This 2-DOF TFEA method is used in this research for tracking the stability of milling processes at various spindle speeds and depths of cut. A full description of the TFEA stability bound method is given in Section 9.1.

To generate stability bounds using the methods given above, knowledge of system parameters (specifically the mass, and damping, and stiffness of the tool/spindle) are required. Experimental tests can be performed to estimate these parameters. However, if something in the system changes such as tool replacement or tool wear, new parameters must be experimentally found and a new stability bound generated. This has lead to the development of on-line chatter detection techniques that are not dependent on knowledge of system dynamics. In the frequency domain, several studies have focused on chatter

detection through the measurement of dynamic force [22], sound [23, 24], acceleration [25] and displacement [26]. In these methods, the system must be on the verge of (or experience) chatter for any kind of action to be taken by the machine or operator to prevent the likelihood of chatter in the future.

One such frequency domain method is given by Smith [24], where a microphone is used to gather the sound waves produced by the machining operation. Once chatter is detected, adjustments to the spindle speed and feed rate are made to achieve a stable milling process. The spindle speed is iteratively adjusted so that the frequency with which the teeth pass is equal to the dominant frequency in the spectrum of the microphone output. If the frequency of the sound wave exceeds a predetermined threshold, which represents the existence of chatter, the control system stops the feed, calculates a new spindle speed, adjusts the speed, and then incrementally increasing the feed once again [24]. Since a microphone is used in determining when chatter has occurred, no knowledge of the system dynamics is required. In later work by Delio [23], it was found that a microphone based system is capable of detecting chatter arising from tool, workpiece, and machine flexibilities (a sufficient chatter signal is also attainable at low-immersion cuts).

The main drawback of the method given by Smith [24] is that chatter must occur (although for a very short period of time) for the control system to adjust the spindle speed an feed rate so that chatter vibrations are eliminated. Specifically, the control system given by Smith [24] was able to detect chatter in approximately 250-500 milliseconds after it formed [23]. To entirely eliminate chatter, knowledge of system parameters is needed to generate a TFEA stability diagram [3, 4, 21] (or a stability

diagram created from another method) so that appropriate spindle speeds and depths of cut can be selected.

1.1.3 PARAMETER ESTIMATION

Various approaches to parameter estimation are discussed in previous literature. These including energy methods [27], frequency domain methods [28], and set inversion via interval analysis (SIVIA) with Taylor expansions [29]. Another parameter estimations technique is the Bayesian approach, where probability density functions are representative of uncertainty in the model. The Bayesian approach consists of estimating a posteriori probabilities of the parameters and therefore transforming a parameter estimation problem into the problem of finding maximum likelihood values of the parameters [30]. One form of Bayesian estimation is the Kalman filter [31, 32]. The Kalman filter is used in detecting signals of known form (pulses and/or sinusoids) in the presence of random noise [31]. The Kalman filter is optimal for linear systems with Gaussian noise [30]. State estimates are calculated by propagating the mean of the states and state errors through time [33]. A mathematical model of the system and a measurement of the desired state, which contains noise, are used in finding an estimate that better represents the true value of the state. The predicted value of the state, which is found from the mathematical model, and the measurement of the state are weighted depending on uncertainty [33].

The extended Kalman filter (EKF) is an expansion of the basic Kalman filter [31, 32] that is able to estimate both states and system parameters. The EKF is "extended" in that it applies to nonlinear systems. Desired parameters are added to the system as pseudo states and estimated along with the actual states [33]. Adding pseudo states

causes the system to become nonlinear. The EKF has been used for parameter estimation in applications for turbine engine control and performance monitoring [34, 35], continuous time heat exchanger models [36], car engine performance [37], and multi-body robot systems [38], among many others. In the work of Sujan [38], an EKF is used in estimating dynamic parameters of a field robot, which is equipped with a manipulator arm and onboard sensors including inclinometers, accelerometers, vision systems, and force/torque sensors. Proposed control algorithms for such a system rely on accurate physical models of the system and its tasks [38]. To successfully apply such algorithms, accurate estimates of the dynamic parameters of the system are required. Parameter estimates can be found off-line through experimental tests. However, certain conditions cause given parameters to change. For example, temperature fluctuations result in changes in the stiffness and damping of the suspension system with time, and vehicle fuel consumption cause changes in the location of the center of gravity, the mass, and the inertia of the system [38]. Therefore, on-line identification of these parameters is performed using an EKF algorithm so that the predicted dynamic response of the robot system matches that of the real system.

Sujan [38] successfully showed the ability and importance of on-line EKF parameter estimation in a multi-body robot system. On-line parameter estimation is important in the milling process for many of the same reasons outlined by Sujan [38]. Milling parameters (specifically the mass, damping, and stiffness of the tool/spindle) can be found off-line through experimental procedures. However, these tests must be repeated if changes in the system occur due to tool wear, tool chipping, and/or a tool change. Furthermore, it is shown that EKF estimates from experimental tool deflection

data change as the depth of cut, b, and/or the spindle speed, Ω, are varied. These changes in parameters are due to the inability of the linear milling model to accurately represent the nonlinear system over a range of b or Ω (i.e. the parameter values change in order for the linear model to adapt to the nonlinear system). Un-modeled dynamics of the system, whether they are linear or nonlinear, will also cause changes in parameter values at various milling conditions. By updating EKF parameter estimates on-line, parameter values can be generated that best describe the current state of the actual system in terms of the linear model.

1.2 BACKGROUND IN HIGH-SPEED MILLING AND CHATTER

High-speed milling (HSM) has become exceedingly popular since its inception in the 1980s. At that time, spindles were developed that could rotate at much higher speeds while retaining good stiffness, which is essential for maintaining the dimensional accuracy of the machined part [39]. Given its ability for high removal rates and low location error, HSM is one of the most cost effective machining operations available [40]. HSM is especially important in machining aluminum. Given its material properties, aluminum can be machined relatively easily and, therefore, lends itself to large material removal rates and high spindle speeds [39]. HSM has become one of the foremost aluminum machining processes used in a wide variety of industrial applications [24]. For example, improvements by machine tool builders led a shift within the aerospace community from labor-intensive sheet metal assemblies to monolithic aluminum components. However, the opportunity to capture substantial cost savings typically requires accurate predictive analysis tools to avoid unstable oscillations, meet

dimensional requirements, and to take full advantage of a machining center's capabilities [10].

The diagrams in Fig. 1 show the conditions for up and down-milling operations. The areas given in red represent the workpiece material removed by the current tooth pass. For up milling, the chip thickness increases as the tool passes through the workpiece (the opposite is true for down-milling). As shown in Fig. 1, milling is an interrupted process in that the cutting teeth of the tool enter and exit the workpiece as the tool rotates. The primary limiting factor in material removal rates is the relative oscillations between a cutting tool and workpiece caused by the tool coming in and out of contact with the workpiece [6, 39]. More specifically, the current tooth cuts a surface on the workpiece produced by the previous tooth pass. Therefore, the chip thickness of the current tooth cut not only depends on the current position of the tool, but also depends on the location of the previous tooth. As a result, there exists a regenerative effect in milling that must be accounted for in stability analysis [41]. This regenerative effect has become the commonly accepted explanation of machine tool chatter [42-44].

In most instances, HSM is applied to machining operations where there is an "inherent lack of stiffness" in the system, mainly on the part of the tool (i.e. in most cases the workpiece can be considered rigid) [39]. This lack of stiffness leads to tool vibrations caused by the forces exerted on the tool as it comes in and out of contact with the workpiece. These tool vibrations can either be stable (chatter-free vibrations) or unstable (chatter vibrations) depending on milling parameters such as spindle speed, radial immersion, depth of cut, feed rate, workpiece material, and tool geometry. However, the depth of cut, b, which directly corresponds to the chip width, is the primary factor in

stability [39]. When chatter develops, the unstable tool vibrations cause large dynamic loads on the machine spindle and table structure, damage to the cutting tool, and a poor surface finish [6, 8, 39, 45]. Reducing the material removal rate can reduce or eliminate chatter; however, this leads to reduced productivity [4]. In fact, chatter vibrations limit the depth of cut and radial immersion of a given milling process; therefore, increasing the spindle speed is the only way of achieving higher material removal rates [39].

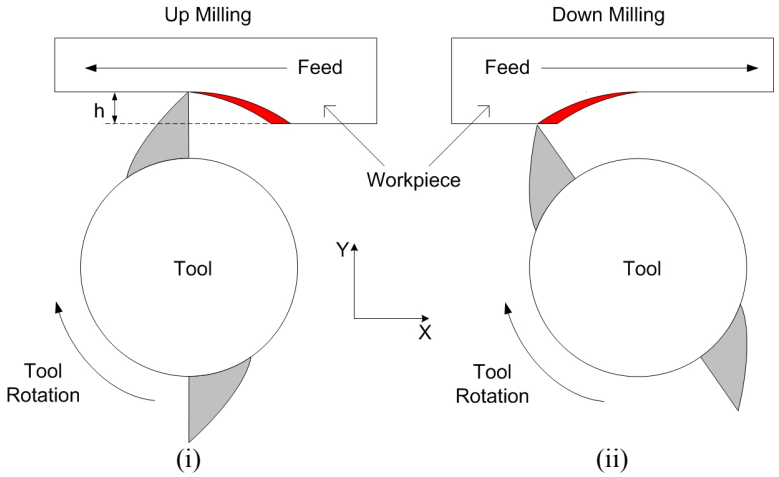

Fig. 1. Diagram of an up milling (i) and down milling (ii) process (shown from top looking down). The depth of cut, *b*, is into the paper.

The bifurcation diagram for a milling process as a function of the depth of cut, b, is given in Fig. 2. This diagram relates stable and unstable equilibrium points of the system for an increasing and deceasing depth of cut. The solid blue lines in Fig. 2 represent once-per-time-delay (i.e. once-per-tooth-pass) tool deflection data in the x-direction, X_n. The red dashed lines represent unstable solutions. Only stable solutions (i.e. solid blue lines) can be obtained experimentally. Suppose all milling parameters are held constant except for the depth of cut, b. Then, suppose the system is initially chatter-free and b is increased until the tool vibrations transition from chatter-free to chatter vibrations. The depth of cut at this transition is the bifurcation point for an increasing b.

The stability path the system follows for an increasing b is shown with arrows in Fig. 2. Furthermore, suppose the system initially contains chatter and b is decreased until the tool vibrations transition from chatter to chatter-free vibrations. The depth of cut at this transition is the bifurcation point for a decreasing b. The stability path the system follows for a decreasing b is also shown with arrows in Fig. 2. Due to hysteresis, the bifurcation point for a decreasing b occurs at a smaller depth of cut than for an increasing b (this can be seen by comparing the stability paths for an increasing and decreasing b in Fig. 2). Ignoring the outlying stable solutions (i.e. solid blue lines on the right of Fig. 2) and focusing on the region near the bifurcation point at b^*, the bifurcation point is shown to be subcritical in that one stable and two unstable solutions exist when $b < b^*$, and a single unstable solution exists when $b > b^*$) [46].

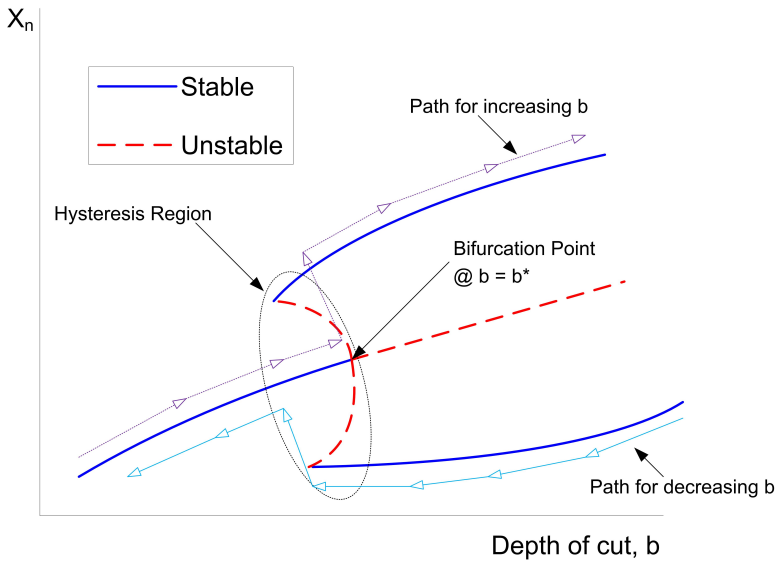

Fig. 2. Subcritical bifurcation diagram for a milling process as a function of the tool displacement at each time-delay (i.e. at each tooth pass), X_n, and depth of cut, b. Red lines represent stable equilibrium points, which can be experimentally observed. The blue dashed lines represent unstable equilibrium points, which cannot be observed experimentally [15].

At a given depth of cut, the points on the blue line in Fig. 2 represent stable equilibrium of the system. For small values of b there is one stable equilibrium point (i.e. chatter-free vibrations exist). When b is large, however, there are multiple stable equilibrium points (i.e. chatter vibrations exist). Referring to Fig. 2, there is a region of b values where both stable chatter-free and chatter equilibrium points exist. This is a result of hysteresis in the milling system. In previous milling literature, hysteresis in the bifurcation point has not been shown though simulations or experimentally. However, the existence of hysteresis is shown in this work. If hysteresis were not present, there would not be unstable solutions (see red dashed lines in Fig. 2) connecting the bifurcation point and stable outlying solutions. Furthermore, the two stable solutions for $b > b^*$ would intersect the bifurcation point at $b = b^*$. Therefore, the bifurcation point would be classified as supercritical [46]. Given that hysteresis does exist, however, the conditions of the system (mainly if b is increased of decreased) will determine which set of stable equilibrium points the solution will tend towards when b is within the hysteresis region. Furthermore, a small disturbance to the system may cause the system to jump from a chatter-free solution to a chatter solution within the hysteresis region. Once the solution jumps to the chatter equilibrium, it can remain at the chatter equilibrium or return to the chatter-free equilibrium.

1.3 MOTIVATION

Chatter in the milling process results in poor surface finish of the machined part, poor dimensional accuracy, large spindle loads, and can lead to excessive tool wear or tool breakage [6, 8, 39, 45]. In a manufacturing environment, these effects of chatter result in revenue loses due to scrapped parts, re-machining of parts, tool replacement,

machine damage, and machine downtime. Avoiding chatter (i.e. avoiding cutting conditions that results in chatter vibrations) can significantly reduce machining costs. The goal of this research is to better understand bifurcations in the milling process and then develop a control method capable of predicting the onset of chatter (i.e. predicting the stability bound of the system). Once the stability bound is know, necessary changes to milling parameters (specifically the spindle speed and feed rate) can be made to avoid chatter entirely. Once tested and proven, this control method (or variations on it) can potentially be marketed as a way to greatly reduce or eliminate the ill effects of chatter listed above.

1.4 OBJECTIVES

The objectives of this research are as follows.

- Create data acquisition (DAC) system used in collecting experimental tool deflection data for an up-milling process.
- Verify the accuracy of the mathematical models by comparing simulated and experimental data.
- Improve the models based on experimental results.
- Experimentally and analytically verify that end milling contains a subcritical bifurcation (i.e. contains hysteresis).
- Create an extended Kalman filter algorithm capable of estimating the model parameters of the milling system (i.e. the mass, damping, and stiffness of the tool/spindle) from tool deflection data and tool rotational angle.

- Estimate model parameters from experimental and analytical deflection data to verify the accuracy of the estimates.
- Test whether changes in the spindle speed and/or depth of cut affect parameter estimates of experimental data.
- Determine the effect of milling and model parameter on the stability of the system.
- Create control algorithm that is capable of predicting and avoiding chatter in a simulated milling process by varying the spindle speed and feed rate.
- Test control system on various simulated milling processes and verify its ability to avoid the onset of chatter.
- Create DAC system to experimentally estimate the model parameters on-line.
- Obtain on-line root-mean-square (RMS) values for experimental deflection data.
- Design sensor housing that will protect the sensors from the machining environment (i.e. protect the sensors from metal chips and coolant used in commercial machining operations).

1.5 CONTRIBUTIONS

A list of the contributions that this work provides is given in Table 1. Entirely new contributions and improvements on existing work in the fields of milling, parameter estimation, and chatter prevention are given in this table.

Table 1. Contributions provided by this work. Entirely new contributions and improvements on existing work are indicated for each item.

Subject	Description	New	Improve-ment
Bifurcations in Milling	Bifurcation points are shown to contain hysteresis through both simulations and experimental test data.	X	
	Disturbance inputs to the system can cause equilibrium jumps (i.e. a jump from chatter-free to chatter tool vibrations) within the hysteresis region. This is shown through simulations and experimentally.	X	
New Milling Model	New milling model algorithm given by Radhakrishan [12-15] is optimized for faster simulation time.		X
	Tool/spindle runout is added to the model to produce simulated results more representative of the experimental results.		X
Runout in Milling	Through simulated results, runout is shown to increase the period of tool motion from 1/2 to 1 full revolution. This increase in period is a result of unequal forces applied to tooth #1 and #2 as they are in contact with the workpiece.	X	
	The amount of runout is related to specific changes in the tool dynamics.	X	
Extended Kalman Filter (EKF)	EKF algorithm is created capable of estimating the states (i.e. the deflection and velocity of the tool tip) and the model parameters of the tool/spindle (i.e. the mass, damping, and stiffness) given the rotational angle of the tool and the deflection of the tool in the x and y-directions.	X	
	EKF is tested on simulated and experimental data to verify the accuracy of its estimates.	X	
	Parameter estimates are found to vary depending on spindle speed and depth of cut.	X	
	Data acquisition system is used to calculate EKF estimates during a milling operation (i.e. on-line).	X	
Control System	EKF estimates are continually updated to provide estimates of the current state of the milling operation.	X	
	EKF estimates are used in generating TFEA stability bounds of the system.		X
	Spindle speed and/or feed rate are adjusted based on stability bounds to avoid the onset of chatter vibrations.	X	
	Control system is shown to keep a simulated milling process chatter-free for a variety of milling parameters.	X	
Root-mean-square (RMS)	A chatter detection method based on the RMS values of the once-per-revolution deflection data is created.	X	
	Capable of indicating the onset and magnitude of chatter vibrations.	X	
	Data acquisition system is used to calculate RMS values on-line.	X	
Parameter Influence on Stability	The effect of perturbations in the model parameters (m, c, and k) and spindle on the TFEA stability bound of the system are found.	X	

1.6 OVERVIEW

The following paper is organized as follows. The 2-DOF mathematical milling model (see Altintas [5-7]) used in calculating the forces exerted on the tool as it enters and exits the workpiece is given in Chapter 2 (this force model is dependent on the instantaneous chip thickness). Two separate chip thickness models are discussed in Chapter 3. The first chip thickness model (denoted as the traditional model) assumes a circular tool path and uses equations given by Mann [8-10] and Insperger [11]. This model only uses one time-delay in calculating the chip thickness (i.e. it takes into account the workpiece surface created by the previous tooth pass). The second model (referred to as the new model) calculates the chip thickness through the knowledge of multiple time-delays (i.e. it takes into account the workpiece surface created by multiple tooth passes). First introduced by Radhakrishnan [12-15], the new model takes into account the trochoidal motion of the tool, which is more representative of the actual milling operation. Both the traditional and new chip thickness models are used in combination with the milling model given in Chapter 2 to simulate various milling processes. The experimental system used in measuring the tool deflection and period is given in Chapter 4. Experimental procedures used in obtaining model parameter estimates (i.e. the mass, damping, and stiffness) of the milling tool/spindle are also given here. Simulated and experimental results are given in Chapter 5 to show the existence of hysteresis in the milling bifurcation diagram. Additional tests are conducted to illustrate the possibility of equilibrium jumps within the hysteresis region.

The effect of tool/spindle runout on the tool deflection, instantaneous chip thickness, and cutting forces are discussed in Chapter 6. Simulated results with and

without runout are compared with experimental data. Discrete Kalman filter and discrete extended Kalman filter algorithms are constructed in Chapter 7 to estimate the desired states of the system (i.e. the deflection and velocity of the tool in the x-direction) and model parameters (i.e. m, c, and k). Estimates for both simulated and experimental deflection data are given. Additional experimental results are given in Chapter 8 for a variety of spindle speeds and testing procedures. Bifurcation diagrams and model parameter estimates from each experimental result are given. A control system is given in Chapter 9 that uses updated EKF model estimates to generate stability lobe diagrams, which indicate stable and unstable regions in the space defined by depth of cut and spindle speed. These stability diagrams are then used to adjust the spindle speed and/or feed rate of a simulated milling process to avoid the onset of chatter. The root-mean-square (RMS) value of the tool deflection data is also given in Chapter 9 (RMS is used in quantifying the onset and severity of chatter vibrations). The influence of the model parameters and spindle speed on the stability of a given milling process is discussed in Chapter 10. This analysis ranks the parameters by their ability to change the stability bound of a given milling system (i.e. change the point at which the system bifurcates). Finally, Chapter 11 summarizes all notable results and findings. Suggestions for continuing and expanding this research are also given here.

Chapter 2 MATHEMATICAL MILLING MODEL

Low radial immersion end-milling is an interrupted process in which the motion of the tool effects the chip load and cutting forces, leading to chatter vibrations in certain conditions [3]. As shown in Fig. 3, there are two degrees-of-freedom (DOF) accounted for in the *x* and *y*-directions. The workpiece is assumed to be rigid, and the tool is assumed to be flexible [3]. The forces on the tool (see Fig. 3) are only applied when the tool is cutting (i.e. when one of the cutting teeth are engaged in the workpiece). The forces are zero when the tool is not cutting. In this chapter, the 2-DOF milling model is derived. The forces for an orthogonal turning process are first analyzed in Section 2.1 for simplicity. These force calculations are then modified in Section 2.2 for a milling process and combined with the 2-DOF milling model.

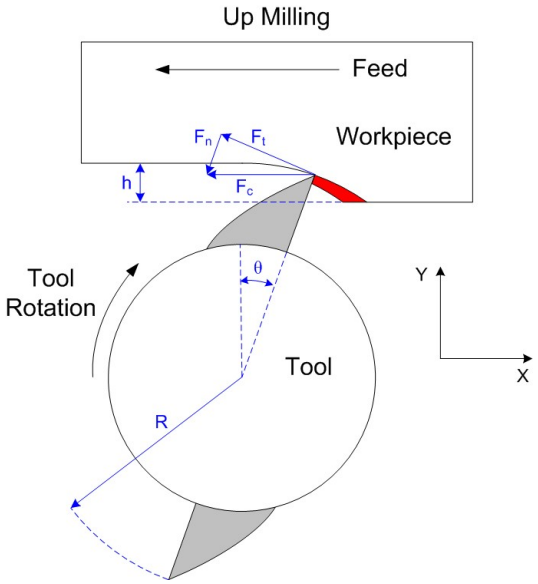

Fig. 3. Diagram of the cutting forces during an up-milling process. The red area of the workpiece represents the material removed by the current tooth pass.

2.1 CUTTING FORCES IN MILLING

Milling is an interrupted process where the cutting forces turn on and off as the tool enters and exits the workpiece. Therefore, the mathematical model must account for the fact that the tool has a finite entry and exit angle. As shown in Fig. 3, a tangential force, F_t, and normal force, F_n, are applied to the milling tool as it passed through the workpiece. The cutting forces are proportional to the uncut chip area shown in red in Fig. 3 [7, 39, 47]. The resultant cutting force, F_c, is the sum of the normal and tangential forces. While in contact with the workpiece, the force model for the milling operation can be approximated as a model of forces identical to that of a turning operation with orthogonal cutting. This assumes that the helix angle of the cutting tooth is zero. A schematic of the force distribution for an orthogonal turning operation is given in Fig. 4. For a turning operation, the forces in the tangential and normal directions are given by Altintas [6] as

$$F_t = K_t b h, \tag{1}$$

$$F_n = K_n b h, \tag{2}$$

where b is the depth of cut, h is the radial immersion, and K_t and K_n are the respective cutting coefficients in the tangential and normal directions. A full derivation of the cutting coefficients is given by Radhakrishnan [15]. Estimated values of K_t and K_n for aluminum 7050-T7451 (i.e. the same workpiece material used in this research) are experimentally found by Mann [48] to be 5.36×10^8 and 1.87×10^8 N/m^2, respectively. These cutting coefficient values are used for all analytical calculations in the following chapters.

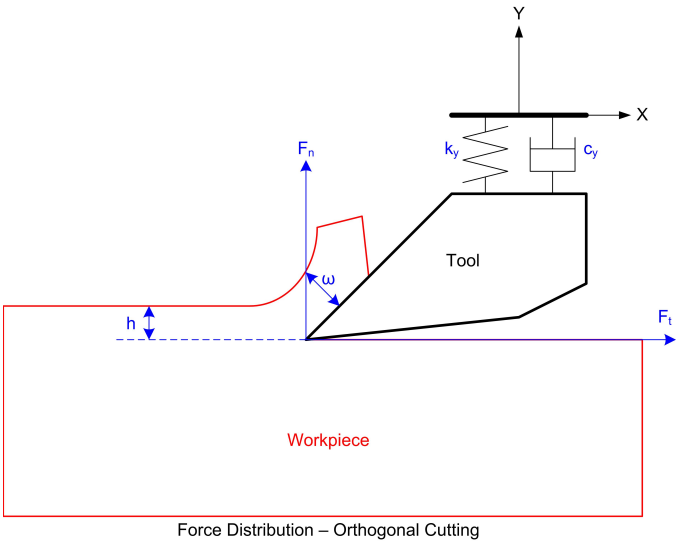

Fig. 4. Schematic of the force distribution for a turning operation with orthogonal cutting. The depth of cut, *b*, which is not shown, is into the paper [6].

2.2 MODEL AND FORCES

For the turning operation given in Fig. 4, the tool is in continuous contact with the workpiece. Therefore, the radial immersion, h, remains constant and is equivalent to the chip thickness of the material being removed, ω. During a milling operation, however, the tool enters and exits the workpiece introducing a time-delay into the system and causing ω to vary along the length of each cut. The schematic given in Fig. 5 shows the directional cutting forces for both up and down-milling. The red regions represent the workpiece material removed by the current tooth pass. The tool is assumed to behave as a 2-DOF system consisting of two second-order systems with a given mass, damping, and stiffness. The stiffness, $k_{x,y}$, and damping, $c_{x,y}$, in the respective directions of the system are given in Fig. 5. The mass of the tool, $m_{x,y}$, is not represented in this figure. Variables $m_{x,y}$, $c_{x,y}$, and $k_{x,y}$ represent the model parameters of the milling system in the x and y-directions.

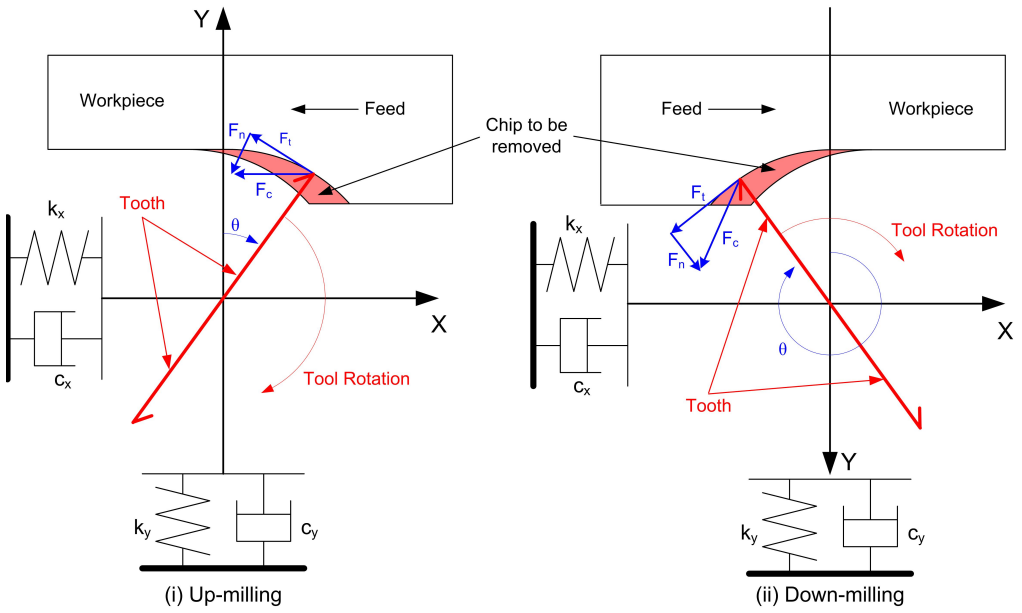

Fig. 5. Schematic of the directional cutting forces and model parameters in the flexible directions of the tool: (i) up-milling (ii) down-milling. The cutting teeth of the tool are given as red lines. The red area of the workpiece represents the material removed by the current tooth pass.

As stated above, end milling is an interrupted process. Therefore, the normal and tangential force equations for a turning process (see Eqs. (1) and (2)) must be modified to allow the forces to be turned on when the tool is in contact with the workpiece and turned off when it is not. For milling, the forces on the p^{th} tooth in the tangential, F_{tp}, and normal, F_{np}, directions are expressed by Mann [10] as

$$F_{tp} = K_t b \omega_p(t)^{\gamma} g_p(t), \tag{3}$$

$$F_{np} = K_n b \omega_p(t)^{\gamma} g_p(t), \tag{4}$$

where ω_p is the instantaneous chip thickness for the p^{th} tooth, $\gamma \neq 1$ causes a nonlinear relationship between the chip thickness and the cutting forces, and the function $g_p(t)$, which is used to turn the forces on and off, is given as

$$g_p(t) = \begin{cases} 1, \text{ if the } p^{th} \text{ tooth is active} \\ 0, \text{ if the } p^{th} \text{ tooth is not active} \end{cases}. \quad (5)$$

For this research, the relation between the chip thickness and the cutting force is considered linear (i.e. $\gamma = 1$).

To obtain a useful model of the milling operation, the forces in the normal and tangential directions must be transformed from a rotating reference frame to a fixed reference frame (i.e. the forces are transformed from F_n and F_t to F_x and F_y).

$$\begin{bmatrix} F_x \\ F_y \end{bmatrix} = \begin{bmatrix} -\cos\theta & -\sin\theta \\ \sin\theta & -\cos\theta \end{bmatrix} \begin{bmatrix} F_t(X,Y,\omega) \\ F_n(X,Y,\omega) \end{bmatrix} \quad (6)$$

The fixed frame linear model of the milling system is given as

$$m_x\ddot{X} + c_x\dot{X} + k_xX = F_x, \quad (7)$$

$$m_y\ddot{Y} + c_y\dot{Y} + k_yY = F_y, \quad (8)$$

where $\ddot{X}$, $\dot{X}$, and X are the acceleration, velocity, and position of the tool tip in the *x*-direction, and $\ddot{Y}$, $\dot{Y}$, and Y are the acceleration, velocity, and position in the *y*-direction, respectively [3, 10]. This linear model can also be represented in the following matrix form.

$$\begin{bmatrix} m_x & 0 \\ 0 & m_y \end{bmatrix} \begin{bmatrix} \ddot{X}(t) \\ \ddot{Y}(t) \end{bmatrix} + \begin{bmatrix} c_x & 0 \\ 0 & c_y \end{bmatrix} \begin{bmatrix} \dot{X}(t) \\ \dot{Y}(t) \end{bmatrix} + \begin{bmatrix} k_x & 0 \\ 0 & k_y \end{bmatrix} \begin{bmatrix} X(t) \\ Y(t) \end{bmatrix} = \begin{bmatrix} F_x \\ F_y \end{bmatrix} \quad (9)$$

Chapter 3 CHIP THICKNESS CALCULATION

In this chapter, two separate models for calculating the instantaneous chip thickness, ω, are given. The first model, referred to as the traditional model, is derived in Section 3.1. The traditional model assumes circular motion of the tool; therefore, the entry and exit angles of the tool and workpiece are fixed [8-11]. The process used in simulating a milling process with the traditional chip thickness model is given in Section 3.2. The second model, referred to as the new model, is derived in Section 3.3. The new model accounts for tool motion discontinuity, allowing for varying entry and exit angles during the cutting process [12-15]. Furthermore, the new model takes into account the trochoidal motion of the tool (i.e. the actual motion of the tool due to the feed of the workpiece past the rotating tool). The simulation process utilizing the new chip thickness model is presented in Section 3.4.

3.1 TRADITIONAL CHIP THICKNESS MODEL

When assuming a circular tool path, the entry angle, θ_{in}, and exit angle, θ_{out}, for a given cutting tooth are a function of the radial immersion, h, and tool radius, r (i.e. θ_{in} and θ_{out} are constants).

$$\left.\begin{aligned}\theta_{in} &= 0 \\ \theta_{out} &= \cos^{-1}(1-h/r)\end{aligned}\right\}\text{up-milling} \tag{10}$$

$$\left.\begin{aligned}\theta_{in} &= \pi - \cos^{-1}(1-h/r) \\ \theta_{out} &= \pi\end{aligned}\right\}\text{down-milling} \tag{11}$$

From Eq. (10), the entry angle for tooth #1 and #2 of a two-flute tool can never be less than 0 and 180 degrees, respectively, for an up-milling process. The radial chip thickness at time t can be calculated by projecting the current position of the tool, $X(t)$ and $Y(t)$, with the position of the tool on the previous tooth pass, $X(t-\tau)$ and $Y(t-\tau)$. The variable τ is the time-delay in the system (i.e. the time between consecutive tooth passes) given as $\tau = 60/(N\Omega)$, where N is the number of teeth-per-tool and Ω is the spindle speed in revolutions per minute [15]. Referring to the red region of the workpiece in Fig. 5, the radial chip thickness is the thickness of the red region along the line projected from the center of the tool to the tip of the cutting tooth. The instantaneous radial chip thickness for the p^{th} tooth is approximated by Mann [10] as

$$\omega_p(t) \approx h\sin\theta_p(t) + [X(t) - X(t-\tau)]\sin\theta_p(t) + [Y(t) - Y(t-\tau)]\cos\theta_p(t), \qquad (12)$$

where f is the feed-per-tooth and θ_p is the cutter rotation angle for the p^{th} tooth. Combining Eq. (12) with Eqs. (3) - (9) results in the complete traditional milling model.

3.2 MILLING SIMULATION WITH TRADITIONAL MODEL

A block diagram of the milling simulation using the traditional milling model is given in Fig. 6. The simulation begins by defining process parameters (i.e. depth of cut, b, feed rate, f, radial immersion, h, spindle speed, Ω, cutting coefficients, K_t and K_n, number of cutting teeth, N, tool radius, r, etc.) and the model parameters (i.e. m, k, and c in the x and y-directions). The numerical parameters (i.e. the number of revolutions, R_v, and steps per revolution, S_t) are also defined [15]. The program then initiates the tool revolution loop. At a given simulated time step, dt, if the current angular position of p^{th} tooth, θ_p, is contained within the entry and exit angles given in Eqs. (10) and (11), then

Eq. (12) is used to evaluate the current chip thickness of the p^{th} tooth, ω_p. If θ_p is outside the entry and exit angles, ω_p is set equal to zero (i.e. the forces are set to zero). If ω_p is

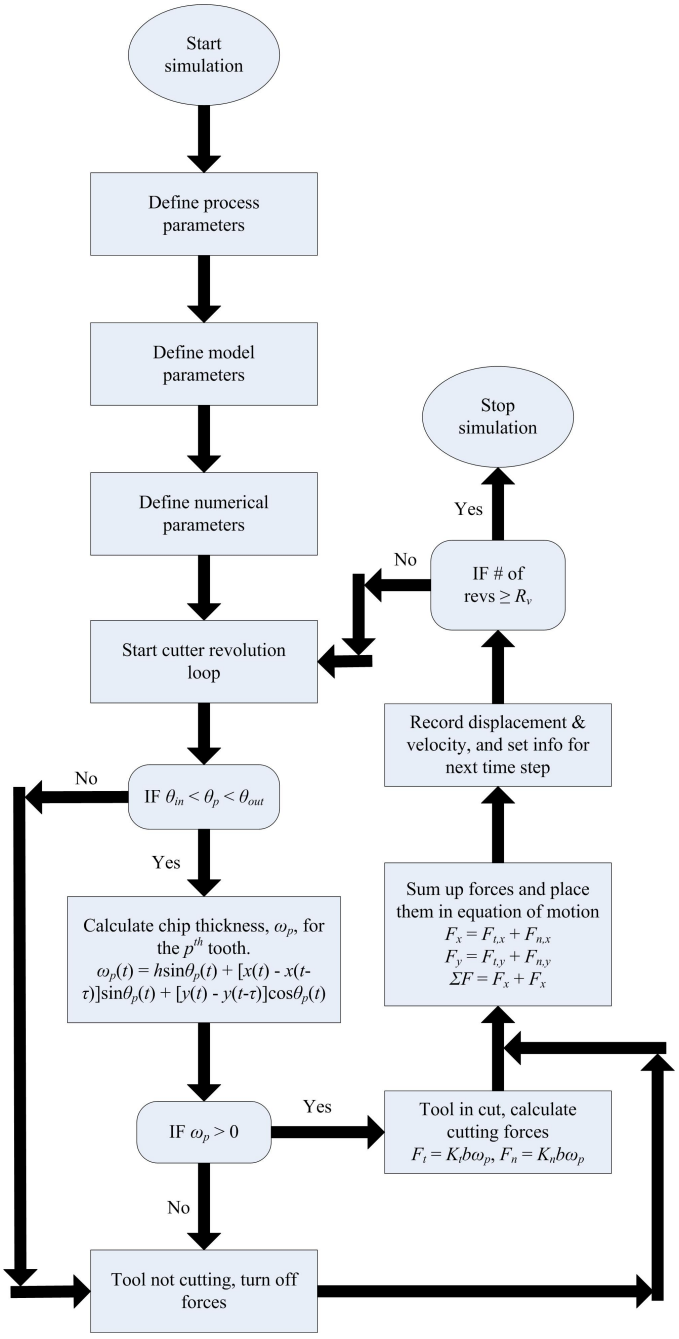

Fig. 6. Flowchart of the milling simulation using the old chip thickness calculation model [15].

greater than zero, the forces in the flexible directions of the tool, F_x and F_y, are then calculated using Eqs. (3) - (6); otherwise, the forces are set to zero. Equation (9), along

with the states from the previous simulated time step, t - dt, are then used in calculating the states of the system for the current time, t. The current states are then saved and used in the calculation of the states for the next time step, $t + dt$. The main loop continuous until the simulated revolutions equals the predefined number of revolutions.

3.3 NEW CHIP THICKNESS MODEL

The traditional chip thickness model (see Eq. (6)) only has the ability to look back one time step, τ (i.e. one tooth pass). The new model, on the other hand, is capable of looking back several time steps, providing information from multiple tooth passes. This is especially important in capturing the dynamics of the milling process during chatter vibrations where multiple tooth passes can affect the workpiece surface the current tooth is cutting. The new model also takes into account the trochoidal motion of the tool due to the feed of the workpiece past the rotating tool. The coordinates of the p^{th} tooth at time t are calculated from

$$U_p(t) = r\sin\theta_p(t) + dfdt + X(t), \tag{13}$$

$$V_p(t) = r\cos\theta_p(t) + Y(t), \tag{14}$$

where U_p and V_p are the positions of the p^{th} tooth tip with respect to the workpiece in the x and y-directions, respectively, df is the incremental feed rate, and dt is the simulated time step [15]. The trochoidal tool motion, which occurs in the x-direction, is accounted for through the expression $dfdt$ in Eq. (13).

To calculate the radial chip thickness at each time step, the position of the current tooth (U_p, V_p) is compared with the location of previous tooth passes ($\boldsymbol{U}_{old}$, $\boldsymbol{V}_{old}$). Vectors $\boldsymbol{U}_{old}$, and $\boldsymbol{V}_{old}$ contain tooth position data from previous revolutions. A simulated tooth

path for one complete rotation of a two-flute tool is shown in Fig. 7 (this tooth path is from a stable up-milling process at a constant depth of cut, b). Referring to Fig. 7, the chip thickness for the p^{th} tooth is calculated as the shortest distance from the current position of the tooth (U_p, V_p) (see red dots) to the previous cut surface ($\boldsymbol{U}_{old}$, $\boldsymbol{V}_{old}$) (see blue line) along a radial line connecting (U_p, V_p) to the center of the tool (see black dashed lines). The black dots in Fig. 7 represent the intersection point of the previous cut surface and the radial line projecting from (U_p, V_p) to the center of the tool. For a given time step, if no intersection is found or the chip thickness is found to be negative (as shown to be the case for the data points on the far left of Fig. 7), then the p^{th} tooth is not engaged with the workpiece. Otherwise, the p^{th} tooth is cutting.

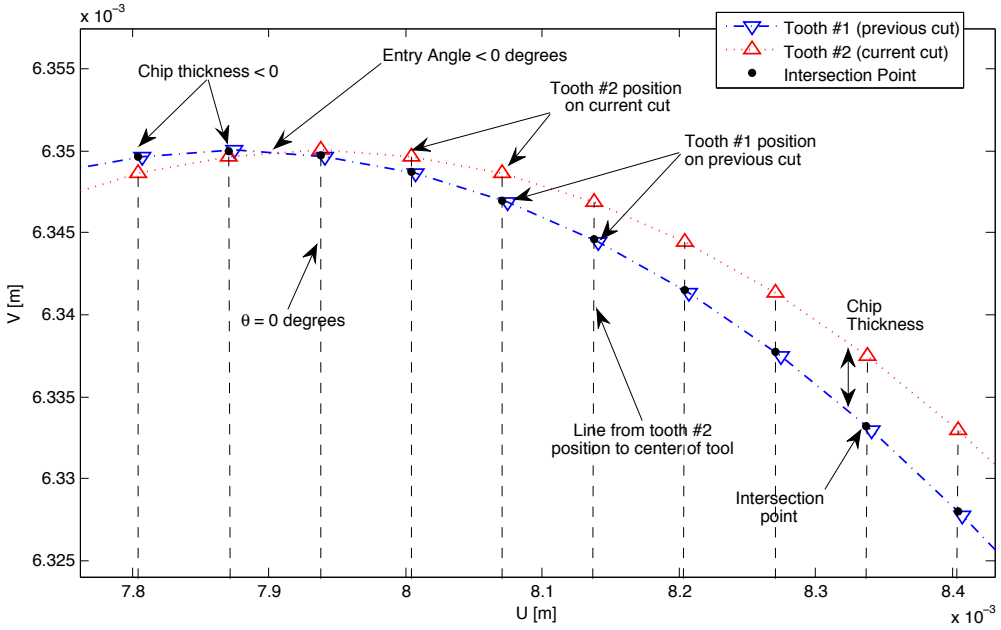

Fig. 7. Simulation of the tooth pass of a two flute milling tool for one revolution.

The traditional chip thickness model discussed in Section 3.1 assumes a circular tool path with fixed entry and exit angles given by Eqs. (10) and (11) (i.e. the chip thickness for a given tooth is only calculated within a defined range of rotational angles,

θ). The new chip thickness model, however, calculates the chip thickness at all values of θ. From Fig. 7, the entry angle for a simulated up-milling process at a constant depth of cut, b, is in fact less than 0 degrees (this is a result of the trochoidal motion of the tool). Therefore, the new chip thickness model is expected to provide a more accurate representation of the dynamics that occur in an actual milling operation.

3.4 MILLING SIMULATION WITH NEW MODEL

A block diagram of the milling simulation using the new milling model is shown in Fig. 8. The main program (see left block diagram in Fig. 8) is similar to the simulation of the traditional model described in Section 3.2 (see Fig. 6). First, the process, model, and numerical parameters are defined. The main program then initiates the tool revolution loop. At each time step, values of θ_p, U_p, and V_p and vectors of $\boldsymbol{U}_{old}$, and $\boldsymbol{V}_{old}$ are sent to the chip thickness sub-program (see right block diagram in Fig. 8), where the chip thickness for the p^{th} tooth, ω_p, is calculated. Refer to Section 3.3 for a description of the process used in calculating ω_p. If ω_p is greater that zero, the forces in the flexible directions of the tool, F_x and F_y, are calculated using Eqs. (3) - (6); otherwise, the forces are set to zero. Equation (9), along with the states from the previous simulated time step, t - dt, are then used in calculating the states of the system for the current time, t. The current states are then saved and used in the calculation of the states for the next time step, t + dt. The main loop continuous until the simulated revolutions equals the predefined number of revolutions.

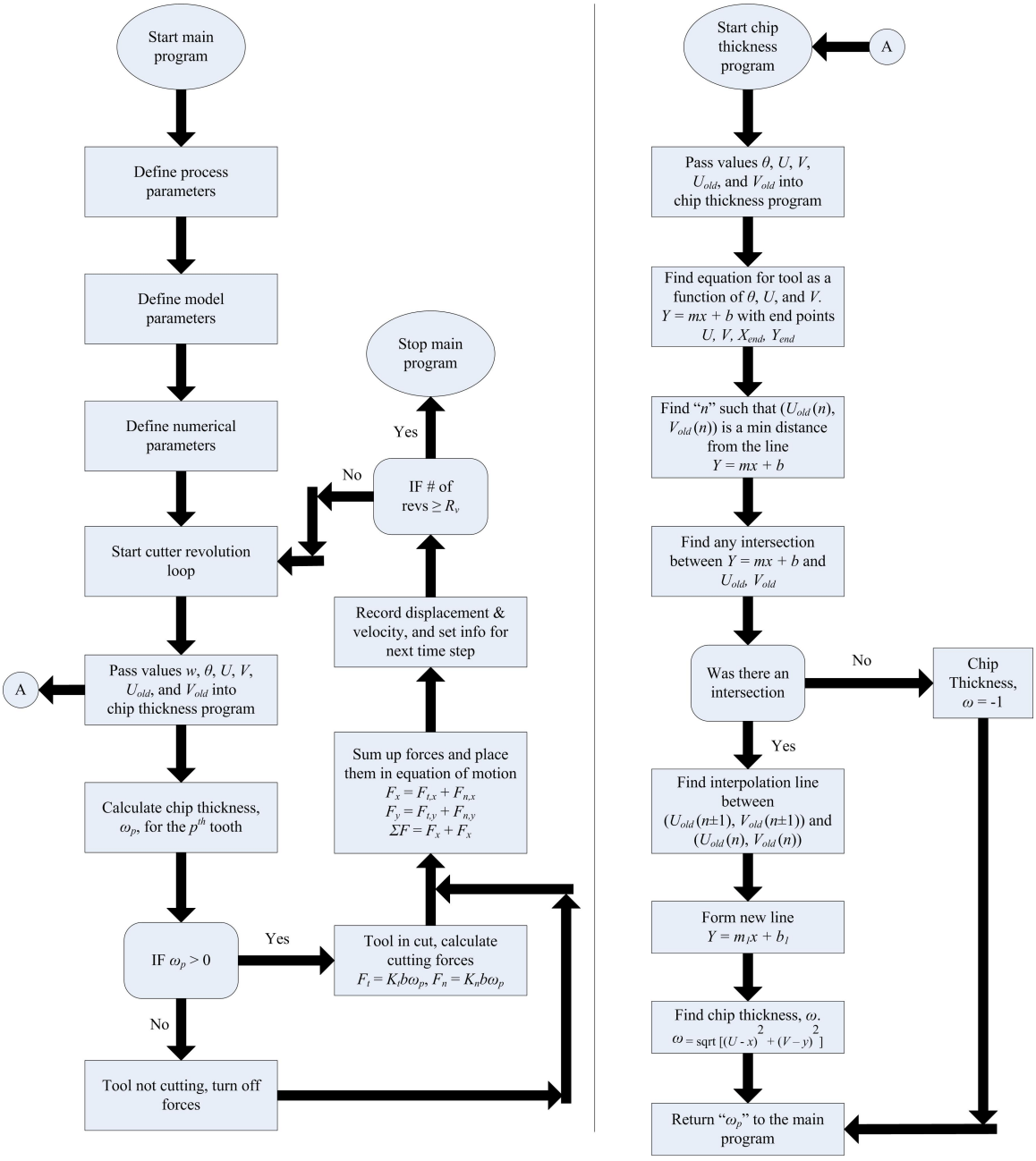

Fig. 8. Block diagram of the milling simulation using the new chip thickness calculation model [15].

CHAPTER 4 EXPERIMENTAL SETUP

In the following chapter, the experimental milling setup used in collection tool deflection data and tool period is discussed. The preliminary setup of the system including calibration of the sensors and experimental model parameter estimation procedures are also given. First, the milling (CNC) machine, sensor layout, and data acquisition (DAC) system used in obtaining experimental data are discussed in Section 4.1. The DAC system given here is used for obtaining all experimental results in the following chapters. The calibration process used for the tool deflection sensors (i.e. capacitance sensors) is outlined in Section 4.2. Finally, static and dynamic model parameter testing procedures and results are given in Section 4.3.

4.1 SYSTEM CONFIGURATION

A 3 DOF Cincinnati CFV1050^{si} CNC machine with a maximum spindle speed of 20,000 rpm is used as the testing platform for all milling experiments. The table of the CNC machine moves in the x and y-directions, and the spindle moves in the z-direction (see photo (i) in Fig. 9 for axis directions). A 2-flute Robbjack EX-206-16 milling tool is mounted into the spindle of the CNC machine via a polygonal tool holder. The tool has a cutting radius of 6.35 mm, a shank radius of 5.71 mm, an overall length of 152.4 mm, a neck length of 101.6 mm, and a 30-degree helix angle. The tool extends from the tool holder approximately 100 mm. This tool has a long reach (i.e. long neck length); therefore, it is more susceptible to chatter. A 7050-T7451 aluminum workpiece is bolted to the table of the CNC machine. The workpiece is approximately 986 mm long, 152 wide, and 50 mm thick.

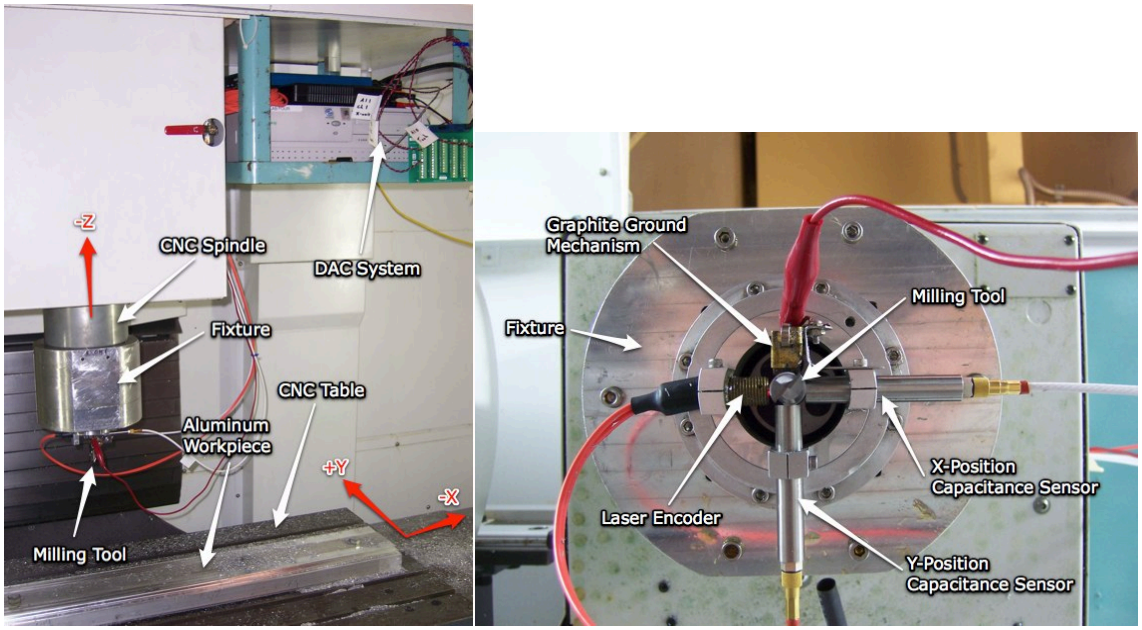

(i) (ii)

Fig. 9. (i) Experimental milling system (axis directions are shown in red). (ii) Experimental sensor arrangement/layout.

An underneath view of the milling tool and sensor configuration is shown in photo (ii) of Fig. 9. A custom aluminum fixture is mounted on the spindle of the CNC machine (see plots (i) and (ii)). Two capacitance sensors are clamped to the fixture 90 degrees apart, which provide tool displacement readings in the x and y-directions. The centers of both capacitance sensors are positioned perpendicular to the centerline of the tool. A laser tachometer is clamped into the fixture 180 degrees from the x-position capacitance sensor. White adhesive paper is placed on the tool to reflect the laser beam back to the sensor (no reflection occurs when the laser hits the bare metal surface of the tool). The signal from the tachometer is square wave whose frequency represents the rotational speed of the tool. The DAC system consists of a real-time microcontroller with 6831 FPGA data acquisition. The signals from the capacitance sensors and tachometer are sampled at a rate between 13,000 and 15,000 Hz depending on the spindle speed of the CNC machine. A higher sampling rate is required at higher spindle speeds to achieve

the desired number of samples per tool revolution. The capacitance sensor readings are stored as 16 bit analog signals, where as the tachometer reading is stored as a digital signal.

4.2 SENSOR CALIBRATION

The calibration setup for the capacitance sensors is shown in Fig. 10. The tool is mounted into the spindle of the CNC machine, and the capacitance sensor is securely clamped to the CNC table. The centerline of the sensor is aligned perpendicular to the centerline of the tool. The sensor is positioned above the fluting of the tool in approximately the same location where it is mounted for experimental tests. At the start of the calibration process, the tool and capacitance sensor are touching. The CNC table, on which the sensor is mounted, is then moved in the negative *x*-direction approximately 0.0762 mm (see Fig. 10 for *x*-axis direction). The voltage signal from the capacitance sensor is collected with the DAC system and saved to the laptop. The CNC table is then moved another 0.0762 mm in the negative x-direction, where the capacitance sensor signal is once again measured. This procedure is repeated until the distance between the tool and sensor approaches the maximum range of the sensor (i.e. 1 mm). The same calibration process is performed for the second capacitance sensor. Once all data is collected, the calibration curves (see Fig. 11) can be constructed. Finding the slope of first-order polynomials fit through the data in Fig. 11 results in calibration constants of 10.1874 and 10.9206 V/mm for the *x* and *y*-direction capacitance sensors, respectively.

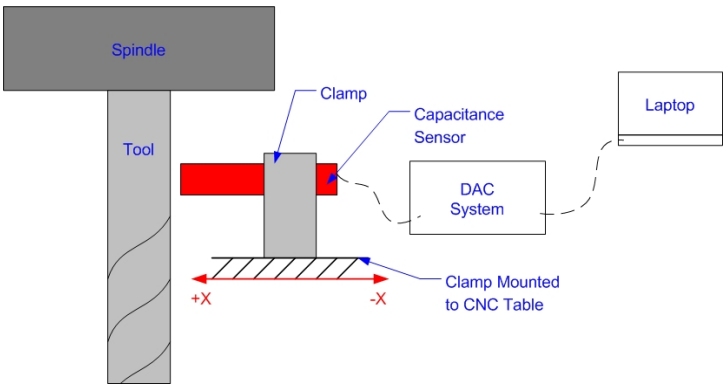

Fig. 10. Schematic of the capacitance sensor calibration. The *x*-direction of the CNC table is given in red.

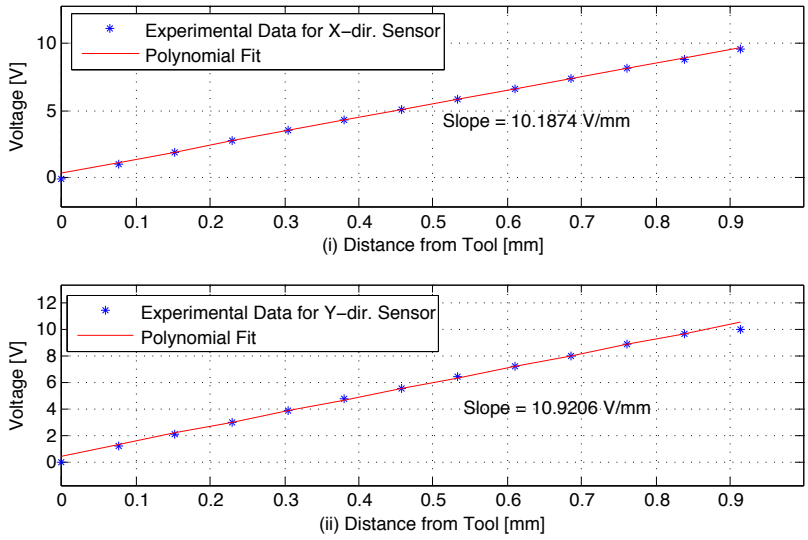

Fig. 11. Calibration curves for the capacitance sensors: (i) *x*-direction sensor, (ii) *y*-direction sensor.

4.3 MODEL PARAMETER ESTIMATION

To simulate the dynamics of a given milling process, the model parameters (i.e. the mass, m, damping, c, and stiffness, k) of the system must first be estimated. Two separate tests are performed in estimating the model parameters. The first is a static load test used in calculating the stiffness of the tool (see Fig. 12 for a schematic of the static load test). A 222 N spring scale is used to apply a constant force to the tip of the tool.

The spring scale is connected to the tool tip via a coupler and setscrew. A capacitance sensor (in this case the *x*-directional capacitance sensor) is placed on the opposite side of the tool, 180 degrees from the applied force. As a known force is applied via the spring scale, the voltage signal from the capacitance sensor is recorded with the use of a volt meter. The calibration constant for the *x*-directional capacitance sensor is used in converting the voltage signal to a corresponding tool deflection. The plot in Fig. 13 shows the relation between various force magnitudes and tool deflections. Fitting a first-order polynomial through this data results in a slope (i.e. a stiffness) of 11.9×10^5 N/m.

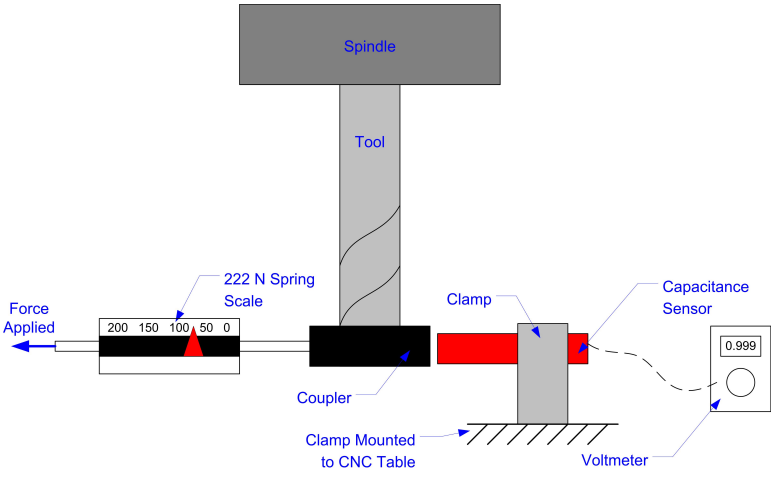

Fig. 12. Schematic of the static load test.

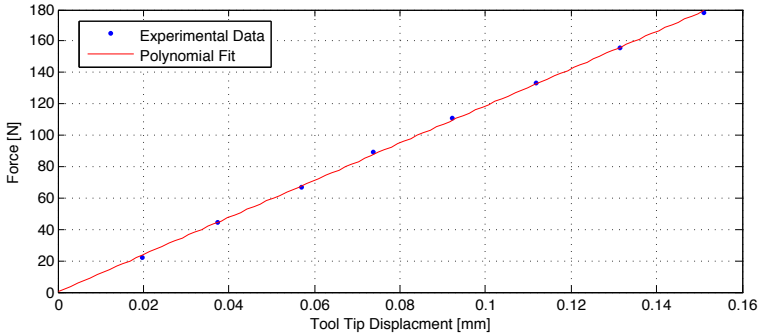

Fig. 13. Experimental force versus displacement relation for the static load test.

The second testing procedure is a dynamic test used in determining the remaining model parameters (see Fig. 14 for a schematic of the dynamic test system). Similar to the static test, the dynamic model test is performed at the tool tip. A PCB model 086C02 impact hammer is used to excite the tool/spindle. An accelerometer is placed on the tool 180 degrees from the hammer impact to record the acceleration of the tool when excited. The voltage signals from the impact hammer and accelerometer are recorded via the DAC system. Once a given test is complete, the voltage data from the impact hammer and accelerometer are converted to values of force (N) and acceleration (m^2/s), respectively, with known calibration constants.

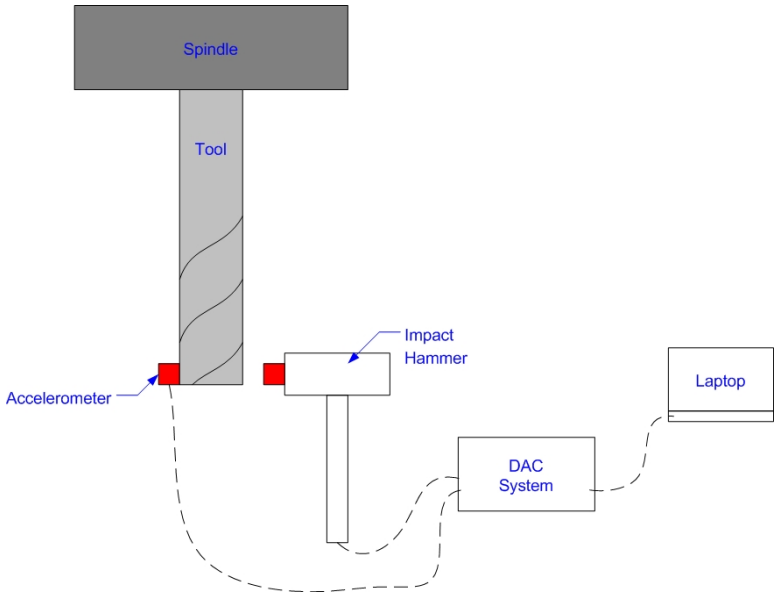

Fig. 14. Schematic of the model testing system.

The following is the 2-DOF equation of motion for the tool/spindle

$$m\ddot{X} + c\dot{X} + kX = F_h, \tag{15}$$

where $\ddot{X}$, $\dot{X}$, and X are the acceleration, velocity, and displacement of the tool tip, respectively, and F_h is the experimental force signal from the hammer test. Equation (15) can be rewritten as a transfer function of the form

$$a = \frac{F_h s^2}{ms^2 + cs + k}, \tag{16}$$

where a is the acceleration of the tool tip. At a given set of model parameters, the experimental force signal from the hammer test can be used along with Eq. (16) to calculate tool acceleration. The Matlab® command *fminsearch* is used to find a set of model parameters that minimizes the difference between the experimental acceleration signal and the one generated using Eq. (16). The stiffness, k, is assumed to be know with a value of 11.9×10^5 N/m (this value is calculated using the static load test given above). The mass, m, and damping, c, are allowed to vary until the difference between the experimental and simulated tool acceleration signals is minimized. The experimental and analytical acceleration responses are shown in Fig. 15 for a given hammer test. Once proper values of m and c are found, the analytical acceleration signal is shown to closely match the experimental acceleration data (see Fig. 15). After multiple tests, average values of m = 0.046 kg and c = 8.9 N-s/m are found to provide the best match between the analytical and experimental results. All simulated results in the following chapters assume the model parameters in the x and y-directions are equivalent (i.e. $m = m_{x,y}$, $c = c_{x,y}$, and $k = k_{x,y}$ in Eqs. (7) – (9)).

In the milling model and in the parameter estimation procedures given above, the milling tool is assumed to be a cantilever beam with a given mass, damping, and stiffness. The tool does not have a constant cross section due to the fluting of the tool. Here, the natural frequency of the tool from the dynamic parameter estimation technique (see Fig. 15) is compared with the analytic natural frequency derived for a cantilever beam with constant cross section. For a cylindrical cantilever beam, the natural frequency is given by Palm [49] as

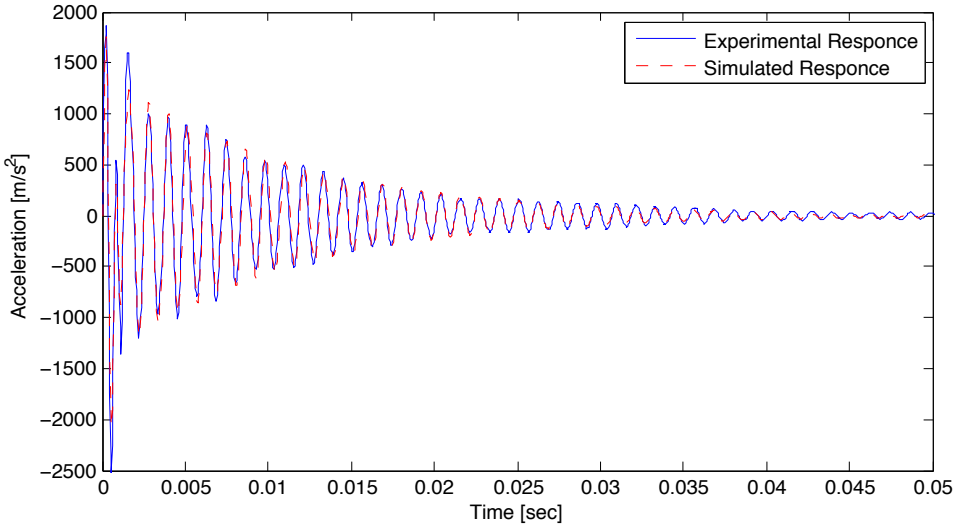

Fig. 15. Experimental and simulated acceleration response of the tool for a given hammer test.

$$\omega_n = \sqrt{\frac{k}{m}} = \sqrt{\frac{3EI}{0.23mL_b^3}}, \tag{17}$$

where E is the Young's Modules, L_b is the beam length, and I is the mass moment of inertia given by

$$I = \frac{\pi r_s^4}{4}, \tag{18}$$

where r_s is the radius of shaft. From the values of m and k found through the parameter estimation techniques given above, the natural frequency of a cantilever beam is found to be 810 Hz from Eq. (17). The tool used in this work has a neck length of 0.1016 m, a shaft radius of 5.71×10^{-3} m, a neck weigh of approximately 0.155 kg, and a Young's Modules of 500 GPa. Palm [49] approximates the effective mass of a cantilever beam as 0.23% of its actual mass. At an actual mass of 0.155 kg, the milling tool (when considered a uniform cantilever beam) has an effective mass of 0.357 kg, which is smaller than the value of m (0.046 kg) found via the parameter estimation techniques above. It is not expected that the actual effective mass of the milling tool match with that

of a uniform cantilever beam since the milling tool is not uniform due to the geometry of the flutes. Solving Eq. (17) using the actual tool properties (i.e. E, I, m, and L), a natural frequency of 921 Hz is found, which is 12% larger than the natural frequency found using the values of k and m from the parameter estimation techniques. From Fig. 15, the frequency of the experimental tool oscillations from the hammer test is shown to be 850 Hz, which falls between the natural frequency values calculated from Eq. (17). From this analysis, it is shown that the response of the milling tool behaves very similar to a cantilever beam; however, the non-constant geometry of the tool does have an effect on the response.

Chapter 5 PRELIMINARY RESULTS

In this chapter, simulations form the traditional and new milling models discussed in Chapter 3 are performed and compared with experimental results. The convergence of both mathematical models are first tested in Section 5.1 to find the number of steps-per-revolution required for the solution of each model to converge. In Section 5.2, the calculated chip thicknesses from the traditional and new milling models are compared to show how the two models differ. Simulations are then compared with experimental results in Section 5.3 to verify the accuracy of the mathematical models (this chapter also experimentally and analytically validates the existence of hysteresis in the milling operation). In Section 5.4, a set of experimental and simulated results are given to show the possibility of equilibrium jumps (i.e. jumps from chatter-free to chatter equilibrium) within the hysteresis region of the system. Finally, Section 5.5 gives a summary of the results. All results in this chapter are for an up-milling process with the following conditions: Ω = 15,000 rpm, r = 0.382 mm, f = 0.0635 mm/tooth, and b varies between 0 and 6 mm. All simulations use the model parameters experimentally obtained in Section 4.3 (m = 0.046 kg, c = 8.9 N-s/m, and $k = 11.9\times10^5$ N/m).

5.1 CONVERGENCE OF THE MATHEMATICAL MODELS

Before simulated and experimental results can be compared, a proper number of revolutions and steps-per-revolution must be chosen that provide a converged analytical solution. The number of tool revolutions is chosen to match the experimental tests. At a feed rate of 0.127 mm/rev and workpiece length, L, of 986 mm, the tool rotates

approximately 7,765 times over the length of the workpiece. For all experimental results, the depth of cut, b, is increased from 0 to 6 mm or decreased from 6 to 0 mm over the length of the workpiece. To match the experimental tests, each simulation contains approximately 1,290 revolutions for every 1 mm change in b. For example, if a given simulation has a 2 mm change in b, $2 \times 1{,}290 = 2{,}580$ revolutions are simulated. To find converged analytical solutions, the steps-per-revolution are varied from 100 to 1200 for the traditional and new models (the time step of a given simulation can be calculated by knowing the steps-per-revolution and spindle speed). The bifurcation diagrams in Fig. 16 show the once-per-tooth-pass tool deflection in the x-direction, X_n, as a function of b for the new milling model at 400, 600, and 800 steps-per-revolution. As the number of steps increase, the bifurcation point (i.e. the point at which the X_n data diverges) begins to converge onto a given depth of cut, b.

The bifurcation points from the traditional and new models over the full range of steps are given in Table 2. Referring to the bifurcation points at 1200 steps-per-revolution as a reference (i.e. the converged solution), the error in the location of the bifurcation points is shown to decrease as the steps are increased, which is expected. However, increasing the number of steps increases the computational time significantly (this is especially true for the new model); therefore, the fewest number of steps is desired. At 800 steps per revolution, both simulations have a bifurcation error of only 0.02% (see Table 2). The computational time for each model is significantly less at 800 steps than at 1200 steps. Therefore, 800 steps-per-revolution are used in generating all simulated results from this point forward.

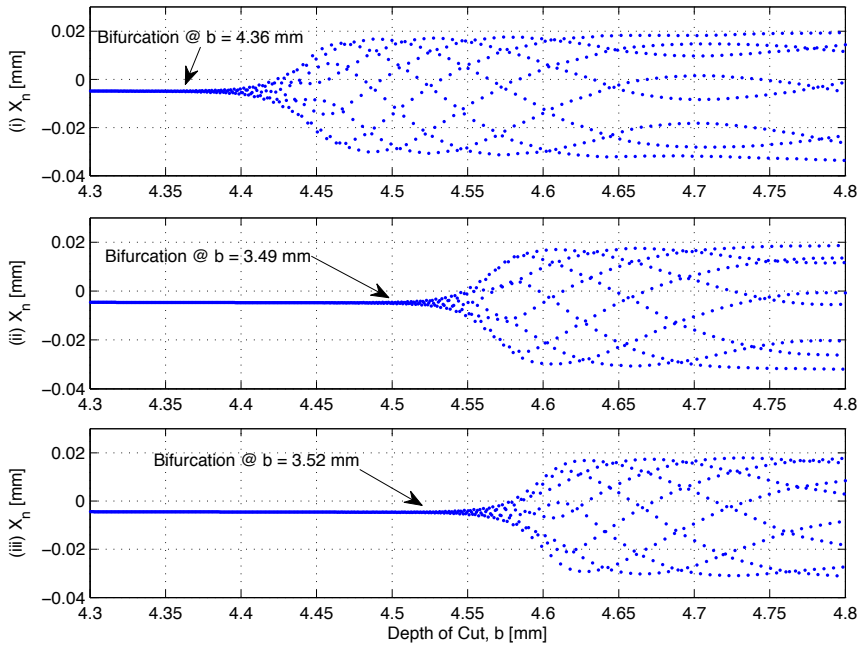

Fig. 16. Simulated once-per-tooth pass tool displacement, X_n, for an increasing b. Results are from the new milling model: (i) 400 steps-per-revolution, (ii) 600 steps-per-revolution, (iii), 800 steps-per-revolution.

Table 2. Bifurcation points at different number of steps-per-revolution.

	Bifurcation Point [mm] – Error [%]	
Steps per rev.	**Traditional Model**	**New Model**
100	4.92 – 3.1	4.85 – 7.1
200	4.71 – 1.3	4.61 – 1.8
400	4.74 – 0.6	4.36 – 3.8
600	4.75 – 0.4	4.49 – 0.9
800	4.76 – 0.2	4.52 – 0.2
1200	4.77 - 0	4.53 – 0

5.2 CHIP THICKNESS MODEL COMPARISON

Plots (i) and (ii) of Fig. 17 show the chip thickness of tooth #1, ω_1, and tooth #2, ω_2, respectively, for the traditional and new milling models over one revolution of the tool (the tool is chatter-free in these plots). While the tool is chatter-free, ω_1 and ω_2 increase linearly until the tool leaves the workpiece. The chip thicknesses from the new

and traditional models have similar slopes; however, the magnitudes of ω_1 and ω_2 from the new model are slightly larger than those calculated using the traditional model. As discussed in Section 3.3, the new model accounts for the trochoidal motion of the tool (i.e. accounts for the feed of the tool past the workpiece), which results in a slight increase in ω_1 and ω_2. The traditional model assumes circular tool motion.

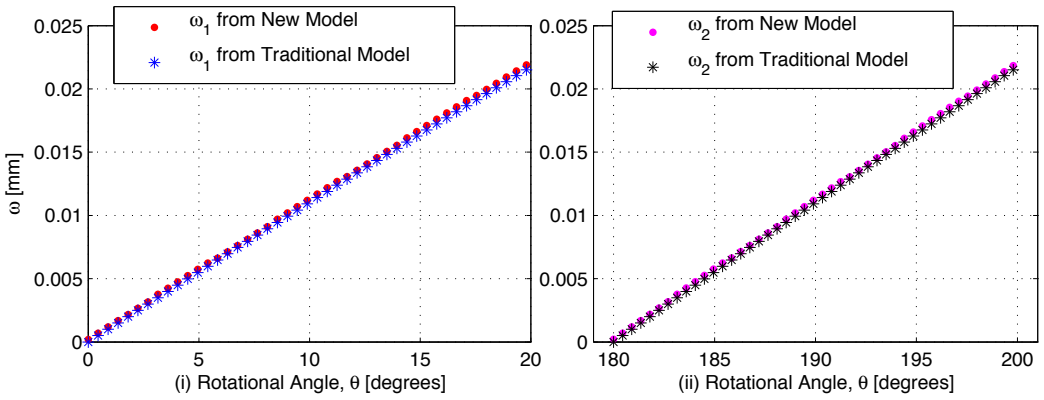

Fig. 17. Simulated chip thickness results for an increasing *b* from the new and traditional milling models in the chatter-free region: (i) chip thickness for tooth #1, (ii) chip thickness for tooth #2.

The plots in Fig. 18 give ω_1 (see plot (i)) and ω_2 (see plot (ii)) for one complete revolution while the tool undergoes chatter. During chatter vibrations, ω_1 and ω_2 no longer follow a linear path. As shown in plot (i), ω_1 from the new model (see red dot data) has a relatively small magnitude as tooth #1 passes through the workpiece. When ω_1 is small (i.e. when tooth #1 only removes a small amount of material from the workpiece), the chip thickness for the consecutive tooth pass (in this case ω_2) will in most cases have a much larger magnitude than ω_1. The magnitude of ω_2 in plot (ii) (see magenta dot data) is in fact significantly larger than ω_1. Further inspecting the chip thicknesses within the chatter region (see Fig. 18), the entry and exit angles begin to vary significantly. Even during chatter vibrations, the entry and exit angles of the traditional model must fall within the specified range given by Eq. (10). Specifically, the traditional

model requires the entry angle for tooth #1 and #2 to be greater than or equal to 0 and 180 degrees, respectively. Referring to plot (ii) of Fig. 18, ω_2 for the new model (see magenta dot data) is shown to enter the workpiece at an angle less than 180 degree. This ability to enter and/or exit the workpiece at any given angle is an obvious advantage the new model has over the traditional model.

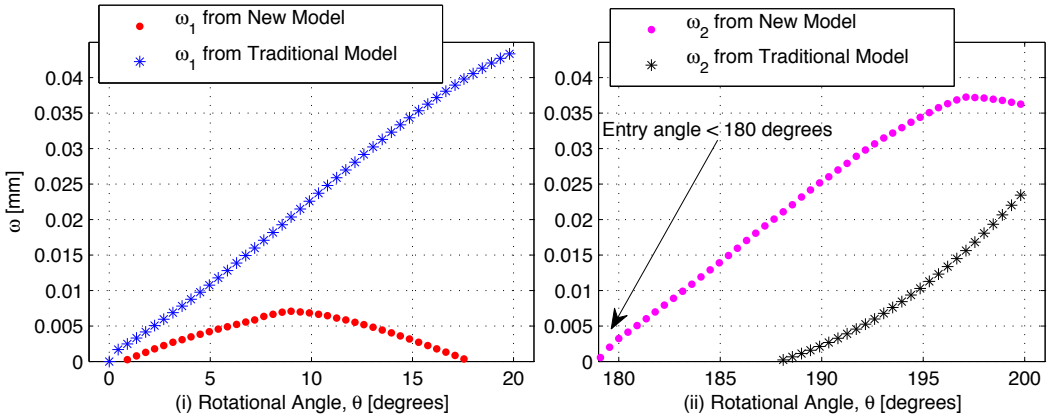

Fig. 18. Simulated chip thickness results for an increasing *b* from the new and traditional milling models in the chatter region: (i) chip thickness for tooth #1, (ii) chip thickness for tooth #2.

5.3 MODEL VERIFICATION

To explore the subcritical nature of milling bifurcations (see milling bifurcation diagram in Fig. 2), two analytical and experimental cases are considered. The first case has an increasing depth of cut (i.e. *b* slowly increases from 0 to 6 mm over the length of the workpiece), and the second case has a decreasing depth of cut (i.e. *b* decreases from 6 to 0 mm over the length of the workpiece). By slowly varying *b*, a quasi-static system is approximated, though which the depth of cut that causes a change in the stability of the milling system can be found. When *b* is increased, the system is initially chatter-free and then transitions into chatter once some value of *b* is reached (the bifurcation point occurs at the depth of cut at which chatter forms). When *b* is decreased, the system initially

contains chatter and then becomes chatter-free at some value of b (the bifurcation point occurs at the depth of cut at which the system becomes chatter-free).

The left-most plots in Figs. 19 and 20 show experimental and analytical bifurcation diagrams (i.e. the once-per-tooth pass displacement data in the x-direction, X_n, as a function of b) for an increasing and decreasing b, respectively. A Poincaré map at b = 4.75 mm is given to the right of each bifurcation diagram. A Poincaré map can be thought of as a cross-sectional view of the once-per-tooth-pass bifurcation diagram over a small range of b. To generate a Poincaré map, $X_n(t)$ is plotted verses $X_n(t\text{-}\tau)$, where τ is the time step between constitutive tooth passes. For example, the deflection of tooth #2 ($X_n(t)$) is plotted against the deflection tooth #1 ($X_n(t\text{-}\tau)$) for any given revolution. When the Poincaré map shows a single point over a small range of b, a single stable chatter-free equilibrium exists. However, a circular or oval shape indicates the existence of multiple stable chatter equilibrium.

Referring to Fig. 19, the experimental and analytical results show a sudden divergence of the X_n data. This is characteristic of a system suddenly transitioning from stable chatter-free equilibrium to stable chatter equilibrium points. The bifurcation diagrams from the experimental result (see plot (i)) and new model simulation (see plot (ii)) show similar bifurcation points at depths of cut near 4.52 and 4.53 mm, respectively. The traditional model (see plot (iii)), however, results in a bifurcation point at b = 4.82 mm, which is 0.24 mm larger than the experimental result. The Poincaré maps for the experimental result and new milling model both show an elliptical pattern representing multiple stable chatter equilibrium points at b = 4.75 mm (i.e. the location of the Poincaré maps). On the other hand, the Poincaré map for the traditional model shows a single

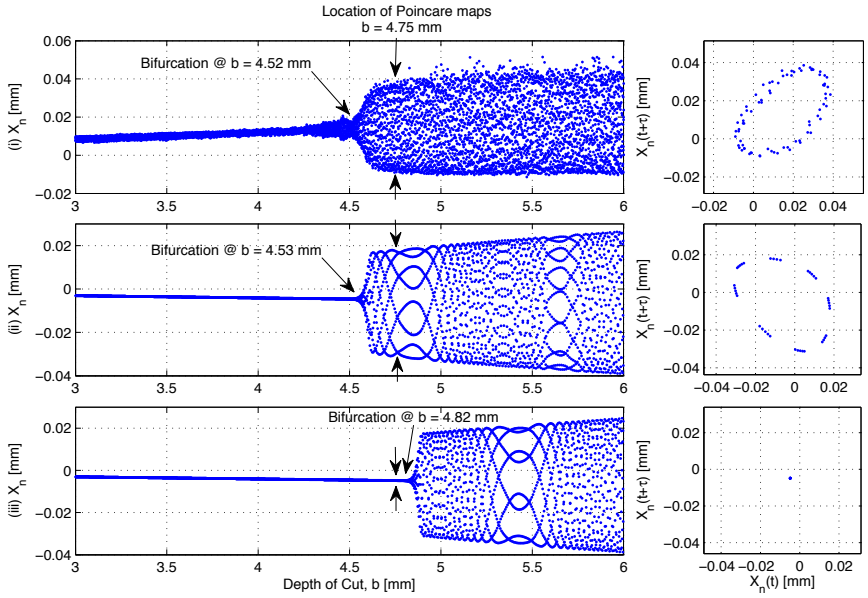

Fig. 19. Once-per-tooth-pass tool displacement, X_n for an increasing b: (i) experimental result, (ii) simulation with new milling model, (iii) simulation with traditional milling model. Poincaré maps at b = 4.75 mm are given to the right of each bifurcation diagram.

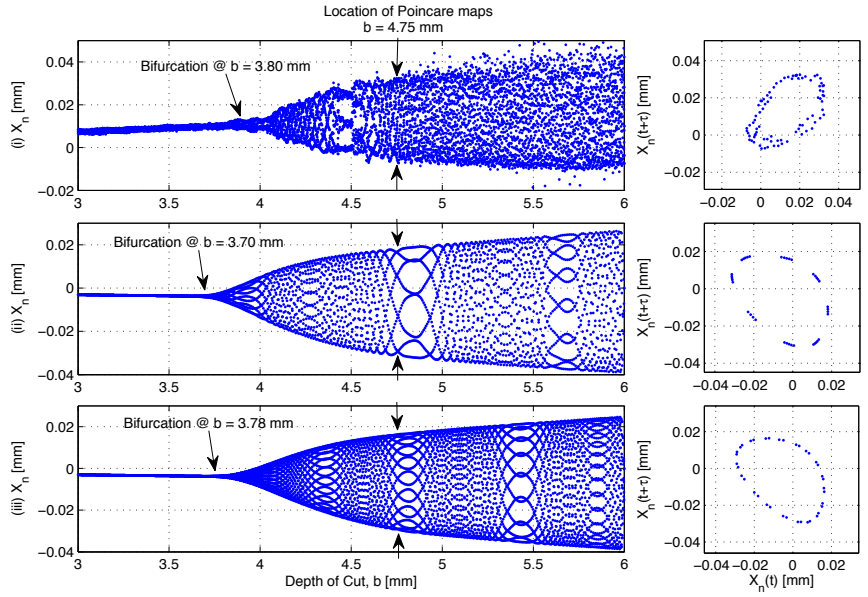

Fig. 20. Once-per-tooth-pass tool displacement, X_n, for an increasing b: (i) experimental result, (ii) simulation with new milling model, (iii) simulation with traditional milling model. Poincaré maps at b = 4.75 mm are given to the right of each bifurcation diagram.

stable chatter-free equilibrium point since the traditional model overestimated the bifurcation point and remains chatter-free at b = 4.75 mm.

For a decreasing b (see Fig. 20), the experimental and analytical results show a gradual convergence from stable chatter equilibrium onto the stable chatter-free equilibrium. Here, both models approximate the experimental bifurcation point within a depth of cut of 0.1 mm. When b is decreased over the length of the workpiece, the Poincaré maps of the experimental and simulated results all show multiple chatter equilibrium points at b = 4.75 mm. By comparing the case with an increasing b (see Fig. 19) with that of a decreasing b (see Fig. 20), the hysteresis in the milling operation can be seen in both experimental and simulated results. For an increasing and decreasing b, the experimental tests produced bifurcations at 4.52 and 3.80 mm, respectively. Therefore, the system contains both stable chatter and chatter-free equilibrium for depths of cut ranging from 3.8 to 4.52 mm. This experimentally verifies that the milling process contains a subcritical bifurcation (i.e. contains hysteresis)

5.4 EQUILIBRIUM JUMP WITH DISTURBANCE INPUT

The experimental and simulated bifurcation diagrams in Section 5.3 shows milling to contain a subcritical bifurcation; therefore, further testing can be performed to try and excite the system from stable chatter-free equilibrium to chatter equilibrium within the bifurcation range of the system (i.e. within depths of cut ranging from 3.8 to 4.52 mm for the experimental case). This is done for the case with an increasing b since the system must transition from chatter-free to chatter vibrations. To excite the system, a lip (see Fig. 21) is cut into the workpiece at b = 4.03 mm, which is within the bifurcation range of the system. The lip causes an increase in the radial immersion of the tool, which

produces larger chip thicknesses as the tool passes through the workpiece and, therefore, increases the forces on the tool. It is expected that these increased forces will cause the system to jump from stable chatter-free equilibrium to chatter equilibrium and remain in the chatter region as *b* continues to increase.

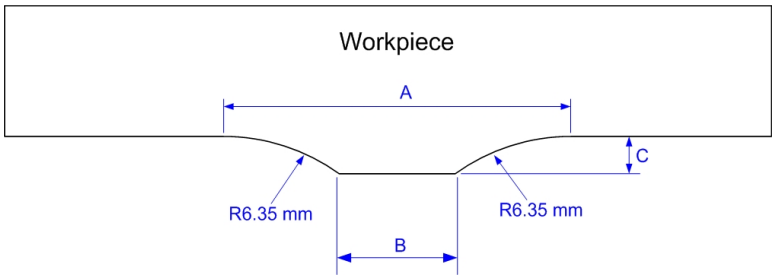

Fig. 21. Top view of the lip cut into the workpiece.

Table 3. Dimensions of the lip shown in Fig. 21.

	Lip Dimension		
	A [mm]	**B [mm]**	**C [mm]**
Test #1	3.81	0.254	0.254
Test #2	6.35	2.794	0.254

Two experimental tests are performed with different sized lips cut into the workpiece. Table 3 gives the dimensions of the lip for each test, and Fig. 21 shows an illustration of the lip from the top view. The maximum depth of the lip (see dimension C in Fig. 21) remains constant at 0.245 mm for each test. The depth of the lip causes an increase in the radial immersion of the tool from a nominal value of 0.381 mm to a max value of 0.635 mm at the peak of the lip. Dimension B in Fig. 21 determines the length over which the max radial immersion occurs (dimension A is dependent on B given the radius of the milling tool). Test #1 has a value of 0.245 mm for dimension B. However, test #1 does not cause an equilibrium jump in the experimental X_n data (i.e. the system remains chatter-free as the tool passes through the lip). Therefore, dimension B is increased to 0.2794 mm for Test #2. By increasing the time spent at the max radial

immersion, the system does jump from chatter-free to chatter equilibrium (i.e. the system experiences a bifurcation). As b continues to increase, the tool remains in a chatter vibration state. Experimental and analytical results are shown in plots (i) and (ii) of Fig. 22, respectively, for lip test #2. As shown in Section 5.3, the new model is better able to predict the experimental bifurcation points; therefore, only the new model is compared to the experimental lip test results in Fig. 22.

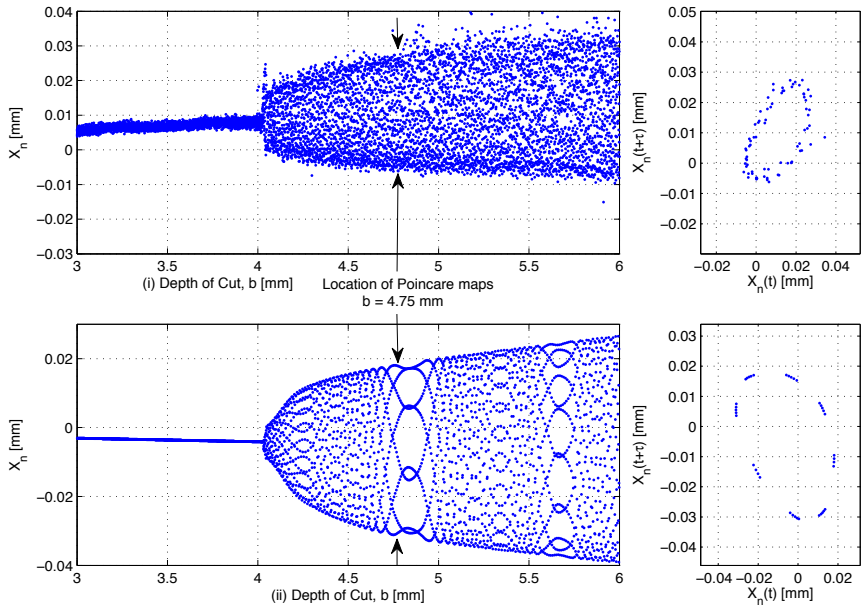

Fig. 22. Once-per-tooth-pass tool displacement, X_n, (left plots) for an increasing b and disturbance at b = 4.03 mm: (i) experimental result, (ii) simulation with new milling model. Poincaré maps at b = 4.75 mm are given to the right of each bifurcation diagram.

As shown in Fig. 22, the lip at b = 4.03 mm causes a bifurcation in both experimental and analytical results. To better represent the importance of the lip test results, respective experimental and simulated results are given in Figs. 24 and 24 for an increasing b, decreasing b, and increasing b with a disturbance are directly compared. For the experimental and simulated results for a decreasing b, the system contains chatter at b = 4.03 mm (see plot (ii) of Figs. 23 and 24). However, the milling operation is

chatter-free at this depth of cut when b is increased along the workpiece (see plot (i) of Figs. 23 and 24). As a result, if a disturbance occurs at b = 4.03 mm for the increasing b case (in this case a momentary increase in radial immersion), chatter vibrations may form (see plot (iii) of Figs. 23 and 24). To ensure that disturbances during a milling operation do not cause prolonged periods of chatter vibration, the depth of cut must be less than the lower bound of the hysteresis region. In other words, the depth of cut must be less than the bifurcation point found when b is decreased (see plot (ii) of Figs. 23 and 24), which occurs at b = 3.80 mm for the experimental result and b = 3.70 mm for the simulated result. For a constant depth of cut less than these values, a disturbance may cause a momentary jump from stable chatter-free to higher amplitude vibrations. However, the response will return to a chatter-free equilibrium once the disturbance has passed (this is shown analytically in Fig. 25 for a disturbance at b = 3.4 mm).

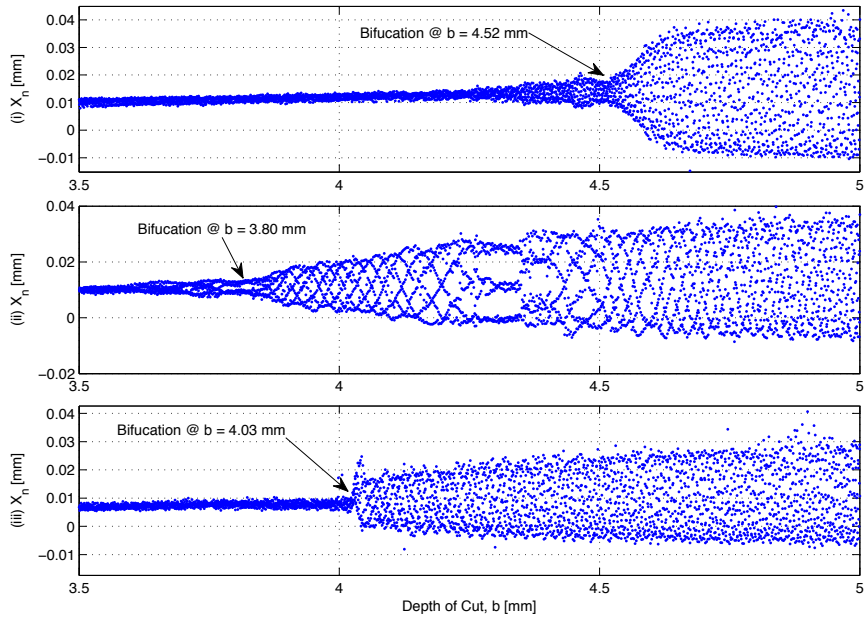

Fig. 23. Experimental once-per-tooth-pass tool displacement, X_n: (i) increasing b, (ii) decreasing b, (iii) increasing b with disturbance at b = 4.03 mm.

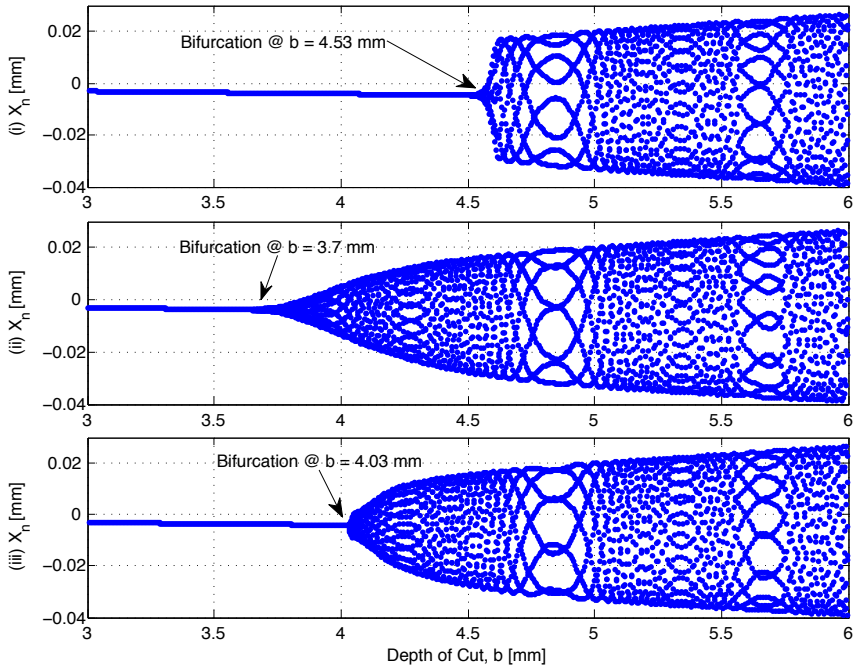

Fig. 24. Simulated once-per-tooth-pass tool displacement, X_n, (new milling model is used): (i) increasing b, (ii) decreasing b, (iii) increasing b with disturbance at b = 4.03 mm.

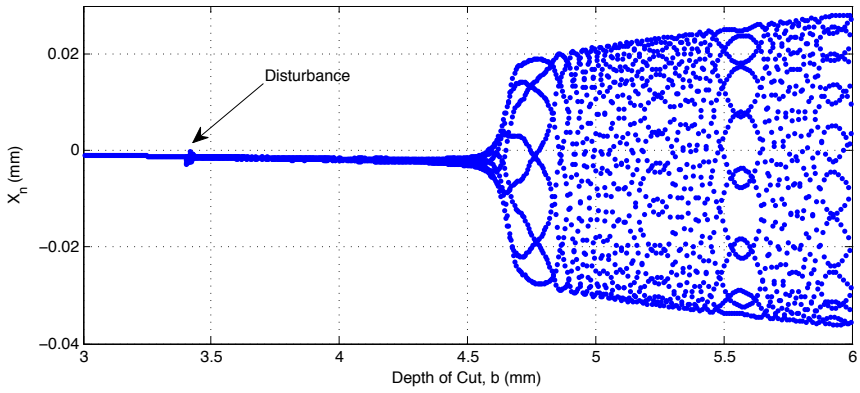

Fig. 25. Simulated once-per-tooth-pass tool displacement, X_n, for an increasing b and disturbance at b = 3.4 mm (new milling model is used).

5.5 RESULTS AND CONCLUSIONS

In this chapter, simulated results from the traditional and new milling models are compared with experimental results. The new milling model takes into account the trochoidal motion of the tool, which results in slightly larger simulated chip thickness

magnitudes compared to those calculated with the traditional model. The new model also has the ability to calculate chip thicknesses at any rotational angle of the tool, which is an obvious advantage over the traditional model. Furthermore, the new model is better able to predict the experimental bifurcation points for both an increasing and decreasing b. Therefore, all simulated results in the following chapters are generated using the new milling model. Through both simulated and experimental results, the milling system is shown to contain a subcritical bifurcation (i.e. is shown to contain hysteresis). Within the hysteresis range, a stability jump (i.e. a jump from chatter-free to chatter equilibrium) can be achieved through a disturbance to the system (this is verified both experimentally and analytically).

Chapter 6 TOOL AND SPINDLE RUNOUT

Up to this point, it is assumed that the centers of the tool and spindle are exactly aligned (i.e. no runout exists). However, in most milling systems, some sort of runout between the tool and spindle will exist. Offsetting the center of the tool and the center of the cutting teeth can simulate runout in the tool/spindle (i.e. the radius of tooth 1 is increased and the radius of tooth 2 decreased). Varying the tooth radii is also an effective way of simulating uneven tool wear and/or tooth chipping. To show how runout influences the dynamics of the tool, two separate simulations (one with and one without offset tooth radii) are compared with experimental results. The radii of the cutting teeth, r_1 and r_2, for the simulations are set at $[r_1, r_2]$ = [6.35 mm, 6.35 mm] and $[r_1, r_2]$ = [6.34938 mm, 6.35065 mm] for the case without and with runout, respectively. The radii r_1 and r_2 are decreased and increased by 0.01%, respectively, when simulating runout.

The effect of runout on the deflection of the tool, instantaneous chip thickness, and cutting forces are discussed in Sections 6.1, 6.2, and 6.3, respectively. Lastly, the results and conclusions are given in Section 6.4. All simulated and experimental results in this chapter are for an up-milling process with an increasing b, Ω = 15,000 rpm, h = 0.382 mm, f = 0.0635 mm/tooth. The simulated results are generated using the new milling model with model parameters obtained in Section 4.3 (m = 0.046 kg, c = 8.9 N-s/m, and $k = 11.9\times10^5$ N/m).

6.1 RUNOUT AND TOOL DEFLECTION

The plots in Fig. 26 give bifurcation diagrams for simulated results without and with runout (see plots (i) and (ii), respectively) and an experimental result (see plot (iii)). By comparing plots (i) and (ii), runout (i.e. a slight offset in the tooth radii) has little-to-no effect on the bifurcation point of the simulated results. The bifurcation point for each simulation occurs at approximately b = 4.55 mm. These bifurcation points closely match the experimental bifurcation point at b = 4.52 mm (see plot (iii)). The plots in Fig. 27 show the once-per-tooth-pass deflection data, X_n, in a portion of the chatter-free region (specifically from b = 0 to 2 mm). From this plot, the effect of runout on the once-per-tooth-pass deflection data, X_n, can be seen. With no runout (see plot (i) of Fig. 27), the X_n data follows a straight line. In other words, the displacement of tooth #1 and #2 in the x-direction (at a given b) are the same at some rotational angle, θ. In other words, the tool displacement has a period of 1/2 revolution when runout is not present. Offsetting the tooth radii, however, results in different displacement magnitudes every 1/2 revolution (see plot (ii) of Fig. 27). The difference in the X_n data increases as b increases. This results in what looks like a sideways 'V' in the X_n data. Similar to the simulated result with runout, the experimental result (see plot (iii) of Fig. 27) also shows differences in the X_n data for tooth #1 and #2.

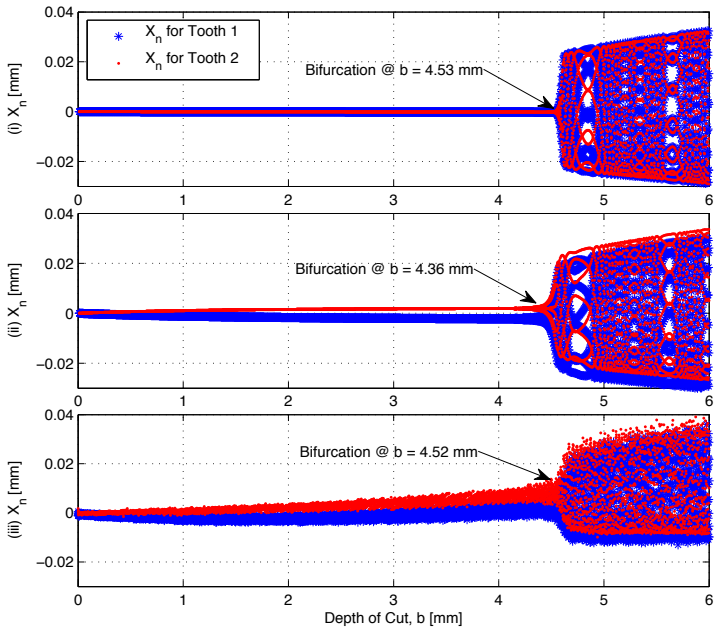

Fig. 26. Once-per-tooth-pass displacement, X_n, for an increasing b: (i) simulation without runout, (ii) simulation with runout, (iii) experimental result.

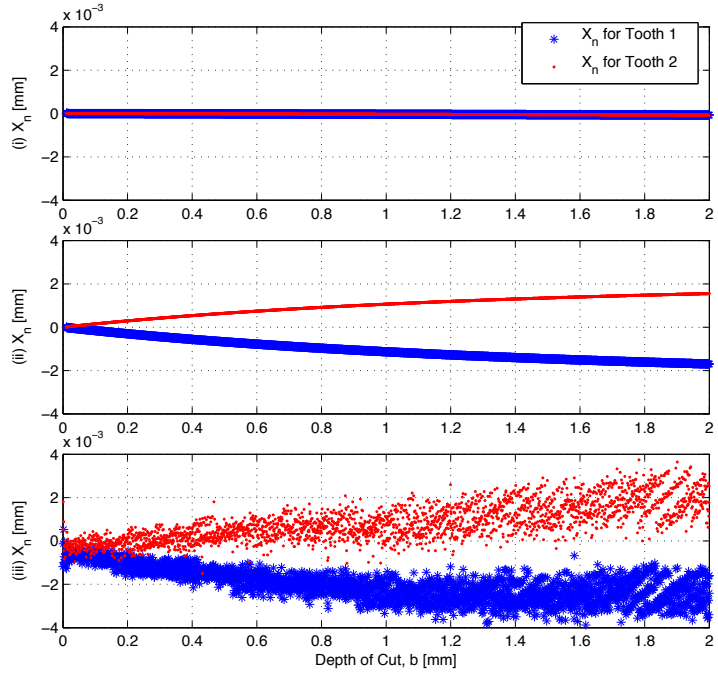

Fig. 27. Once-per-tooth-pass tool displacement, X_n, for an increasing b: (i) simulation without runout, (ii) simulation with runout, (iii) experimental result.

To better visualize the changes in the tool motion brought about by runout, Fig. 28 shows two complete revolutions (i.e. 720 degrees of rotation) at b = 3.5 mm, which is within the chatter-free region shown in Fig. 26. Without runout (see red dashed line in Fig. 28), the displacement amplitudes indicated with arrows are identical (these amplitudes are positioned 180 degrees apart). Furthermore, it can be shown that at any rotational angle, the deflection of the tool is repeated every 180 degrees (i.e. the displacement of the tool has a period of 1/2 revolution). However, when runout exists (see blue dashed line in Fig. 28), changes in the tool displacement begin to occur. This is especially evident when comparing the deflection amplitudes at 195 and 375 degrees (see point B). The offset in the tooth radii causes the amplitudes at 195 and 375 degrees to decrease and increase, respectively. There is also a change in the magnitude of the larger deflection oscillations (see point A); however, this change is small when compared to the magnitude change at point B.

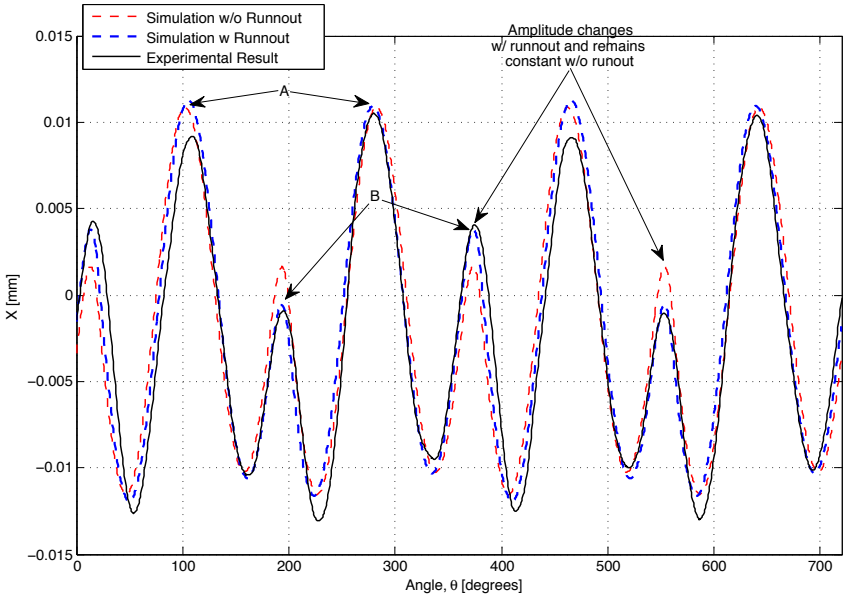

Fig. 28. Tool displacement, X, for 2 revolution (720 degrees) at b = 3.5 mm in Fig. 26 (chatter-free).

There are other small changes in the tool displacement caused by runout that can be seen by comparing the red and blue dashed data lines in Fig. 28. As a result of runout, the *x*-directional displacement only repeats every full revolution of the tool at a given *b* (i.e. the tool motion has a period of 1 revolution). The tool displacement for the experimental result (see black line in Fig. 28) more closely matches the simulated result with runout. Therefore, it can be assumed that there exists some sort of runout in the tool/spindle of the CNC machine used in collecting experimental data.

It should be noted that changing the angle at which the once-per-tooth-pass deflection data, X_n, in Fig. 27 is plotted can reduce the difference in the X_n values for tooth #1 and #2 (i.e. cause the red and blue data points in plots (ii) and (iii) to converge). For example, take the simulation with runout in Fig. 28 (see blue dashed line). The difference between X values at 100 and 280 degrees (see point A) are much smaller that the difference between X values at 195 and 375 degrees (see point B). Therefore, specific rotation angles can cause the X_n data in plots (ii) and (iii) of Fig. 27 to converge onto a straight line comparable to the simulated result without runout given in plot (i). However, when runout does not exist (i.e. when the tool displacement has a period of 1/2 revolution), the X_n data will always follow a single straight line regardless of the rotational angle the data is chosen from.

6.2 RUNOUT AND CHIP THICKNESS

The plots in Figs. 29 and 30 show the chip thicknesses, ω_1 and ω_2, for simulations with and without runout in the chatter-free and chatter cutting regions, respectively. In the chatter-free region (see Fig. 29), both ω_1 and ω_2 linearly increase at a slope of 1.096×10^{-3} mm/degree and reach a maximum magnitude of 0.02186 mm for the case

without runout. By offsetting the tooth radii (i.e. when runout exists), there is a decrease in the magnitude of ω_1 and an increase in the magnitude of ω_2. There is also an increase in the slope of ω_1 and a decrease in the slope of ω_2 due to runout. The differences in magnitude between ω_1 and ω_2 for the cases with and without runout are most predominant when the tool first enters the workpiece (i.e. when θ is slightly greater than 0 and 180 degrees for ω_1 and ω_2, respectively). As the tool continues trough the workpiece (i.e. as θ increases), the magnitude differences are reduced due to the changes in slope brought about by the offsets in the tooth radii. When compared to the case without runout, the slope of ω_1 increases to 1.179×10^{-3} mm/degree and the slope of ω_2 decreases to 1.010×10^{-3} mm/degree when runout is present (the slope of ω_1 and ω_2 both equal 1.096×10^{-3} mm/degree without runout). When the tool exits the workpiece (i.e. when ω_1 and ω_2 are at their maximum values), $\omega_1 = 0.02182$ mm and $\omega_2 = 0.02190$ mm for the case with runout ($\omega_1 = \omega_2 = 0.02186$ mm without runout).

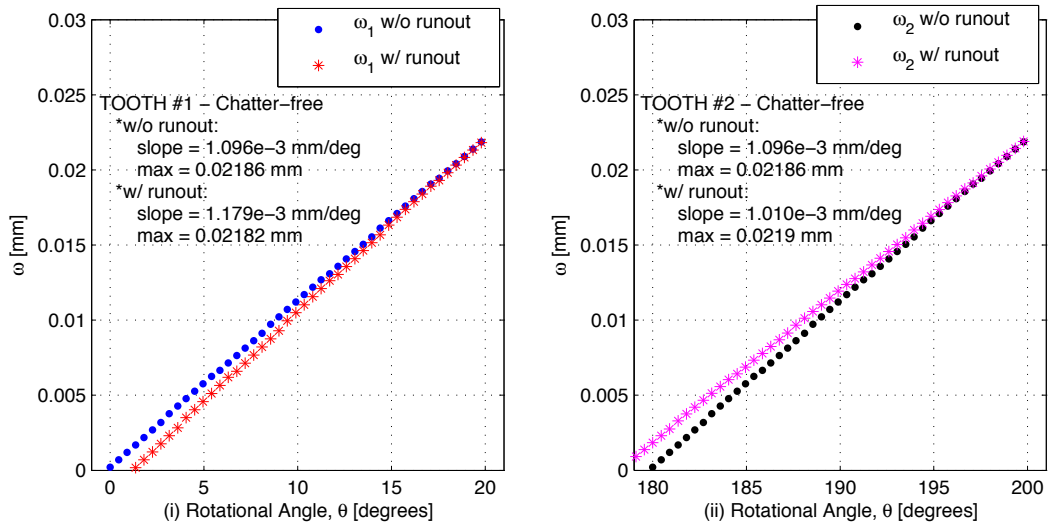

Fig. 29. Simulated chip thickness for the case with and without runout at b = 4 mm and Ω = 15,000 rpm (chatter-free vibrations exist): (i) chip thickness for tooth #1, (ii) chip thickness for tooth #2.

An overall decrease in ω_1 and increase in ω_2 is expected since the radii of tooth #1 and #2 are respectively decreased and increased when simulating runout. In other words, the cutting tooth with the larger radius (in this case tooth #2) will remove more material from the workpiece over a given tool revolution when chatter vibrations do not exist. As the tool undergoes chatter vibrations (see Fig. 30), ω_1 and ω_2 for the case with and without runout begin to differ more significantly. These large variations in chip thickness are a result of the different types of chatter vibrations and/or a very slight change in the bifurcation point caused by the offset in the tooth radii. Therefore, an "apples-to-apples" comparison between the case with and without runout cannot be made within the chatter vibration region.

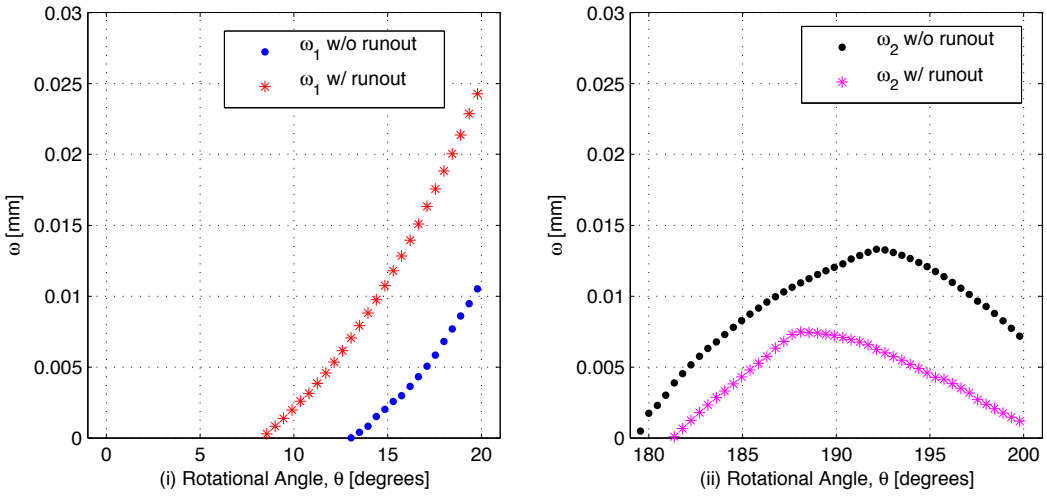

Fig. 30. Simulated chip thickness for the case with and without runout at b = 4.7 mm and Ω = 15,000 rpm (chatter vibrations exist): (i) chip thickness for tooth #1, (ii) chip thickness for tooth #2.

6.3 RUNOUT AND CUTTING FORCE

The instantaneous chip thickness has a direct effect on the forces applied to the tool tip (see Eqs. (3) – (6)). Therefore, the changes in ω_1 and ω_2 due to runout result in unequal forces applied to tooth #1 and tooth #2 as they pass through the workpiece. As

shown in Fig. 28, this force imbalance causes the period of the tool motion to double from 1/2 revolution to 1 full revolution. To better represent how changes in the force affect tool motion, two simulated results are given (one without and one with runout) that compare the displacement of the tool and forces applied to the tool over one revolution. Plot (i) of Fig. 31 shows the deflection of the tool in the x-direction, X, at b = 3 mm for the case without runout. The points at which the calculated force from the simulation is non-zero (i.e. the points where the tool is engaged in the workpiece) are shown as black dots along the X data curve. The force magnitude in the x-direction is given in plot (ii) of Fig. 31. The force signal for tooth #1 (see point A in plot (ii)) has a magnitude of -37.4 N and a slope of -1.696×10^{5} N/s, which is identical to the magnitude and slope for tooth #2 (see point B in plot (ii)). This is expected since the magnitude and slope of ω_1 and ω_2, which directly correlate to the force through Eqs. (3) – (6), is the same when runout does not exist (see plot (i) of Fig. 29 for chip thicknesses without runout). Since the force is uniform on tooth #1 and #2, the deflection of the tool, X, has a period of 1/2 revolution. Therefore, the maximum magnitude of X (1.413×10^{-3} mm) while the tool is engaged in the workpiece is the same for tooth #1 and #2 (see points A and B in plot (i) of Fig. 31).

Plots (i) and (ii) of Fig. 32 show the deflection of the tool, X, at b = 3 mm and the force magnitude in the x-direction, respectively, for the case with runout. The force signal for tooth #1 (see point C in plot (ii)) has a magnitude of -36.96 N and a slope of -1.815×10^{5} N/s, while tooth #2 (see point D in plot (ii)) has a magnitude of -37.84 N and a slope of -1.575×10^{5} N/s. The increases/decreases in the force magnitude and slope directly correlate to the changes in the chip thicknesses shown in Fig. 29 for the case with runout. The larger magnitude force applied to tooth #2, which is applied in the

negative x-direction, causes the tool to change its direction of motion from positive to negative more quickly than does the smaller magnitude force applied to tooth #1. In other words, the maximum magnitude of X while the tool is engaged in the workpiece is less for tooth #2 than for tooth #1 (see points C and D in plot (i), respectively). The maximum magnitude of X is 3.472×10^{-3} for tooth #1 (see point C) and -6.955×10^{-4} mm for tooth #2 (see point D). The different force magnitudes applied to tooth #1 and #2, and the resultant change in tool deflection, cause the period of X to increase to 1 revolution when runout exists.

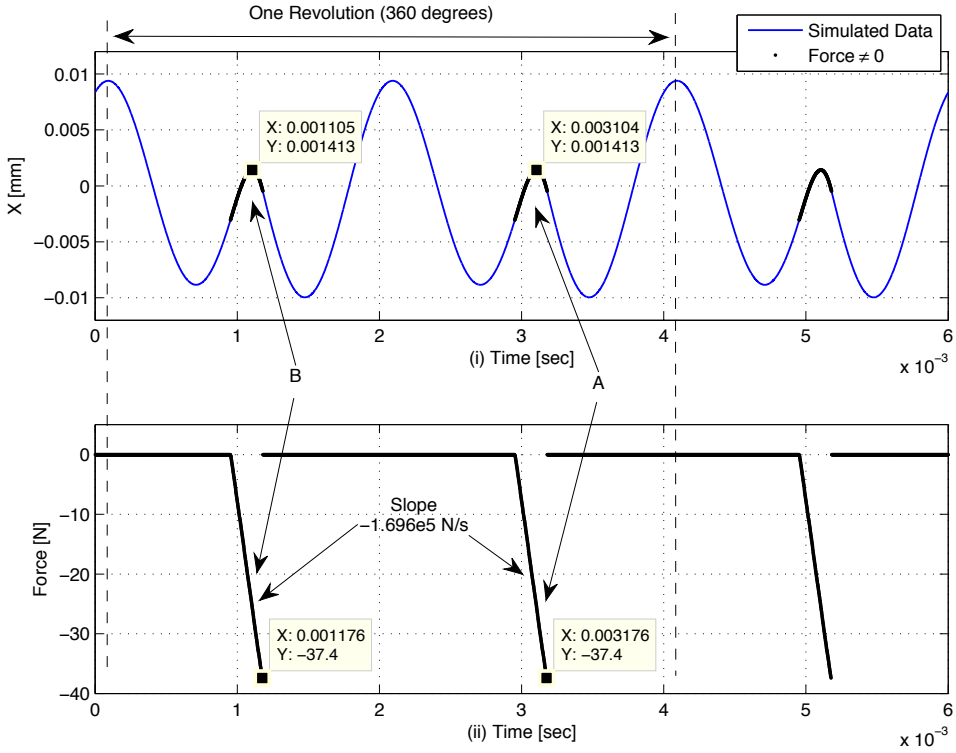

Fig. 31. (i) Simulated tool displacement, X, at b = 3 mm (chatter-free region) without runout. The points at which the calculated force is not zero (i.e. the points where the tool is engaged in the workpiece) are shown as black dots. (ii) Simulated force signal. Points A and B correspond to the respective regions tooth #1 and #2 are engaged in the workpiece.

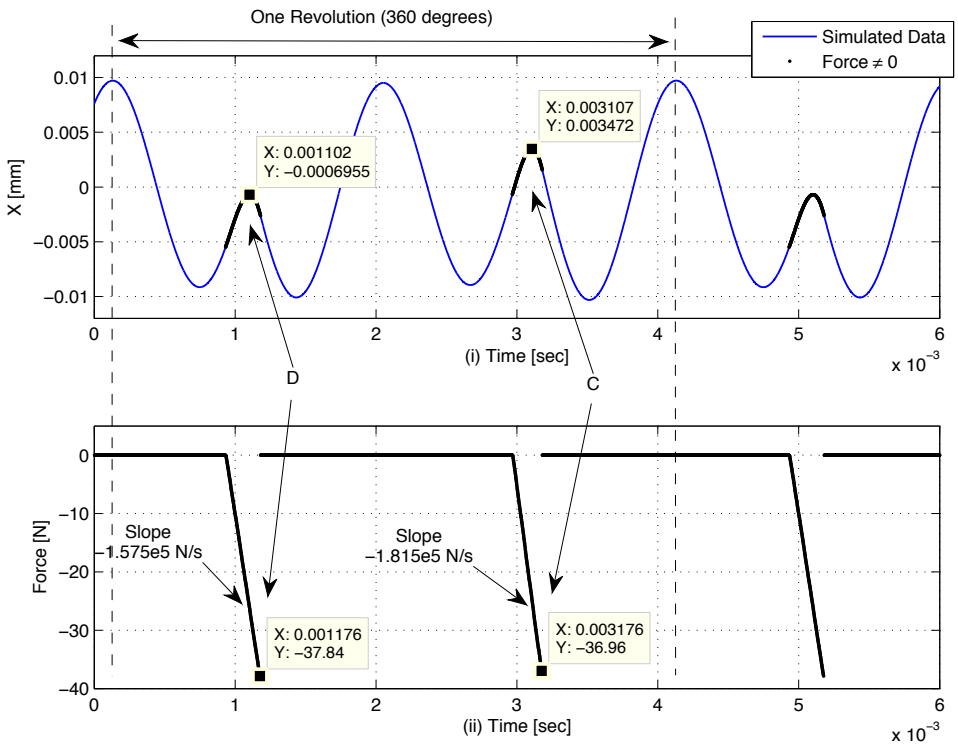

Fig. 32. (i) Simulated tool displacement, *X*, at *b* = 3 mm (chatter-free region) with runout. The points at which the calculated force is not zero (i.e. the points where the tool is engaged in the workpiece) are shown as black dots. (ii) Simulated force signal. Points A and B correspond to the respective regions tooth #1 and #2 are engaged in the workpiece.

6.4 RESULTS AND CONCLUSIONS

In this chapter, runout is simulated using the new milling model by offsetting the tooth radii. Simulations with and without runout (i.e. with and without tooth radii offsets) are compared with experimental results. Runout is shown to increase the period of tool motion from 1/2 to 1 full revolution. This increase in period is a result of unequal forces applied to tooth #1 and #2 as they are in contact with the workpiece. When runout is present, differences in the magnitude and slope of ω_1 and ω_2 cause the force applied to tooth #1 and #2 to differ. These non-uniform forces cause slight changes in the tool motion, resulting in an increase in the period of tool motion. By comparing the simulated

and experimental results given in this chapter, it can be concluded that runout exists in the tool/spindle of the CNC machine used in collecting experimental data.

Chapter 7 STATE AND PARAMETER ESTIMATION

For the experimental milling system given in Section 4.1, the measured outputs are the deflection of the tool in the x and y-directions. These measurements contain sensor noise, which can affect dynamic analysis of the system. Furthermore, exact parameters of the milling model (in this case the model parameters) are not often known to a high degree of accuracy. Experimental tests similar to those conducted in Section 4.3 can be used to estimate the model parameters of the system. However, these tests are time consuming, must be repeated when something in the system changes (such as a tool change or tool wear), and cannot be performed in real-time (i.e. during a milling operation). Therefore, state and parameter estimation methods based on measurements of different aspects of the system response are needed [30]. Such estimates can be obtained through the use of Kalman filters.

To eliminate sensor noise in the tool deflection measurements, a Kalman filter can be used. A Kalman filter is a multiple-input, multiple-output digital filter that can optimally estimate the states of a system (i.e. the position and velocity of the tool tip) based on its noisy outputs (i.e. measurements on the tool position) [38]. In addition, an extended Kalman filter (EKF), which is an expansion upon the basic Kalman filter, can estimate the model parameters (i.e. m, c, and k) by adding them to the system as additional pseudo states [33]. In the following chapter, a discrete Kalman filter algorithm and a discrete EKF algorithm are developed based on the mathematical milling model given in Chapter 2. The discrete Kalman filter algorithm along with state estimates of simulated and experimental tool deflection data are given in Section 7.1. The discrete

EKF algorithm is given in Section 7.2, where the accuracy of the state and parameter estimates are also tested on simulated and experimental data. The observabiltiy of each Kalman filter (i.e. the ability of each filter to calculate parameter and/or state estimates) is discussed in Section 7.3. Lastly, Section 7.4 provides a summary of the state and parameter estimation results.

A time step, T, of 10^{-6} seconds (i.e. a frequency of 10^6 Hz) is required to produce accurate parameter estimates within the EKF algorithm. Larger values of T result in errors in the parameter estimates, particularly the estimate of c. A larger time step ($T = 5\times10^{-6}$ seconds) can be used to accurately estimate only the states of the system using the discrete Kalman filter. However, the same value of T ($T = 10^{-6}$ seconds) is used for both Kalman filter algorithms for consistency. The frequencies of the experimental and analytical deflection data used within the Kalman filter algorithms are 1.33×10^3 and 2×10^5, respectively (this assumes Ω = 15,000 rpm). Therefore, the Matlab® command *interp1* is used to interpolate the simulated/experimental deflection data using cubic spline interpolation. The computational expense of the new chip thickness model is significantly larger than the traditional chip thickness model. Calculation time becomes important when computing parameter and/or state estimates on-line from experimental data; therefore, the traditional chip thickness model is used within the Kalman filter algorithms for estimating the instantaneous chip thickness (an on-line EKF parameter estimation technique is discussed in Section 11.2.1).

All simulated and experimental results in this chapter are for an up-milling process with Ω = 15,000 rpm, h = 0.382 mm, and f = 0.0635 mm/tooth. The new milling model is used in generating all simulated results. The experimental results in this chapter

are obtained with a different tool than those results given in Sections 5.3 through 6.3 (a chip in one of the cutting teeth of the previous tool resulted in this tool change). The new tool, which is the same part/model number as the previous one, is used for all experimental tests from this point forward. All efforts are taken to make the neck length (i.e. the length of the tool extending from the tool holder) of the new and old tools the same. However, it is inevitable that the model parameters of the tools will differ slightly. Therefore, new nominal model parameters are found using the static and dynamic testing methods shown in Section 4.3. Model parameter values for the new tool are m = 0.040 kg, c = 9.2 N-s/m, and $k = 11.5\times10^5$ N/m (the values found for the old tool are m = 0.046 kg, c = 8.9 N-s/m, and $k = 11.9\times10^5$ N/m).

7.1 DISCRETE KALMAN FILTER

The basic Kalman filter (in this case a discrete Kalman filter) is used to propagate the mean and errors of the states through time [33]. A mathematical model of the system and a measurement of the desired state, which contains noise, are used in finding an estimate that better represents the true value of the state. The predicted value of the state, which is found from the mathematical model, and the measurement of the state are weighted depending on uncertainty [33]. If the model of the system contains less uncertainty than the measured data, then the predicted state value will be weighted more heavily. The opposite is true if the measured state value contains less uncertainty than the model. Some trial-and-error is required to find the proper weighting values to tune the filter. The discrete Kalman filter algorithm used in estimating the states of the milling process is presented in Section 7.1.1. Kalman state estimates of simulated and experimental defection data are given in Section 7.1.2.

7.1.1 DISCRETE KALMAN FILTER ALGORITHM

As shown in the linear equation of motion of the milling tool in Eq. (9), the states of the system are the position and velocity in the x and y-directions. The states experimentally measured are the tool position values, X and Y. For simplicity, the discrete Kalman filter is designed for the states in the x-direction only. Therefore, the discrete version of Eq. (7) is the mathematical model, and the deflection measurement of the tool in the x-direction, X, is the state measurement. The discrete Kalman filter can easily be expanded to contain the states in both the x and y-directions but is not required for the purposes of this research. The discrete linear equation of motion in the x-direction at each time step, $k = 1, 2, \ldots$, is written as

$$\boldsymbol{x}_k = f_{k-1}(\boldsymbol{x}_{k-1}, \boldsymbol{u}_{k-1}\boldsymbol{w}_{k-1}) = \begin{bmatrix} x_{2,k-1}T + x_{1,k-1} \\ \frac{T}{m}(-x_{2,k-1}c - x_{1,k-1}k + u_{x,k-1} + w_{x,k-1}) + x_{2,k-1} \end{bmatrix}, \tag{19}$$

Where $\boldsymbol{x}$ is the state vector, $\boldsymbol{u}$ is the input vector, $\boldsymbol{w}$ is the process noise vector, T is the time step in seconds, u_x is the force input on the tool in the x-direction (F_x in Eq. (9)), w_x is process noise added to the system, and the states x_1 and x_2 are the respective displacement and velocity of the tool in the x-direction. The discrete measurement equation is given by

$$y_k = h_k(\boldsymbol{x}_k, \boldsymbol{v}_k) = \boldsymbol{H}_k\boldsymbol{x}_k + v_{x,k} = x_{1,k} + v_{x,k}, \tag{20}$$

where $\boldsymbol{v}$ is the measurement noise vector, v_x is the measurement noise, and $\boldsymbol{H}$ is the measurement matrix.

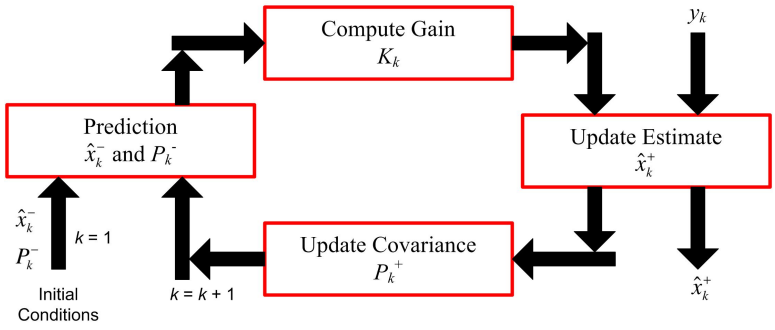

Fig. 33. Flow diagram of a Kalman filter and EKF [38].

A flow diagram of a Kalman filter is given in Fig. 33. The discrete Kalman filter equations, which are calculated at each time step, k, are given by Simon [33] as follows

$$\hat{\boldsymbol{x}}_k^- = \boldsymbol{F}_{k-1}\hat{\boldsymbol{x}}_{k-1}^+ + \boldsymbol{G}_{k-1}\boldsymbol{u}_{k-1}, \tag{21}$$

$$\boldsymbol{P}_k^- = \boldsymbol{F}_{k-1}\boldsymbol{P}_k^+\boldsymbol{F}_{k-1}^T + \boldsymbol{Q}_{k-1}, \tag{22}$$

$$\boldsymbol{K}_k = \boldsymbol{P}_k^-\boldsymbol{H}_k^T(\boldsymbol{H}_k\boldsymbol{P}_k^-\boldsymbol{H}_k^T + \boldsymbol{R}_k)^{-1}, \tag{23}$$

$$\hat{\boldsymbol{x}}_k^+ = \hat{\boldsymbol{x}}_k^- + \boldsymbol{K}_k(\boldsymbol{y}_k - \boldsymbol{H}_k\hat{\boldsymbol{x}}_k^-), \tag{24}$$

$$\boldsymbol{P}_k^+ = (\boldsymbol{I} - \boldsymbol{K}_k\boldsymbol{H}_k)\boldsymbol{P}_k^-, \tag{25}$$

where $\hat{\boldsymbol{x}}^-$ is a prior estimate of $\boldsymbol{x}$, $\hat{\boldsymbol{x}}^+$ is a subsequent estimate of $\boldsymbol{x}$, $\boldsymbol{P}^-$ denotes the covariance of the estimation error of $\hat{\boldsymbol{x}}^-$, $\boldsymbol{P}^+$ denotes the covariance of the estimation error of $\hat{\boldsymbol{x}}^+$, $\boldsymbol{K}$ is the Kalman filter gain matrix, $\boldsymbol{Q}$ is the covariance matrix of the process noise, and $\boldsymbol{R}$ is the covariance matrix of the measurement noise. The partial derivative matrices $\boldsymbol{F}$, $\boldsymbol{G}$, and $\boldsymbol{H}$, are given below.

$$\boldsymbol{F}_{k-1} = \left.\frac{\partial \boldsymbol{f}_{k-1}}{\partial \boldsymbol{x}}\right|_{\hat{\boldsymbol{x}}_{k-1}^+} = \begin{bmatrix} 1 & T \\ \dfrac{-k}{m}T & 1 - \dfrac{c}{m}T \end{bmatrix} \tag{26}$$

$$\boldsymbol{G}_{k-1} = \left.\frac{\partial f_{k-1}}{\partial \boldsymbol{u}}\right|_{\hat{\boldsymbol{x}}_{k-1}^{+}} = \begin{bmatrix} 0 \\ \dfrac{T}{m} \end{bmatrix} \tag{27}$$

$$\boldsymbol{H}_{k} = \left.\frac{\partial h_{k}}{\partial \boldsymbol{x}}\right|_{\hat{\boldsymbol{x}}_{k}^{-}} = \begin{bmatrix} 1 & 0 \end{bmatrix} \tag{28}$$

The process noise vector, $\boldsymbol{w}$, and the measurement noise vector, $\boldsymbol{v}$, both contain one variable each (i.e. $\boldsymbol{w} = [w_x]$ and $\boldsymbol{v} = [v_x]$). The dimension of the covariance terms $\boldsymbol{Q}$ and $\boldsymbol{R}$ are $i \times i$ and $j \times j$, respectively, where i is the length of $\boldsymbol{w}$ and j is the length of $\boldsymbol{v}$. Therefore, both $\boldsymbol{Q}$ and $\boldsymbol{R}$ have dimension 1×1. These covariance terms are used to weight the predicted and measured values of the state x_1. Decreasing the covariance of the process noise, $\boldsymbol{Q}$, increases the weight on the predicted state value (i.e. the estimate of X), while decreasing the covariance of the measurement noise, $\boldsymbol{R}$, increases the weight on the measured state value (i.e. X from experimental or simulated results).

The respective process noise, w_x, and measurement noise, v_x, terms in Eqs. (19) and (20) are set equal to zero (the only noise in the system is assumed to be contained within the measured value of X). During the first Kalman filter calculation (i.e. when $k = 1$), initial guesses of $\hat{\boldsymbol{x}}_1^+$ and $\boldsymbol{P}_1^+$ must be defined (see flow diagram in Fig. 33). The covariance matrix $\boldsymbol{P}^+$ is $l \times l$, where l is the number of states in the system. The initial guess of the covariance matrix, $\boldsymbol{P}_1^+$, is diagonal whose terms correspond to the convergence of each respective initial state estimate. Essentially, the diagonal terms in $\boldsymbol{P}_1^+$ determine how much each state estimate can change when k is small (i.e. determines the convergence rate of each state estimate). Generally, higher initial diagonal values increase the convergence rates of the states.

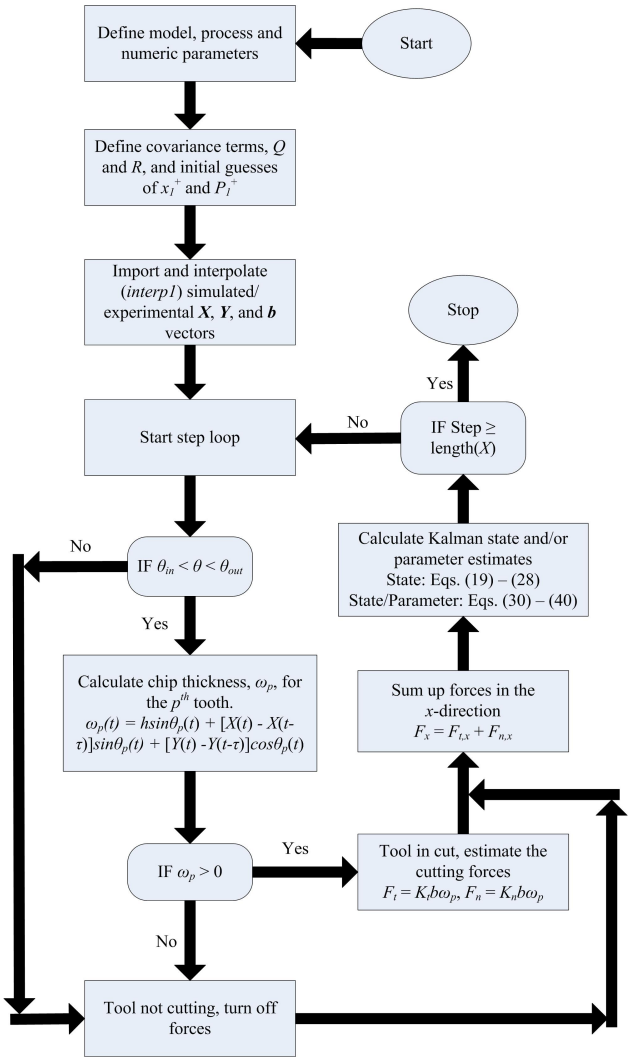

Fig. 34. Block diagram of the discrete Kalman and discrete extended Kalman state estimator.

The discrete Kalman filter algorithm is represented in block diagram form in Fig. 34. Process and numeric parameters are first defined. The covariance matrices, $\boldsymbol{Q}$ and $\boldsymbol{R}$, and an initial guess of $\hat{\boldsymbol{x}}_1^+$ and $\boldsymbol{P}_1^+$ are also defined. Vectors of simulated/experimental tool displacements, $\boldsymbol{X}$ and $\boldsymbol{Y}$, and depth of cut, $\boldsymbol{b}$, are then imported to the algorithm. The Matlab® command *interp1* is used to interpolate the simulated/experimental deflection data using cubic spline interpolation. The interpolated displacement values, along with the current angle of each cutting tooth, are then used in estimating the chip thickness at

each time step using Eq. (12). The chip thickness calculation requires knowledge of measured tool deflections in both the *x* and *y*-directions; therefore, the force estimates are dependent on measured tool deflections in both the *x* and *y*-directions. The force on the tool in the *x*-direction is then calculated using Eqs. (3) - (6). Since the Kalman filter is only used in estimating the states in the *x*-direction, force estimates are not required in the *y*-direction. The force estimate and current simulated/experimental *X* value are then used along with the discrete Kalman filter equations (see Eqs. (19) - (28)) in calculating $\hat{\boldsymbol{x}}^{+}$ (i.e. the updated estimate vector of the *x*-directional states, x_1 and x_2). The algorithm then proceeds to the next time step and continues within the main loop until the current step number equals the length of the interpolated $\boldsymbol{X}$ and $\boldsymbol{Y}$ data vectors.

7.1.2 STATE ESTIMATION WITH DISCRETE KALMAN FILTER

To show the accuracy of the state estimation algorithm, two sets or simulated deflection data (one with and one without runout) and one set of experimental deflection data are tested. To show the ability of the discrete Kalman filter to filter out noise within the system, a normally distributed random noise signal with a mean of zero and a variance of 0.5×10^{-3} mm is added to the simulated $\boldsymbol{X}$ and $\boldsymbol{Y}$ data vectors prior to state estimation. The initial state estimate vector, $\hat{\boldsymbol{x}}_1^{+}$, contains zeros (i.e. the initial estimates of the deflection and velocity of the tool are zero). The initial guess of the covariance matrix, $\boldsymbol{P}_1^{+}$, is given below.

$$\boldsymbol{P}_1^{+} = \begin{bmatrix} 10^{12} & 0 \\ 0 & 10^{12} \end{bmatrix} \tag{29}$$

The diagonal terms of $\boldsymbol{P}_1^+$ are chosen based on the convergence rate required for each state. Finally, values of the covariance terms, $\boldsymbol{Q}$ and $\boldsymbol{R}$, that provide the best balance between the predicted and measured values for both simulated and experimental results are found to be 0.1 and 5, respectively.

The state estimate of the tool deflection from noisy simulated data at b = 3 mm are shown in plot (i) of Figs. 35 and 36 for the case without and with runout, respectively. The state estimate is shown to match the actual simulated tool displacement in the x-direction (i.e. X without noise) quite well for both cases. The points at which the calculated force from the Kalman filter algorithm is non-zero (i.e. the points at which the cutting teeth are engaged in the workpiece) are shown as black dots along the estimated X curve in plot (i) of Figs. 35 and 36. Plot (ii) of these figures gives the magnitude of the calculated force (i.e. the force estimate found from the noisy deflection data using the traditional chip thickness model). Plot (ii) also gives the actual simulated force (i.e. the simulated force from the new chip thickness model). The noise signals added to the simulated deflection data cause slight errors in the calculated chip thickness, which are translated to errors in the force calculation (see black data points in plot (ii) of Figs. 35 and 36). The Kalman state estimate of X and the calculated force values for an experimental test at b = 3 mm are given in Fig. 37. Once again, the discrete Kalman filter is able to track the experimental X data quite well.

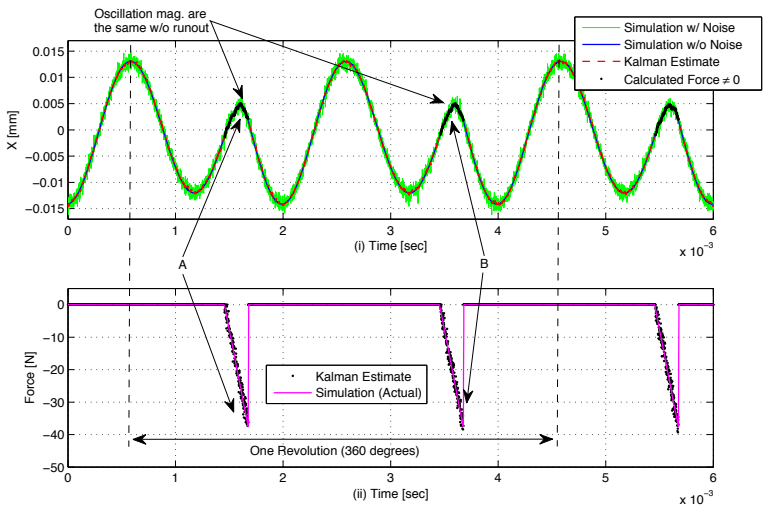

Fig. 35. (i) Kalman filter state estimate of noisy simulated tool deflection data, *X*, without runout at *b* = 3 mm. Simulated data with and without noise are given. The points at which the calculated force is not zero (i.e. the points where the tool is engaged in the workpiece) are shown as black dots along the estimated *X* curve. (ii) Calculated force signal found from the noisy *X* and *Y* simulated data compared with the actual simulated force signal.

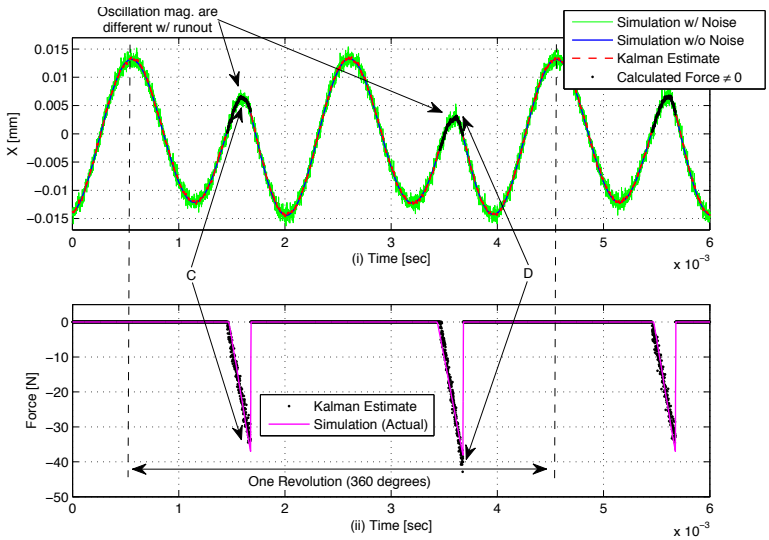

Fig. 36. (i) Kalman filter state estimate of noisy simulated tool deflection data, *X*, with runout at *b* = 3 mm. Simulated data with and without noise are given. The points at which the calculated force is not zero (i.e. the points where the tool is engaged in the workpiece) are shown as black dots along the estimated *X* curve. (ii) Calculated force signal found from the noisy *X* and *Y* simulated data compared with the actual simulated force signal.

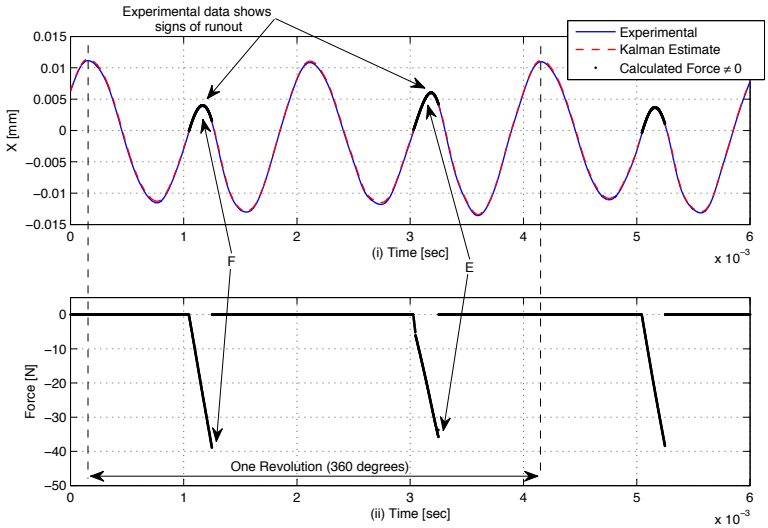

Fig. 37. (i) Kalman filter estimate of experimental deflection data, *X*, data at *b* = 3 mm. The points at which the calculated force is not zero (i.e. the points where the tool is engaged in the workpiece) are shown as black dots along the estimated *X* curve. (ii) Calculated force signal found from experimental *X* and *Y* data.

As shown analytically in Section 6.3, the magnitude of the force on tooth #1 and #2 are equal when runout does not exist, which results in equal oscillation magnitudes as each tooth is engaged in the workpiece (see points A and B in Fig. 35). However, when runout exists, unequal force magnitudes cause the oscillation magnitudes to change (see points C and D in Fig. 36). When generating the state estimate of *X*, the Kalman filter algorithm estimates the force given the deflection and angle of the tool. Therefore, the force signal from experimental data can now be compared with analytical results. The calculated force values for the experimental test are given in plot (ii) of Fig. 37. The estimated force generated by tooth #1 (see point E) is smaller than that generated from tooth #2 (see point F). Since tooth #2 has a larger applied force, the magnitude of *X* as the tooth #2 passes through the workpiece (see point F in plot (i)) is smaller than the

magnitude of tooth #1 (see point E in plot (i)). These results derived from experimental data directly correlate to the analytical results given above and in Section 6.3.

7.2 DISCRETE EXTENDED KALMAN FILTER

The discrete EKF is an expansion of the basic discrete Kalman filter given in Section 7.1. Where the basic Kalman filter only estimates the states of a system, an EKF is able to estimate both the states and parameters within the model [33]. The EKF is "extended" because it applies to nonlinear systems. The desired parameters are added to the system as additional pseudo states, which cause the system to become nonlinear. Parameter estimation is useful when the parameters of a system change with time, or when the exact parameters are not known (as is the case in a milling operation). Experimental model parameters of m, c, and k can be estimated through the procedures given in Section 4.3; however, an EKF can generate estimates without separate experimental tests and can estimate the parameters on-line. The discrete EKF algorithm used in state/parameter estimation is presented in Section 7.2.1. EKF state and parameter estimates of simulated and experimental defection data are then given in Section 7.2.2.

7.2.1 DISCRETE EKF ALGORITHM

In Section 7.1, state estimates are obtained based on a discrete Kalman model of the system and a measurement of the state, X. This estimate assumes that model parameters of the system (m, c, and k) are known. In order to estimate the model parameters, they must be added to the system as three additional pseudo states, where $m = x_3$, $c = x_4$, and $k = x_5$ [33]. Therefore, the respective discrete state and measurement equations given in Eqs. (19) and (20) can be expanded to

$$\boldsymbol{x}_k = f_{k-1}(\boldsymbol{x}_{k-1}, \boldsymbol{u}_{k-1}\boldsymbol{w}_{k-1}) = \begin{bmatrix} x_{2,k-1}T + x_{1,k-1} \\ \frac{T}{x_{3,k-1}}(-x_{2,k-1}x_{4,k-1} - x_{1,k-1}x_{5,k-1} + u_{x,k-1} + w_{x,k-1}) + x_{2,k-1} \\ w_{M,k-1}T + x_{3,k-1} \\ w_{C,k-1}T + x_{4,k-1} \\ w_{K,k-1}T + x_{5,k-1} \end{bmatrix}, \quad (30)$$

$$y_k = h_k(\boldsymbol{x}_k, \boldsymbol{v}_k) = \boldsymbol{H}_k\boldsymbol{x}_k + v_{x,k} = x_{1,k} + v_{x,k}, \quad (31)$$

where w_M, w_C, and w_K are artificial noise terms that are added to the system that allows the EKF filter to modify its estimates of x_3, x_4, and x_5, respectively. A flow diagram of the EKF estimation process is given in Fig. 33 of Section 7.1.1 (the Kalman and EKF flow diagrams are the same). The discrete Kalman filter equations are given by Simon [33] at each time step, $k = 1, 2, \ldots$, as follows

$$\hat{\boldsymbol{x}}_k^- = f_{k-1}(\hat{\boldsymbol{x}}_{k-1}^+, \boldsymbol{u}_{k-1}, 0), \quad (32)$$

$$\boldsymbol{P}_k^- = \boldsymbol{F}_{k-1}\boldsymbol{P}_k^+\boldsymbol{F}_{k-1}^T + \boldsymbol{L}_{k-1}\boldsymbol{Q}_{k-1}\boldsymbol{L}_{k-1}^T, \quad (33)$$

$$\boldsymbol{K}_k = \boldsymbol{P}_k^-\boldsymbol{H}_k^T(\boldsymbol{H}_k\boldsymbol{P}_k^-\boldsymbol{H}_k^T + \boldsymbol{M}_k\boldsymbol{R}_k\boldsymbol{M}_k^T)^{-1}, \quad (34)$$

$$\hat{\boldsymbol{x}}_k^+ = \hat{\boldsymbol{x}}_k^- + \boldsymbol{K}_k(\boldsymbol{y}_k - \boldsymbol{H}_k\hat{\boldsymbol{x}}_k^-), \quad (35)$$

$$\boldsymbol{P}_k^+ = (\boldsymbol{I} - \boldsymbol{K}_k\boldsymbol{H}_k)\boldsymbol{P}_k^-, \quad (36)$$

where the partial derivative matrixes $\boldsymbol{F}$, $\boldsymbol{L}$, $\boldsymbol{H}$, and $\boldsymbol{M}$ are given as

$$\boldsymbol{F}_{k-1} = \left.\frac{\partial f_{k-1}}{\partial \boldsymbol{x}}\right|_{\hat{\boldsymbol{x}}_{k-1}^+} = \begin{bmatrix} 1 & T & 0 & 0 & 0 \\ -\frac{\hat{x}_{5,k-1}^+}{\hat{x}_{3,k-1}^+}T & 1 - \frac{\hat{x}_{4,k-1}^+}{\hat{x}_{3,k-1}^+}T & F_{3,3} & -\frac{\hat{x}_{1,k-1}^+}{\hat{x}_{3,k-1}^+}T & -\frac{\hat{x}_{2,k-1}^+}{\hat{x}_{3,k-1}^+}T \\ 0 & 0 & 1 & 0 & 0 \\ 0 & 0 & 0 & 1 & 0 \\ 0 & 0 & 0 & 0 & 1 \end{bmatrix}, \quad (37)$$

$$F_{3,3} = \frac{T}{(\hat{x}^+_{3,k-1})^2}(\hat{x}^+_{2,k-1}\hat{x}^+_{4,k-1} + \hat{x}^+_{1,k-1}\hat{x}^+_{5,k-1} - u_{x,k-1} - w_{k-1})$$

$$\boldsymbol{L}_{k-1} = \left.\frac{\partial f_{k-1}}{\partial \boldsymbol{w}}\right|_{\hat{\boldsymbol{x}}^+_{k-1}} = \begin{bmatrix} 0 & 0 & 0 & 0 \\ \dfrac{T}{\hat{x}^+_{3,k-1}} & 0 & 0 & 0 \\ 0 & T & 0 & 0 \\ 0 & 0 & T & 0 \\ 0 & 0 & 0 & T \end{bmatrix}, \tag{38}$$

$$\boldsymbol{H}_k = \left.\frac{\partial h_k}{\partial \boldsymbol{x}}\right|_{\hat{\boldsymbol{x}}^-_k} = \begin{bmatrix} 1 & 0 & 0 & 0 & 0 \end{bmatrix}, \tag{39}$$

$$\boldsymbol{M}_k = \left.\frac{\partial h_k}{\partial \boldsymbol{v}}\right|_{\hat{\boldsymbol{x}}^-_k} = [1]. \tag{40}$$

Referring to Eq. (30), the process noise vector, $\boldsymbol{w}$, contains 4 variables (i.e. $\boldsymbol{w} = [w_x, w_M, w_C, w_K]$) and the measurement noise vector, $\boldsymbol{v}$, contains one variable (i.e. $\boldsymbol{v} = [v_x]$). As discussed in Section 7.1.1, the dimension of the covariance terms $\boldsymbol{Q}$ and $\boldsymbol{R}$ are $i \times i$ and $j \times j$, respectively, where i is the length of $\boldsymbol{w}$ and j is the length of $\boldsymbol{v}$. Therefore, $\boldsymbol{Q}$ is 4×4 and $\boldsymbol{R}$ is 1×1.

The discrete EKF algorithm is shown in block diagram form in Fig. 34 of Section 7.1.2. The EKF and Kalman filter block diagrams are almost identical to one another. The difference being that once the force in the x-direction is calculated using the traditional chip thickness model, the discrete EKF uses Eqs. (30) – (40) in estimating both the x-directional states and model parameters. The process noise, w_x, measurement noise, v_x, and artificial noise terms, w_M, w_C, and w_K, are all taken as zero in Eqs. (30) and (31) (it is assumed the only noise in the system is contained in the measurement of X). Initial guesses of $\hat{\boldsymbol{x}}^+_1$ and $\boldsymbol{P}^+_1$ are once again defined at the start of the EKF algorithm and

used within the first time step (i.e. when $k = 1$). At each time step an updated estimate vector, $\hat{\boldsymbol{x}}_1^+$, is calculated (this vector contains estimates for the states/pseudo states x_1, x_1, …, x_5).

7.2.2 PARAMETER ESTIMATION WITH DISCRETE EKF

To show the accuracy of the EKF state/parameter estimates, two sets or simulated deflection data (one with and one without runout) and one set of experimental deflection data are tested. Once again, a normally distributed random noise signal with a mean of zero and a variance of 0.5×10^{-3} mm is added to the simulated $\boldsymbol{X}$ and $\boldsymbol{Y}$ data vectors before the state/parameter estimation is performed. Initial state estimates are set to zero, and initial model parameter estimates are randomly chosen within ±50% of their nominal values (respective nominal values are m = 0.040 kg, c = 9.2 N-s/m, and $k = 11.5\times10^5$ N/m). These initial state and parameters values comprise the vector $\hat{\boldsymbol{x}}_1^+$. The initial guess of the covariance matrix, $\boldsymbol{P}_1^+$, is given below.

$$\boldsymbol{P}_1^+ = \begin{bmatrix} 10^{12} & 0 & 0 & 0 & 0 \\ 0 & 10^{12} & 0 & 0 & 0 \\ 0 & 0 & 10^{8} & 0 & 0 \\ 0 & 0 & 0 & 5\times10^{13} & 0 \\ 0 & 0 & 0 & 0 & 10^{22} \end{bmatrix} \tag{41}$$

The diagonal terms of $\boldsymbol{P}_1^+$ are chosen based on the convergence rate required for each state/pseudo state. Finally, the covariance terms, $\boldsymbol{Q}$ and $\boldsymbol{R}$, that provide the most accurate estimates of the states and model parameters from both experimental and simulated deflection data are given below.

$$\boldsymbol{Q} = \begin{bmatrix} 10^{14} & 0 & 0 & 0 \\ 0 & 0.1 & 0 & 0 \\ 0 & 0 & 0.1 & 0 \\ 0 & 0 & 0 & 0.1 \end{bmatrix} \qquad (42)$$

$$\boldsymbol{R} = [5]$$

Plot (i) of Figs. 38 and 39 shows the extended Kalman estimate of the state, x_1, for noisy simulated deflection data at b = 3 mm for the case without and with runout, respectively. The state estimates are shown to match the actual simulated X data (i.e. X without noise) very well for both cases. Plot (ii) of each figure gives the EKF force estimate found using the traditional chip thickness model along with the actual force signal from the simulation. The noisy X and Y data causes slight variations in the estimated force signals from the EKF; however, the general trend of the estimated force signal does follow that of the simulated force. Plot (iii) of Figs. 38 and 39 shows the percent error of the model parameter estimates (i.e. m, c, and k) from their nominal values over the length of the $\boldsymbol{X}$ and $\boldsymbol{Y}$ input vectors (0.2 seconds).

For the case without runout (see plot (iii) of Fig. 38), the estimates for the mass, m, and stiffness, k, reach steady state (SS) errors of -3.5% within 0.1 seconds. The error in the damping, c, reaches its SS error value of 2% within 0.14 seconds. For the case with runout (see plot (iii) of Fig. 39), the estimates of m and k once again reach a SS values of -3.5% within 0.1 seconds. The estimate of c does not reach a SS value due to noise caused by the runout in the system (this noise is shown as oscillations in the estimate of c). The estimate of c does, however, converge to an average value of 5% within 0.14 seconds. From the results given here, the estimate of c is influenced the most by runout (i.e. runout increases the error in and adds noise to the estimate of c). It should

be noted that eliminating the noise signal on the simulated deflection data reduces the convergence times of the parameter estimates and slightly reduces the SS error.

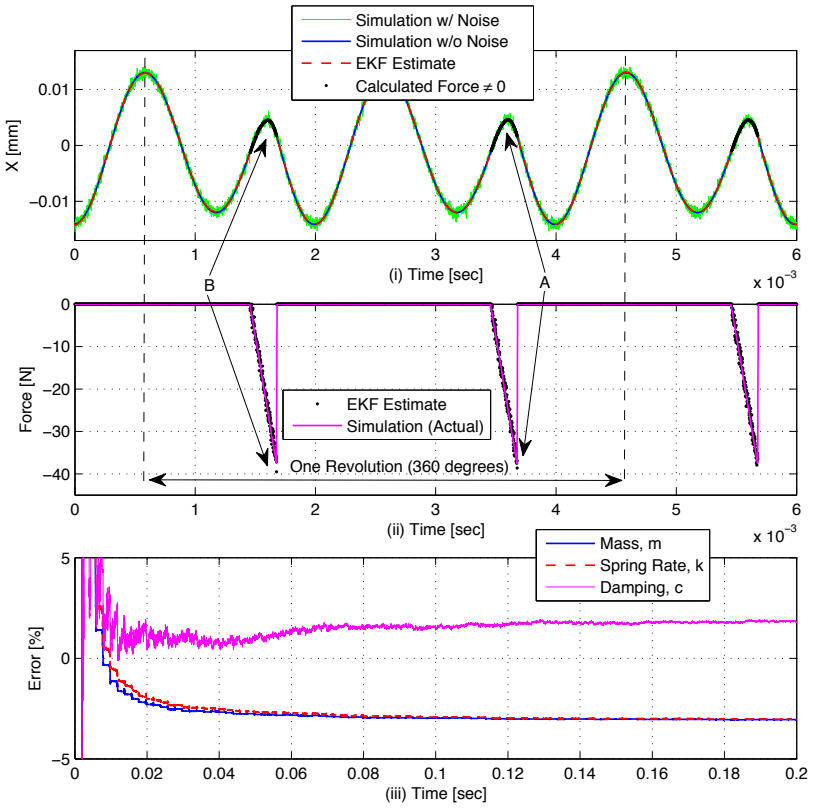

Fig. 38. (i) EKF state estimate of noisy simulated tool deflection data, *X*, without runout at *b* = 3 mm. Simulated data with and without noise are given. The points at which the calculated force is not zero are shown as black dots along the estimated *X* curve. (ii) Calculated force signal from the EKF algorithm found from noisy *X* and *Y* simulated data compared with the actual simulated force signal. (iii) Model parameter estimate errors of *m*, *c*, and *k* from their nominal values over the length of the simulated data (0.2 seconds).

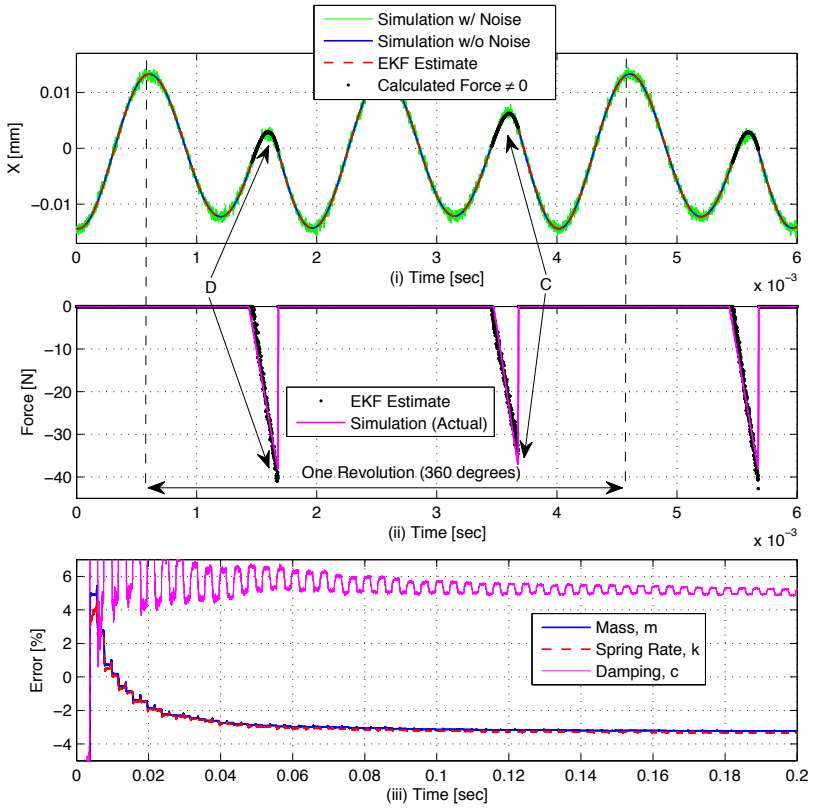

Fig. 39. (i) EKF state estimate of noisy simulated tool deflection data, *X*, with runout at *b* = 3 mm. Simulated data with and without noise are given. The points at which the calculated force is not zero are shown as black dots along the estimated *X* curve. (ii) Calculated force signal from the EKF algorithm found from noisy *X* and *Y* simulated data compared with the actual simulated force signal. (iii) Model parameter estimate errors of *m*, *c*, and *k* from their nominal values over the length of the simulated data (0.2 seconds).

The plots in Fig. 40 show the state and parameter estimates for experimental deflection data. The state estimate of *X* (see plot (i)) is able to track the experimental deflection data very well. The parameter estimates (see plot (iii)) of *m* and *k* reach respective SS errors of -6% and -6.5% within 0.1 seconds. Similar to the simulated result with runout (see plot (iii) of Fig. 39), the estimate of *c* for experimental deflection data contains error due to the runout in the system. Therefore, the estimate of *c* does not reach a SS value equal to the experimentally determined damping but instead converges to an

average value of 5.7% in 0.16 seconds. Plot (ii) of Fig. 40 gives the force estimates from the EKF algorithm generated from the experimental deflection data. Once again, the analytical and experimental force and deflection magnitudes as tooth #1 and #2 pass through the workpiece (see points A – F in Figs. 38 – 40) correspond to the runout results given in Section 6.3.

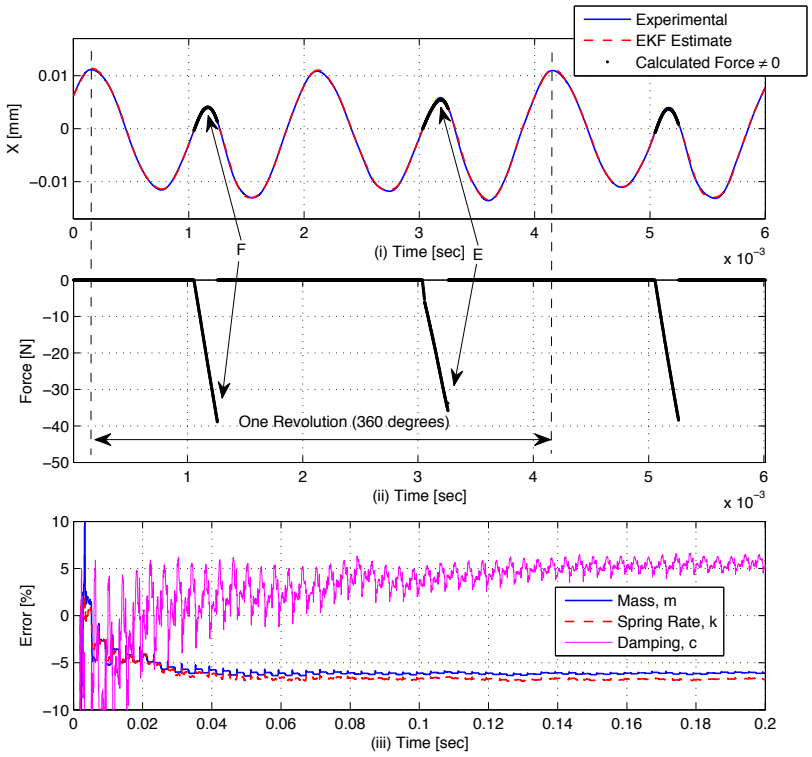

Fig. 40. (i) EKF state estimate of experimental tool deflection data, *X*, at *b* = 3 mm. The points at which the calculated force is not zero are shown as black dots along the estimated *X* curve. (ii) Calculated force signal from the EKF algorithm found from experimental *X* and *Y* data. (iii) Model parameter estimate errors of *m*, *c*, and *k* from their nominal values over the length of the simulated data (0.2 seconds).

7.3 OBSERVABILITY OF THE KALMAN FILTERS

Observability is a characteristic of the state space model of a dynamic system and the measurements. In the case of Kalman filter estimation, the filter is observable (i.e. there is guaranteed convergence of the state/parameter estimates) only if there are sufficient number of independent equations from which the estimates can be found [38]. The observability matrix, $\boldsymbol{O}$, of a time-invariant Kalman filter is given as

$$\boldsymbol{O} = \begin{bmatrix} \boldsymbol{H} \\ \boldsymbol{HF} \\ \boldsymbol{HF}^2 \\ \vdots \\ \boldsymbol{HF}^{n-1} \end{bmatrix} \tag{43}$$

where $\boldsymbol{F}$ is a partial derivative matrix representing the states of the system, $\boldsymbol{H}$ is a partial derivative matrix representing measurements of the system, and n is the number of estimated state/parameters contained in $\boldsymbol{F}$ [50]. A Kalman filter is observable if the number of independent equations in $\boldsymbol{O}$ is equal to the number of estimated states/parameters in $\boldsymbol{F}$ (i.e. the rank of $\boldsymbol{O}$ and $\boldsymbol{F}$ must be equal).

Matrices $\boldsymbol{F}$ and $\boldsymbol{H}$ for the time-invariant Kalman filter algorithm given in Section 7.1.1 are given in Eqs. (26) and (28), respectively. The observability matrix, $\boldsymbol{O}$, and state matrix, $\boldsymbol{F}$, of the discrete Kalman filter both have a rank of 2. Therefore, there are a sufficient number of independent equations in $\boldsymbol{O}$ to guarantee the convergence of the state estimates (i.e. the estimates of the deflection and velocity of the milling tool in the x-direction). Matrices $\boldsymbol{F}$ and $\boldsymbol{H}$ for the time-invariant EKF algorithm given in Section 7.2.1 are given in Eqs. (37) and (39), respectively. The rank of $\boldsymbol{O}$ for the EKF is 3, whereas the rank of $\boldsymbol{F}$ is 5 (i.e. there are 5 state/parameter estimates). As a result, there are only enough independent equations in $\boldsymbol{O}$ to guarantee convergence of 2 states (i.e. the

deflection and velocity of the tool) and 1 parameter (i.e. m, c, or k). However, 2 states and 3 parameters are estimated using this EKF algorithm.

If only the damping parameter, c, is estimated via the EKF (i.e. the mass, m, and stiffness, k, are assumed to be known), then the state and measurement equations of the filter are given as

$$\boldsymbol{x}_k = f_{k-1}(\boldsymbol{x}_{k-1}, \boldsymbol{u}_{k-1}\boldsymbol{w}_{k-1}) = \begin{bmatrix} x_{2,k-1}T + x_{1,k-1} \\ \frac{T}{m}(-x_{2,k-1}x_{3,k-1} - x_{1,k-1}k + u_{x,k-1} + w_{x,k-1}) + x_{2,k-1} \\ w_{C,k-1}T + x_{3,k-1} \end{bmatrix}, \tag{44}$$

$$y_k = h_k(\boldsymbol{x}_k, \boldsymbol{v}_k) = \boldsymbol{H}_k\boldsymbol{x}_k + v_{x,k} = x_{1,k} + v_{x,k}, \tag{45}$$

and the partial derivative matrices $\boldsymbol{F}$ and $\boldsymbol{H}$ given as

$$\boldsymbol{F}_{k-1} = \left.\frac{\partial f_{k-1}}{\partial \boldsymbol{x}}\right|_{\hat{\boldsymbol{x}}_{k-1}^{+}} = \begin{bmatrix} 1 & T & 0 \\ -\frac{k}{m}T & 1-\frac{x_{3,k-1}}{m}T & -\frac{x_{2,k-1}}{m}T \\ 0 & 0 & 1 \end{bmatrix}, \tag{46}$$

$$\boldsymbol{H}_k = \left.\frac{\partial h_k}{\partial \boldsymbol{x}}\right|_{\hat{\boldsymbol{x}}_k^{-}} = \begin{bmatrix} 1 & 0 & 0 \end{bmatrix}. \tag{47}$$

The rank of $\boldsymbol{O}$ computed form Eqs. (46) and (47) and the rank of $\boldsymbol{F}$ in Eq. (46) are both 3. This verifies that 2 states and 1 parameter can be estimated via the EKF with guaranteed convergence. Similar procedures show that parameters m and k can also be estimated individually with guaranteed convergence.

It is assumed that estimating one single parameter (the remaining parameters are assumed to be known exactly) will provide an estimate with less steady state (SS) error than when all 3 parameters are estimated simultaneously. To show this, model parameters estimates are found using the EKF algorithm given in Section 7.2.1 (all 3

parameters are estimated at once) and EKF's that estimate each parameter separately. Estimates are found for the simulated deflection data without runout given in plot (i) of Fig. 38 (b = 3 mm and Ω = 15,000 rpm). No noise is added to the simulated deflection data prior to estimation to eliminate any sources of error in the estimates. Nominal model parameter values are m = 0.0353 kg, c = 9.6982 N-s/m, and $k = 9.9150\times10^5$ N/m. When a given parameter is estimated individually, the remaining 2 parameters are constants and are equal to their respective nominal values.

Plots (i – iii) in Fig. 41 give the respective parameter estimates of m, c, are k for the case when the parameters are estimated simultaneously and independently. The percent error in the estimate results in Fig. 41 are given in Table 4. When parameters m and k are estimated alone, the SS errors in the estimates are smaller than when all 3 parameters are estimated together. On the other hand, the error in the estimate of c is less when all parameters are estimated at the same time (the exact reason for this is not clear). Even though the parameter estimates are not guaranteed to converge onto an exact solution when the EKF algorithm given in Section 7.2.1 is used, all states/parameters in the system are detectable in that all poles of $\boldsymbol{F}$ in Eq. (37) are contained within the unit circle [50]. Furthermore, from the results given in Fig. 41, all estimates converge to values within 3.04% of their respective nominal values when this EKF algorithm is used. When convergence is guaranteed (i.e. when each parameter is estimated separately), all estimates converge to values within 2.64% of their respective nominal values, which is only 0.4% better than when all parameters are estimated at once. Furthermore, estimating only one parameter is not practical in real applications since exact values of the remaining parameters are not often known. Therefore, estimating m, c, and k using the

EKF algorithm in Section 7.2.1 is considered the preferred parameter estimation procedure.

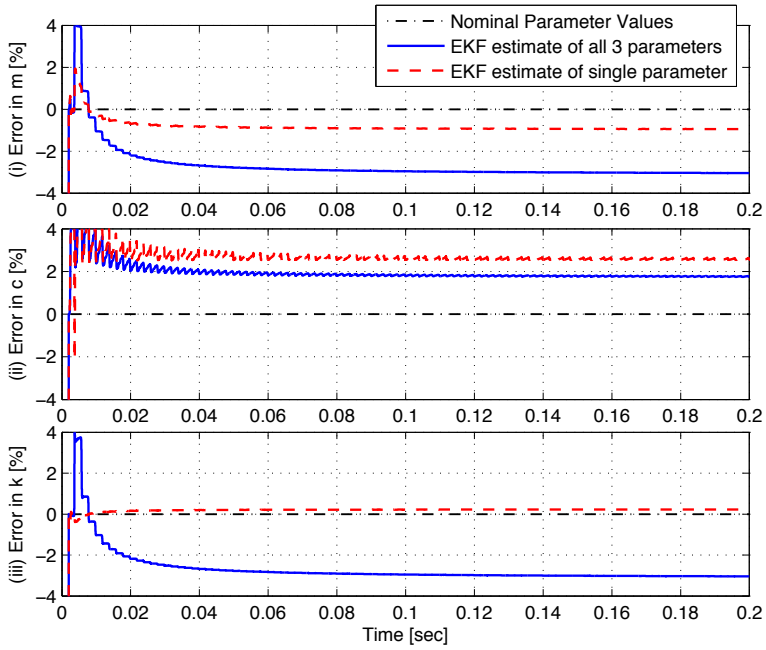

Fig. 41. Parameter estimate error from their nominal values for simulated deflection data at b = 3mm and Ω = 15,000 rpm. Parameters are estimated simultaneously and individually: (i) estimates of m, (ii) estimates of c, (ii) estimates of k.

Table 4. Parameter estimate results from Fig. 41.

	EKF estimate error from nominal [%]	
	All 3 Parameters	**Single Parameter**
Mass, *m*	-3.04	-0.95
Damping, *c*	1.77	2.64
Stiffness, *k*	-3.04	0.19

7.4 RESULTS AND CONCLUSIONS

In this chapter, discrete Kalman filter and discrete EKF algorithms are developed using the traditional milling model given in Section 3.1. Both algorithms are able to accurately estimate the milling states in the x-direction (specifically the tool

displacement, X) given simulated and experimental deflection data. Through EKF parameter estimates of simulated data, runout in the system is shown to affect the estimate of c much more than the estimates of m or k. Runout adds noise to the estimate of c and also increases the estimate error by 3% over the case with no runout. Runout is also shown to exist in the experimental deflection data; therefore, the effect of runout on the parameter estimates (especially the estimate of c) must be considered when experimental data is tested.

The EKF algorithm given here is able to estimate all model parameters (i.e. estimate m, c, and k) within 6.5% of their nominal values for experimental deflection data and within 5% of their nominal values for simulated deflection data. This percent error is considered acceptable given the benefits that EKF parameter estimation provides. Unlike the techniques given in Section 4.3, where both static and dynamic tests are used in finding model estimates, parameter estimation with the EKF algorithm is fast, easily repeatable, can be performed on-line, and is not influenced by human error. The EKF algorithm can also be used to periodically update estimates of m, c, and k to account for changes in a milling operation due to nonlinearities in the system, un-modeled dynamics, and/or tool wear. The EKF algorithm given here is used in Section 9.2 as part of a control system capable of predicting and preventing the onset of chatter in a simulated milling process. It is also used in Section 11.2.1 to provide on-line parameter estimates during an actual milling operation.

The observabiltiy of the Kalman filters is also tested. The discrete Kalman filter is shown to be observable; however, the discrete EKF filter is not (i.e. convergence of state/parameter estimates is not guaranteed). Parameter estimates from the EKF

developed in Section 7.2.1, which is not observable since it estimates all model parameters at once, are compared with parameter estimates from observable EKF results (these filters only estimate one parameter at a time). When all parameters are estimated concurrently, the estimates do converge and have an error range only slightly larger than when each parameter is estimated individually. Furthermore, estimating only one parameter is not practical in real applications since exact values of the remaining parameters are not often known. Therefore, the EKF algorithm presented in Section 7.2.1 is considered the preferred parameter estimation procedure and will be solely used in the follow chapters.

Chapter 8 ADDITIONAL RESULTS

The diagrams in Fig. 42 show the three separate testing procedures used for increasing and decreasing b along the length of the workpiece, L. Test procedure (T.P.) #1 increases b by feeding the milling tool in the negative z-direction as the workpiece is moved past the tool in the positive x-direction (see Fig. 42 for axis directions). There is concern that the downward feed of the tool into the workpiece, which will cause material to be cut by the bottom surface of the tool, will increase the forces on the tool tip and affect tool dynamics. Furthermore, the milling model does not consider forces due to cutting at the bottom surface of the tool, so experimental results obtained using T.P. #1 and simulated results may show differences in tool dynamics and bifurcation points. Therefore, a second testing procedure is used (see T.P. #2 in Fig. 42) that increases b without feeding the tool down into the workpiece (i.e. without cutting material with the bottom surface of the tool). For T.P. #2, a lip is pre-cut into the workpiece, eliminating any movement of the tool in the z-direction during testing. The pre-cut lip has a thickness, h_n, larger than the radial immersion of the experimental tests, h. This eliminates any risk of the tool coming in contact with the back surface of the pre-cut lip as the tool undergoes large magnitude vibrations. Test procedure #3 decreases b by feeding the milling tool in the positive z-direction as the workpiece is fed past the tool in the positive x-direction (see Fig. 42 for axis directions). Since the tool feed in the z-direction is away from the workpiece in T.P. #3, no additional forces can be applied to the tool (i.e. the dynamics of the system are not affected). Therefore, no other testing procedure is required for decreasing b along the workpiece.

The experimental results given in Section 5.3 through the end of Chapter 7 use T.P. #1 and #3 of Fig. 42 for increasing and decreasing b, respectively. Furthermore, these previous experimental tests are only performed at a spindle speed, Ω, of 15,000 rpm. In this chapter, results are given for two separate experimental trials performed using T.P. #1, #2, and #3 (six tests total). These six tests are repeated at 15,000, 14,000, 10,000, and 9,500 rpm, for a total of 24 experimental tests. During testing, all efforts are placed on making the experimental setup and execution of each test identical. Furthermore, trials 1 and 2 for each test procedure are run in direct succession.

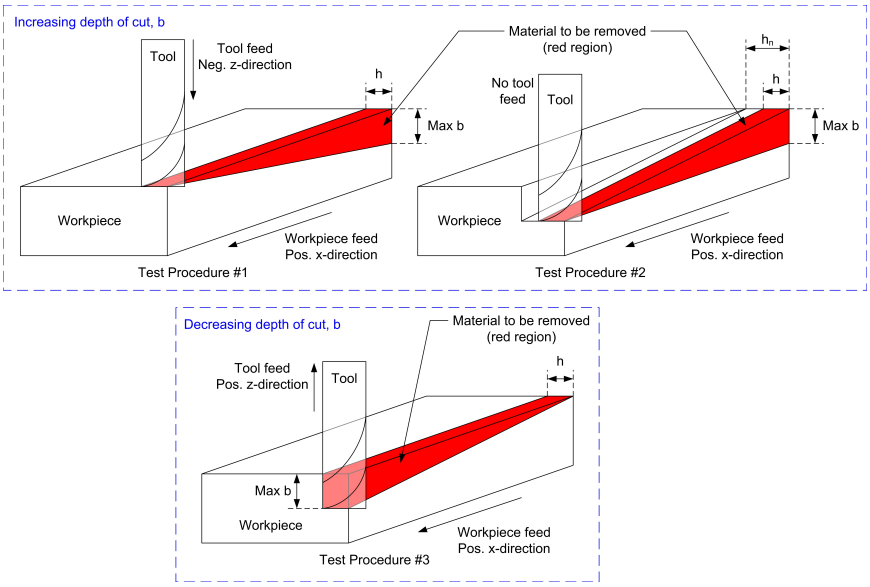

Fig. 42. Diagram of the testing procedures used for obtaining experimental results for an increasing and decreasing depth of cut, *b*.

Bifurcation diagrams for each experimental test are given in Section 8.1. Simulated results at each Ω are also given and compared to the experimental results. In Section 8.2, EKF parameter estimates of the experimental and simulated results are given at a constant depth of cut, b, of 3 mm (these results are similar to the EKF estimates given in Section 7.2.2). EKF model estimates for an increasing b are presented in Section 8.3

for two sets of experimental results at Ω = 15,000 rpm (these tests show parameter estimates change as the depth of cut is varied). The effect of runout on experimental and simulated tool deflection data is further investigated in Section 8.4 at spindle speeds of 15,000 and 10,000 rpm. Finally, results and conclusions are given in Section 8.5. All simulated and experimental results given in this chapter are for an up-milling process with h = 0.382 mm and f = 0.0635 mm/tooth. Model parameters (m, c, and k) for the simulated results are found by averaging EKF parameter estimates of the experimental data at each tested spindle speed, Ω (see Section 8.2 for parameter estimates of all 24 experimental tests). The new milling model is used in generating all simulated results.

8.1 EXPERIMENTAL/SIMULATED BIFURCATION RESULTS

The plots in Fig. 43 give the tool deflections in the x and y-directions, X and Y, and once-per-tooth-pass tool deflections, X_n and Y_n, for an experimental test using T.P. #1 in Fig. 42 (i.e. b is increased by feeding the tool in the negative z-direction). Referring to the X_n and Y_n data in Fig. 43, there is a bifurcation point (i.e. a transition from single stable chatter-free equilibrium points to multiple stable chatter equilibrium points) at b = 3.55 mm. The magnitude of X and Y (see green data in Fig. 43) increases significantly as the system crossed this bifurcation point. As b continues to increase, there is a second bifurcation point near b = 5.52 mm where the dynamics of the tool once again undergo a sudden change. At the second bifurcation point, there is an increase in the magnitude of X (see plot (i)) and a decrease in the magnitude of Y (see plot (ii)). The tool, therefore, begins to oscillate in a more elliptical pattern with the major axis in the x-direction increasing and the minor axis in the y-direction decreasing. Poincaré maps near b = 5.52 mm are shown to the right of the bifurcation diagrams in Fig. 43. The blue and red data

points in the Poincaré maps represent the respective once-per-tooth-pass deflection data at $b < 5.52$ mm (i.e. before the second bifurcation point) and $b > 5.52$ mm (i.e. after the second bifurcation point). There is an obvious change in the chatter equilibrium, which is represented by the location, size, and shape of the Poincaré maps, as b passes through 5.52 mm.

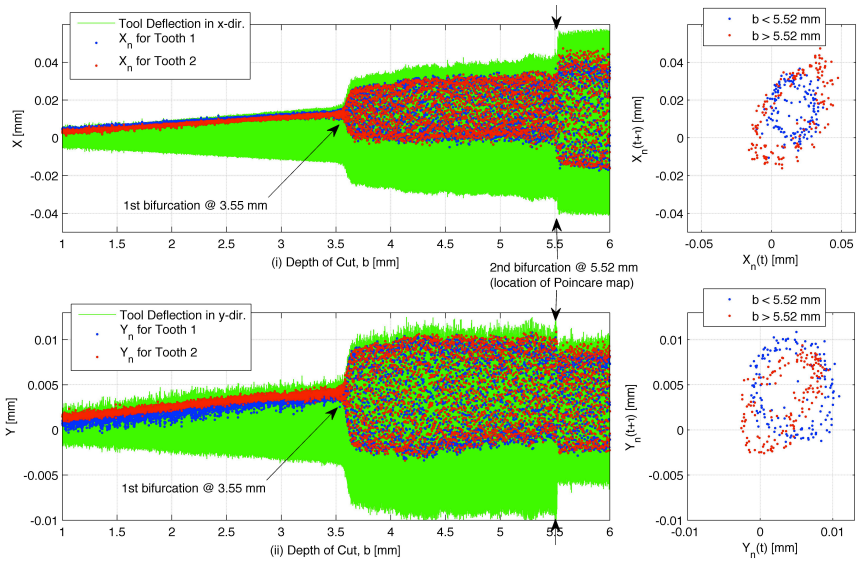

Fig. 43. Experimental tool deflection data, X and Y, and once-per-tooth-pass deflection data, X_n and Y_n, for an increasing b and Ω = 15,000 rpm (T.P. #1 in Fig. 42 is used): (i) displacement in the x-direction, (ii) displacement in the y-direction. Poincaré maps for X_n and Y_n near b = 5.52 mm are given to the right of each bifurcation diagram.

To further investigate the change in the tool dynamics near $b = 5.52$ mm, plots (i) and (ii) of Fig. 44 give X_n and Y_n, respectively, versus time at $b < 5.52$ mm (see blue data points) and $b > 5.52$ mm (see red data points). It is shown that the periods of $X_n(t)$ and $Y_n(t)$ decrease after the second bifurcation point (i.e. when $b > 5.52$ mm). To find the frequency of this data, the Matlab® command *spline*, which uses cubic spline interpolation, is used to interpolate the X_n and Y_n values over a smaller time step (see dashed lines in plots (i) and (ii) of Fig. 44 for interpolated data). A discrete Fourier

transform, using the Matlab® command *fft*, is then performed on the interpolated data to find the single-sided amplitude spectrum of $X_n(t)$ (see plot (iii) of Fig. 44) and $Y_n(t)$ (see plot (iv) of Fig. 44). The frequencies of $X_n(t)$ and $Y_n(t)$ are approximately 134 and 73 Hz for respective b values slightly less than and greater than 5.52 mm. Therefore, the frequency of $X_n(t)$ and $Y_n(t)$ is decreased by 46% as the system passes through the second bifurcation point.

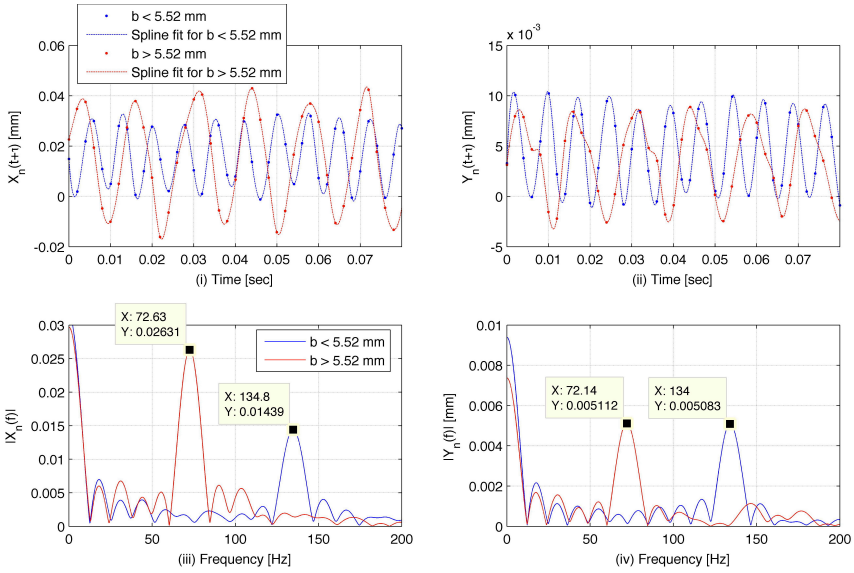

Fig. 44. (i, ii) Experimental once-per-tooth-pass displacement data, X_n and Y_n, before and after the second bifurcation in Fig. 43 at b = 5.52 mm. A spline fit for X_n and Y_n is also given. (iii, iv) Single-sided amplitude spectrum of $X_n(t)$ and $Y_n(t)$.

The experimental data given above (see Figs. 43 and 44) is obtained using T.P. #1 in Fig. 42 (i.e. b is increased by feeding the tool in the negative z-direction). The bifurcation diagrams for all four experimental tests for an increasing b at Ω = 15,000 rpm (i.e. two trials with T.P. #1 and two trials with T.P. #2) are shown in Fig. 45. Poincaré maps at b = 5.25 mm are given to the right of each bifurcation diagram. For trials 1 and 2 of T.P. #1 (see plots (i) and (ii) of Fig. 45), bifurcations occur at 3.55 and 4.4 mm,

respectively. These bifurcation points occur at significantly different depths of cut. Furthermore, trial 2 (see plot (ii)) does not have multiple bifurcation points, as does trial 1 (see plot (i)). This suggests that there is some uncertainty in the tool dynamics when b is increased along the length of the workpiece.

The bifurcation points for trials 1 and 2 of T.P. #2 (see plots (iii) and (iv) of Fig. 45) occur at b values of 4.56 and 5.35 mm, respectively. Once again, there is a significant difference in the bifurcation points for these two trials caused by uncertainty in the tool dynamics for an increasing depth of cut, b. The bifurcation points found using T.P. #2 occur at larger b values than those found using T.P. #1. Therefore, feeding the tool down into the workpiece (i.e. using T.P. #1), which may result in higher forces on the tool tip, decreases the chatter-free range of the system at Ω = 15,000 rpm.

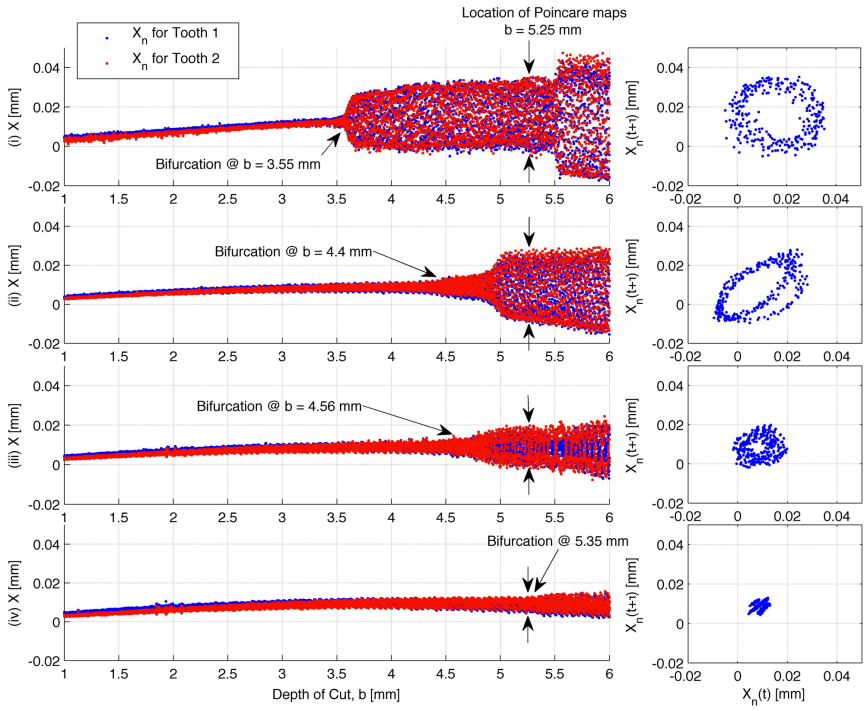

Fig. 45. Experimental once-per-tooth-pass tool displacement in the x-direction, X_n, for an increasing b and Ω = 15,000 rpm: (i) T.P. #1 - trial 1, (ii) T.P. #1 - trial 2, (iii) T.P. #2 - trial 1, (iv) T.P. #2 - trial 2. Poincaré maps at b = 5.25 mm are given to the right of each bifurcation diagram.

The bifurcation diagrams for trials 1 and 2 of T.P. #3 (i.e. decreasing b) at Ω = 15,000 rpm are shown in Fig. 46. Poincaré maps at b = 5.25 mm are given to the right of each bifurcation diagram. The bifurcation points for trials 1 and 2 occur at b values of 3.38 and 3.42 mm, respectively. For trails 1 and 2, the tool dynamics differ at b values slightly larger than their respective bifurcation points. Specifically, there is a gradual transition from chatter to chatter-free equilibrium points for trial 1 (see plot (i) of Fig. 46); however, there is a sudden jump from chatter to chatter-free equilibrium points for trial 2 (see plot (ii) of Fig. 46). Although the tool dynamics differ for each trial, the points at which the system becomes chatter-free (i.e. the bifurcation points) occur at very similar depths of cut. This is unlike the results for an increasing b (see Fig. 45) where bifurcations occur at significantly different b values. Therefore, there seems to be less uncertainty in the experimental bifurcation points when b is decreased along the length of the workpiece as apposed to increased.

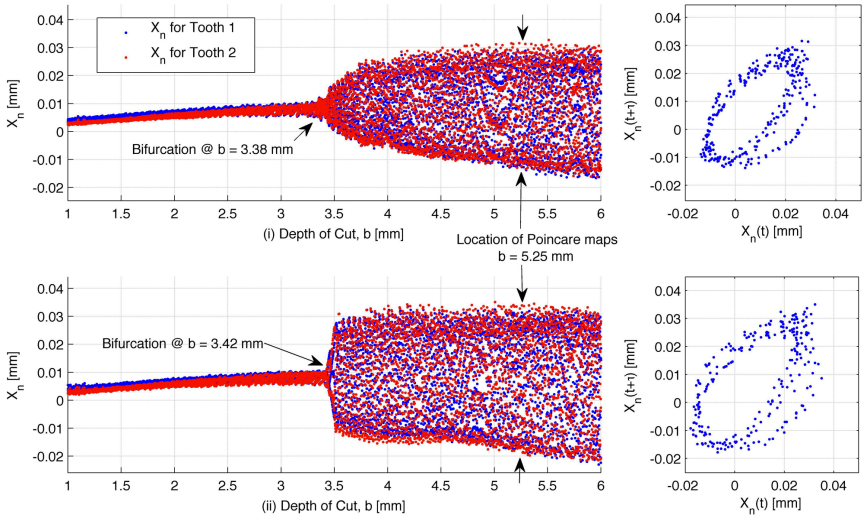

Fig. 46. Experimental once-per-tooth-pass tool displacement in the x-direction, X_n, for a decreasing b and Ω = 15,000 rpm: (i) T.P. #3 - trial 1, (ii) T.P. #3 - trial 2. Poincaré maps at b = 5.25 mm are given to the right of each bifurcation diagram.

The plots in Fig. 47 show simulated results from the new milling model for an increasing and decreasing b at Ω = 15,000 rpm. For an increasing b (see plot (i)), the simulated X_n data bifurcates at b = 3.99 mm, which is within the bifurcation range of the experimental results given in Fig. 45. For a decreasing b (see plot (ii)), the simulation bifurcates at b = 3.28 mm, which is slightly less than the experimental bifurcation points given in Fig. 46. The model parameters (m, c, and k) used in generating these simulated results are obtained through averaging EKF parameter estimates of all 6 experimental results given in Figs. 45 and 46 at b = 3 mm (the EKF parameter estimates of the experimental results are discussed in Section 8.2). Therefore, it is not expected for the bifurcation points of the simulated results to perfectly match any of the experimental results given above.

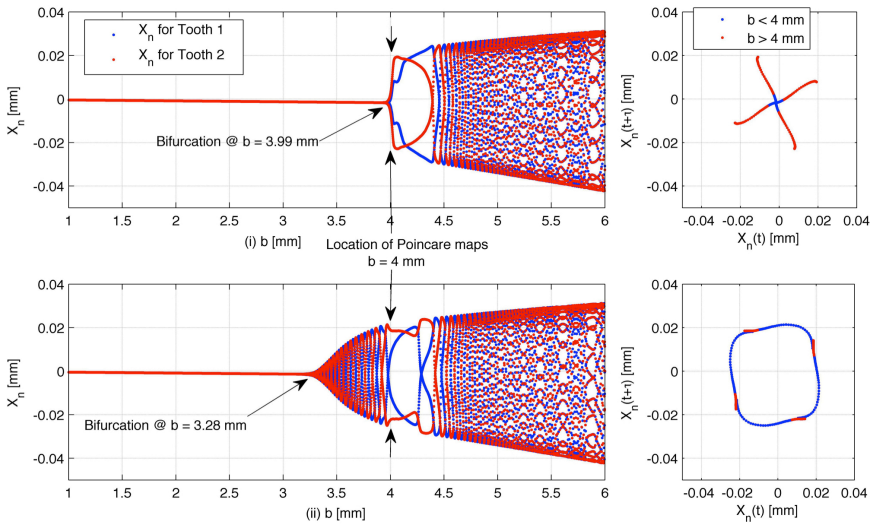

Fig. 47. Simulated once-per-tooth-pass tool displacement in the x-direction, X_n, with Ω = 15,000 rpm: (i) increasing b (ii) decreasing b. Poincaré map at b = 4 mm are given to the right of the bifurcation diagrams. Model parameters used are the average EKF parameter estimates of the experimental results in Figs. 45 and 46 at b = 3 mm (m = 0.0353 kg, c = 9.6982 N-s/m, k = 9.9250×10^5 N/m).

Poincaré maps at b = 4 mm are given to the right of each simulated bifurcation diagram in Fig. 47. Referring to the Poincaré map for an increasing b (see plot (i)), the system contains stable chatter-free equilibrium points for $b < 4$ mm (see blue data) and stable chatter equilibrium points for $b > 4$ mm (see red data). After the system bifurcates (i.e. when $b > 4$ mm), there exists 4 distinct stable chatter equilibrium points at b values slightly greater than 4 mm. As shown by the X_n data in plot (i), these 4 distinct equilibrium points exist for b values ranging from 4 to approximately 4.4 mm. At $b \approx 4.4$ mm, the 4 distinct stable chatter equilibrium points multiply into significantly more chatter equilibrium points. Referring to the bifurcation diagram for a decreasing b (see plot (ii)), there once again exists 4 distinct stable chatter equilibrium points for b ranging from 4 to approximately 4.4 mm. The Poincaré map in plot (ii) of Fig. 47 shows a significant number of stable chatter equilibrium points for $b < 4$ mm (see blue data) and 4 distinct stable chatter equilibrium points for $b > 4$ mm (see red data). When a significant number of chatter equilibrium points exist over a small range of b, the Poincaré map has a continuous circular shape as shown in by the blue data in plot (ii).

Six identical experimental tests to those given above at Ω = 15,000 rpm (i.e. two trials from T.P. #1, #2, and #3) are performed at spindle speeds of 14,000, 10,000, and 9,500 rpm. The bifurcation diagrams for these experimental tests along with simulated results are given in Appendix 1 (see Figs. 77 – 85). The bifurcation points for experimental and simulated results at each spindle speed are given in Table 5. As shown in Table 5, the average experimental bifurcation points for T.P. #1 at 15,000, 14,000, 10,000, and 9,500 rpm are 3.98, 3.65, 3.72, and 2.88 mm, respectively, while the average bifurcation points for T.P. #2 at the respective Ω values are 4.96, 4.08, 4.83, and 3.31

mm. At each Ω, T.P. #1 bifurcates at a lower b value than T.P. #2. Therefore, when increasing b, the forces added to the system by feeding the tool down into the workpiece (i.e. using T.P. #1) decrease the range over which the system is chatter-free. The average experimental bifurcation points for T.P. #3 (i.e. decreasing b) are 3.4, 3.1, 4.34, and 2.95 mm for the respective Ω values given above.

Milling dynamics has a subcritical bifurcation (i.e. contains hysteresis) [46]. Therefore, the bifurcation point when b is increased along the workpiece should occur at a large depth of cut than when b is decreased (this assumes the maximum and minimum values of b are the same for each case). The average experimental bifurcation points for T.P. #3 (i.e. decreasing b) do occur at smaller b values than T.P. #2 (i.e. increasing b without downward tool feed) at each tested spindle speed. This experimentally verifies the existence of hysteresis over a range of Ω. On the other hand, not all average bifurcation points for T.P. #3 are smaller than those from T.P. #1 (i.e. increasing b with downward tool feed), specifically the bifurcation points at 10,000 and 9,500 rpm. This is assumed to be a result of the forces added to the system by the downward feed of the tool into the workpiece. These additional forces change the dynamics of the tool, and in some cases cause the system to chatter at smaller depths of cut than when b is decreased across the length of the workpiece (i.e. when T.P. #3 is used). Therefore, when defining the average hysteresis range of the system at each tested spindle speed; only T.P. #2 and T.P. #3 should be considered. Therefore, the average experimental hysteresis region (i.e. the region where both stable chatter-free and chatter equilibrium exist) for the respective spindle speeds of 15,000, 14,000, 10,000, and 9,500 rpm are 3.4 – 4.96 mm, 3.1 – 4.08 mm, 4.43 – 4.83 mm, and 2.95 – 3.31 mm.

Table 5. Bifurcation points for experimental and simulated results at spindle speeds of 15,000, 14,000, 10,000, and 9,500 rpm (trails 1 and 2 from T.P. #1, #2, and #3 are represented here for each spindle speed).

Ω [rpm]	Case	Trial	Bifurcation Point [mm]	Average Bifurcation Point [mm]
15,000 (Exp.)	T.P. #1	1	3.55	3.98
		2	4.4	
	T.P. #2	1	4.56	4.96
		2	5.35	
	T.P. #3	1	3.38	3.4
		2	3.42	
15,000 (Sim.)	Increasing *b*	--	3.99	--
	Decreasing *b*	--	3.28	
14,000 (Exp.)	T.P. #1	1	3.5	3.65
		2	3.8	
	T.P. #2	1	3.7	4.08
		2	4.45	
	T.P. #3	1	3.0	3.1
		2	3.2	
14,000 (Sim.)	Increasing *b*	--	3.94	--
	Decreasing *b*	--	3.26	
10,000 (Exp.)	T.P. #1	1	4.0	3.72
		2	3.43	
	T.P. #2	1	4.94	4.83
		2	4.72	
	T.P. #3	1	4.44	4.43
		2	4.23	
10,000 (Sim.)	Increasing *b*	--	5.21	--
	Decreasing *b*	--	4.45	
9,500 (Exp.)	T.P. #1	1	1.97	2.88
		2	3.79	
	T.P. #2	1	3.52	3.31
		2	3.09	
	T.P. #3	1	2.2	2.95
		2	3.69	
9,500 (Sim.)	Increasing *b*	--	3.23	--
	Decreasing *b*	--	2.56	

8.2 EKF PARAMETER ESTIMATES OF EXPERIMENTAL RESULTS

The EKF algorithm given in Section 7.2 is used in finding parameters estimates of m, c, and k for each experimental test given in Section 8.1 (24 tests total). Deflection vectors, $\boldsymbol{X}$ and $\boldsymbol{Y}$, containing 0.2 seconds of data are inputted into the EKF algorithm at a

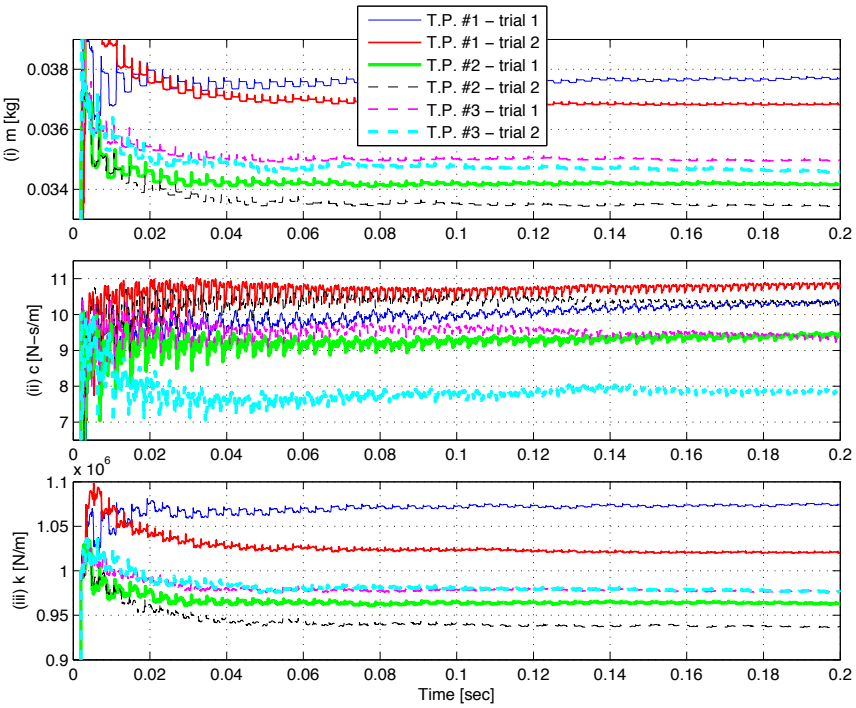

Fig. 48. Parameter estimates of *m*, *c*, and *k* from experimental deflection data at Ω = 15,000 rpm. Parameter estimates are given for two experimental trials from T.P. #1, #2, and #3 in Fig. 42 (6 tests total).

depth of cut near 3 mm. The covariance terms, $\boldsymbol{Q}$ and $\boldsymbol{R}$, used here are the same as the ones given in Section 7.2 (see Eq. (42)). The parameter estimates for experimental tests at spindle speeds of 15,000, 14,000, 10,000, and 9,500 rpm are given in Table 6. The average estimates of *m*, *c*, and *k* at each tested Ω are also given. Plots (i – iii) in Fig. 48 gives the respective EKF estimates of *m*, *c*, and *k* for each of the 6 experimental tests at Ω = 15,000 rpm (two trials from T.P. #1, #2, and #3) over the length of the inputted deflection vectors (0.2 seconds). For each test, the parameter estimates all reach SS/average values in approximately 0.1 seconds. As first shown in Section 7.2.2, runout in the experimental deflection data causes noise in the estimates of *c* (see plot (ii) of Fig. 48). At Ω = 15,000 rpm, the average estimates of *m*, *c*, and *k* have respective values of 0.0353 kg, 9.6982 N-s/m, and 9.9150×10^5 N/m. Plots of the EKF parameter estimates for

the 6 tests at spindle speeds of 14,000, 10,000, and 9,500 rpm are given in Appendix 2 (see Figs. 86 – 88).

Table 6. EKF parameter estimates at spindle speeds of 15,000, 14,000, 10,000, and 9,500 rpm (trails 1 and 2 from T.P. #1, #2, and #3 are represented here for each spindle speed). Parameter estimates are obtained from experimental deflection data, X and Y, at b = 3 mm.

			EKF Parameter Estimates			
Ω [rpm]	**Test Procedure**	**Trial**	**m [kg]**	**c [N-s/m]**	**k [N/m]**	
15,000 (Exp.)	**#1**	**1**	0.0377	10.3388	10.7458×10^5	
		2	0.0368	10.8273	10.2068×10^5	
	#2	**1**	0.0342	9.4346	9.6329×10^5	
		2	0.0334	10.3342	9.3674×10^5	
	#3	**1**	0.0350	9.3705	9.7710×10^5	
		2	0.0346	7.8836	9.7660×10^5	
			0.0353	**9.6982**	**9.9150×10^5**	**Mean**
14,000 (Exp.)	**#1**	**1**	0.0298	9.0241	8.6833×10^5	
		2	0.0293	9.3821	8.4863×10^5	
	#2	**1**	0.0279	9.6322	8.0263×10^5	
		2	0.0279	9.6395	7.9632×10^5	
	#3	**1**	0.0287	9.6050	8.2396×10^5	
		2	0.0286	9.3087	8.2042×10^5	
			0.0287	**9.4319**	**8.2671×10^5**	**Mean**
10,000 (Exp.)	**#1**	**1**	0.0362	7.0023	10.0846×10^5	
		2	0.0358	7.2284	10.0333×10^5	
	#2	**1**	0.0356	8.0845	9.6646×10^5	
		2	0.0351	7.8357	9.6094×10^5	
	#3	**1**	0.0437	8.2501	12.0262×10^5	
		2	0.0425	7.9913	11.8216×10^5	
			0.0382	**7.732**	**10.5400×10^5**	**Mean**
9,500 (Exp.)	**#1**	**1**	0.0336	8.7166	9.9691×10^5	
		2	0.0309	7.9474	8.8897×10^5	
	#2	**1**	0.0322	5.7962	9.2258×10^5	
		2	0.0316	7.5422	8.9093×10^5	
	#3	**1**	0.0311	7.8862	9.0047×10^5	
		2	0.0301	8.1975	8.6230×10^5	
			0.0316	**7.6810**	**9.1036×10^5**	**Mean**

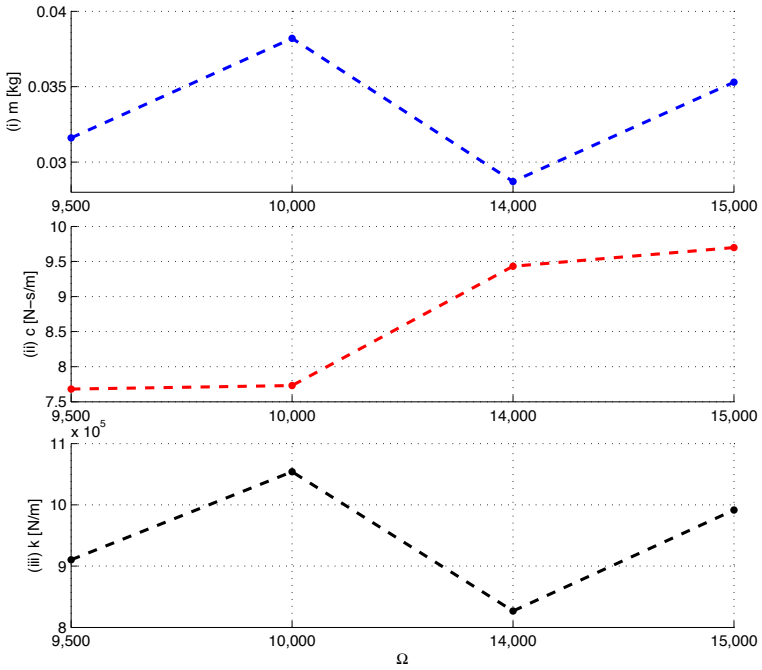

Fig. 49. Average parameter estimates of *m* (i), *c* (ii), and *k* (iii) from experimental deflection data over a range of spindle speeds.

Plots (i – iii) in Fig. 49 give the average parameter estimates for *m, c*, and *k*, respectively, over the range of tested Ω values. From this figure, the parameter estimates are shown to change depending on the spindle speed. Noise in the measurement data and tool wear can cause slight variations in model parameter estimates from test-to-test. However, these changes are mainly caused by the inability of the linear model, which is used within the EKF algorithm, to produce parameter estimates that represent the nonlinear system over a large range of spindle speeds. The traditional milling model is used in defining the EKF; therefore, a circular tooth path and orthogonal cutting (i.e. the helix angle of zero) are assumed. When all other parameters in the milling model are left constant (specifically the cutting coefficients, K_n and K_t, and b), the model parameter estimates are shown to change as Ω changes in order for the linear model to adapt to the nonlinear system. As shown in Fig. 49, a single set of model parameter estimates cannot

be used to accurately represent a milling operation over a range of spindle speeds. Therefore, EKF parameter estimates must be updated (especially when Ω changes) to produce m, c, and k values that best characterize the system at the current spindle speed.

8.3 EKF ESTIMATES ALONG AN INCREASING DEPTH OF CUT

In Section 8.2, it is shown that EKF model parameter estimates change over a range spindle speeds. Knowledge of how/if parameter estimates change as b is varied along the length of the workpiece, L, is also desired. To show this, estimates are taken at 1-second intervals for the experimental deflection data from trial 1 of T.P. #1 and T.P. #2 at Ω = 15,000 rpm. At a 1-second interval, Ω = 15,000 rpm, f = 0.127 mm/rev, and L = 986 mm, approximately 30 estimates are performed for each experimental result. The experimental deflection of the tool in the x-direction, X, and once-per-tooth-pass deflection data, X_n, are given in plot (i) of Figs. 50 and 51 for trial 1 of T.P. #1 and #2, respectively. The EKF model estimates along the length of the each experimental test are given in plot (ii). The estimates are represented as percent variations from the model estimates found in Section 8.2 at b = 3 mm (the value of these "nominal" estimates are given in plot (ii) of Figs. 50 and 51).

For trial 1 of T.P. #1 (see plot (ii) of Fig. 50), the estimates near b = 3 mm match the nominal parameter values. This is expected since the nominal parameter values are calculated from the same experimental data at b = 3 mm (refer to Section 8.2). At depths of cut less than 3 mm, the estimates of m and k are less than their nominal values, and the estimates of c are greater than its nominal value. The error between the model estimates and their nominal values increase as b is decreased from 3 mm. For b < 2 mm, the estimates of c are at least 15% larger than the nominal value. The estimates of m and k

increase in an exponential manner for b values greater than 0.4 mm. For depths of cut ranging from 2.95 to 4.95 mm, all estimates stay within 2% of their nominal values. At the location of the first bifurcation point (b = 3.55 mm), there is a sight increase in the estimate of c. There is a more significant increase in the estimate of c (approximately a 10% jump) when the system experiences its second bifurcation at b = 5.52 mm. The bifurcation points do not cause notable changes in the estimates of m or k.

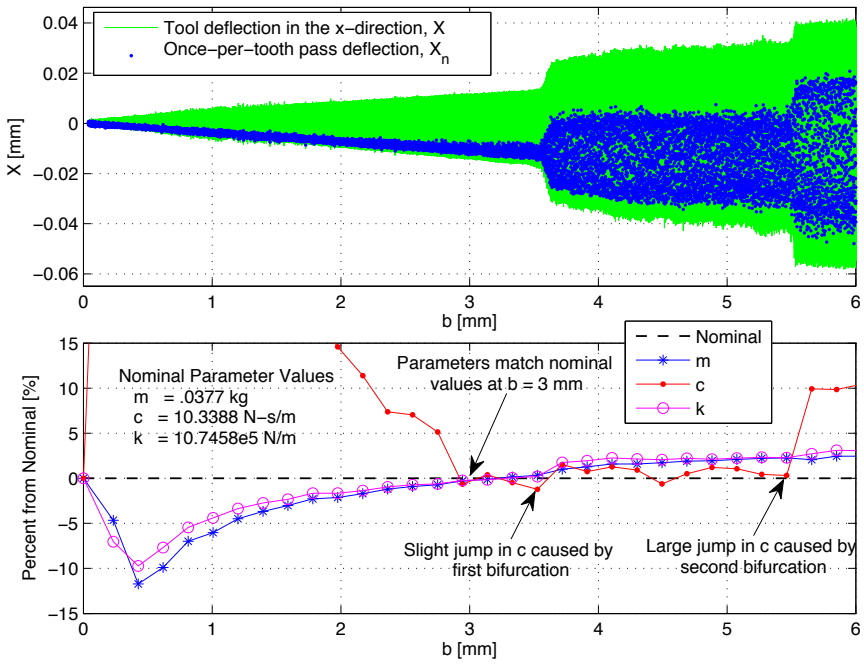

Fig. 50. (i) Experimental tool deflection in the *x*-direction, *X*, and once-per-tooth-pass deflection data, X_n, for an increasing *b* and Ω = 15,000 rpm (T.P. #1 – trial 1). (ii) EKF model parameter estimates of *m*, *c*, and *k* at 1-second intervals along the length of the experiment.

For trial 1 of T.P. #2 (see Fig. 51), the EKF estimates at b = 3 mm once again match the nominal parameter values found in Section 8.2. The estimates of m, c, and k follow similar trends to the results given above in Fig. 50. The estimates of m and k increase exponentially for $b > 0.25$ mm. For $b < 1.8$ mm, the estimates of c are at least 15% larger than the nominal value. All model parameter estimates stay within 2% of

their nominal values for depths of cut ranging from 2.95 to 4.6 mm. Once again, there is a slight jump in the estimate of c at the bifurcation point at b = 4.56 mm (the bifurcation does not affect the estimates of m or k). For b > 4.56 mm, the damping estimate, c, continues to slowly increase as the chatter vibrations become larger (i.e. as b continues to increase).

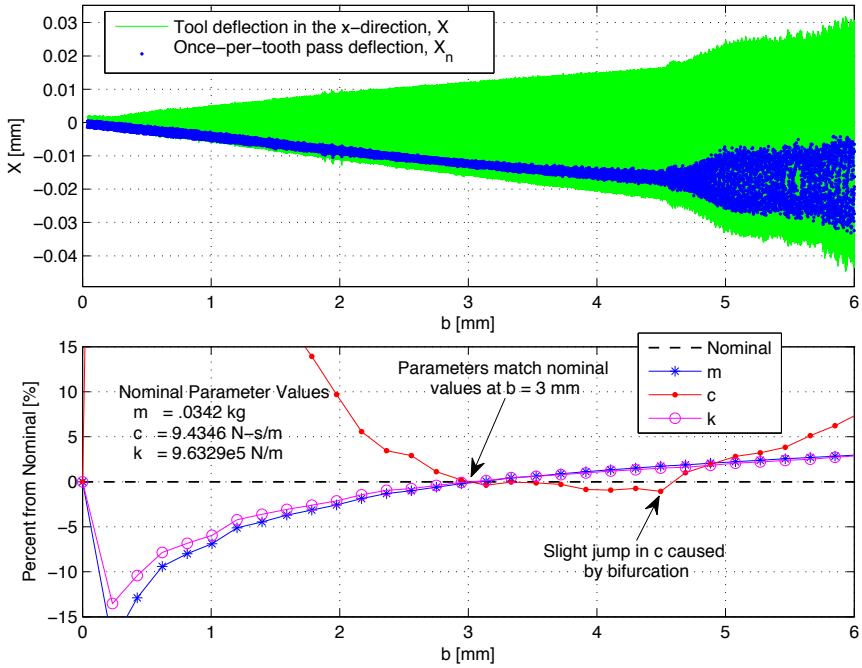

Fig. 51. (i) Experimental tool deflection in the *x*-direction, *X*, and once-per-tooth-pass deflection data, X_n, for an increasing *b* and Ω = 15,000 rpm (T.P. #2 – trial 1). (ii) EKF model parameter estimates of *m*, *c*, and *k* at 1-second intervals along the length of the experiment.

From the experimental results given here, it is shown that the model parameter estimates change depending on the depth of cut and stability state of the milling operation (i.e. whether or not chatter vibrations exist). The changes in the model estimates at different depths of cut can be contributed to the inability of the linear model used in the calculating the EKF estimates to represent the milling system over a range of b. At a constant Ω, the model parameters must change as b changes in order for the linear model

to adapt to the nonlinear system. Therefore, EKF parameter estimates must be updated as b changes to produce m, c, and k values that best represent the system at its current b value. It should be noted that any noise in the experimental deflection will be magnified when the deflection of the tool is small (i.e. when b is small), which will cause errors in the EKF estimates. This may be a reason for the large differences between the parameter estimates at small values of b (especially $b < 2$ mm) and their nominal values (see plot (ii) of Figs. 50 and 51).

8.4 RUNOUT IN SIMULATED AND EXPERIMENTAL RESULTS

As discussed in Chapter 6, runout causes changes in the tool deflection as a result of uneven force distribution on the two cutting teeth. The period of the x-directional deflection increases from every 1/2 revolution to every full revolution when runout exists. To simulate runout, the radii of tooth #1, r_1, and tooth #2, r_2, are offset a given percentage from their nominal values of 6.35 mm (r_1, and r_2 are decreased and increased from their nominal values, respectively). In the following sections, different degrees of runout are simulated and compared with experimental tool deflection data. Two separate spindle speeds are considered. Simulated and experimental results at spindle speeds of 15,000 and 14,000 rpm are given in Sections 8.4.1 and 8.4.2, respectively. The simulated results use model parameters obtained from the average experimental EKF estimates given in Table 6 (see Section 8.2) for the respective Ω values.

8.4.1 RESULTS FOR A SPINDLE SPEED OF 15,000 RPM

Simulated tool deflection data in the x-direction, X, is given in Fig. 52 at $b = 3$ mm for various degrees of runout (tooth radii offsets equal 0, 0.01, 0.015, and 0.02%).

At a spindle speed of 15,000 rpm, the tool oscillates 4 times per revolution. The tip of each oscillation is labeled A – D in Fig. 52. These points are magnified to show a more detailed representation of the effect runout has on the tool deflection. When no runout exists (i.e. when the tooth radii offset is 0), the oscillation magnitude at points A and B and at points C and D are the same. Simulating an increase in runout (i.e. increasing the tooth offset) causes a respective decrease and increase in the magnitude at points A and B. At points C and D, runout causes a slight increase in oscillation magnitude and a slight shift in phase.

As discussed in Section 8.1, the Matlab® command *spline* and *fft* can be used in generating the single-sided amplitude spectrum of $X(t)$. The plots in Fig. 53 give the amplitude spectrum of $X(t)$ for the simulated deflection data given in Fig. 52. There are 3 main magnitude peaks at frequencies near 500, 750, and 1000 Hz (the peak of each magnitude is magnified in Fig. 53 and labeled E – G, respectively). The rotation of the tool, *Rot*, in revolutions corresponding to each frequency, *freq*, is calculated using the following equation.

$$Rot = \frac{\Omega}{freq}\left(\frac{1}{60}\right) \tag{48}$$

From the equation above, magnitudes at 500, 750, and 1000 Hz correspond to 1/2, 1/3, and 1/4 revolutions of the tool, respectively. The dominant frequency magnitude of the tool motion is at 1000 Hz, which relates to 1/4 revolution of the tool. Referring to in Fig. 53, the magnitude at each frequency increases as runout increases. This is especially evident at 750 Hz (see point F), where the magnitude is zero when no runout exists and increases as the offset in the tooth radii increases (i.e. as runout increases). The magnitude at 750 Hz has a direct relationship to the difference in oscillation magnitudes

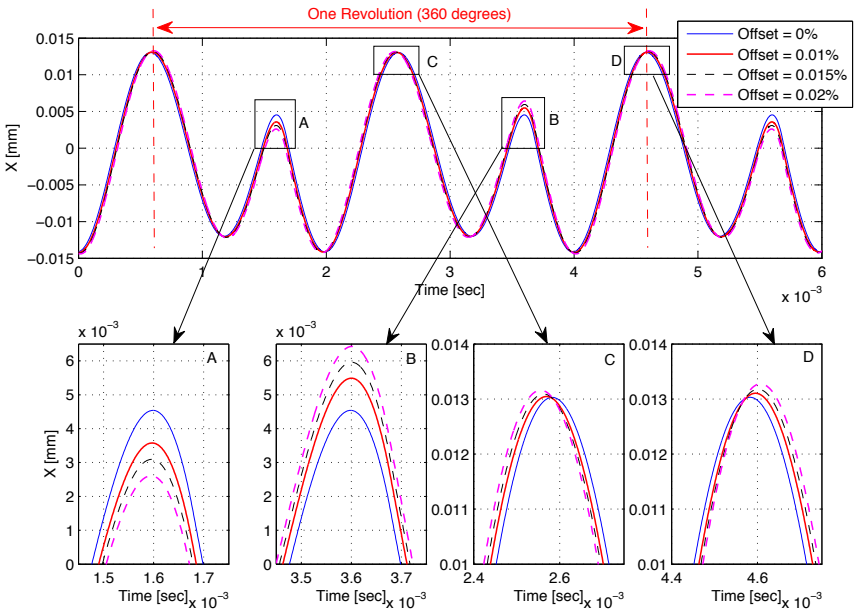

Fig. 52. Simulated tool deflection data in the *x*-direction, *X*, at b = 3 mm and Ω = 15,000 rpm for various degrees of runout (tooth radii offsets equal 0, 0.01, 0.015, and 0.02%). The peaks of selected oscillations are magnified and labeled A – D.

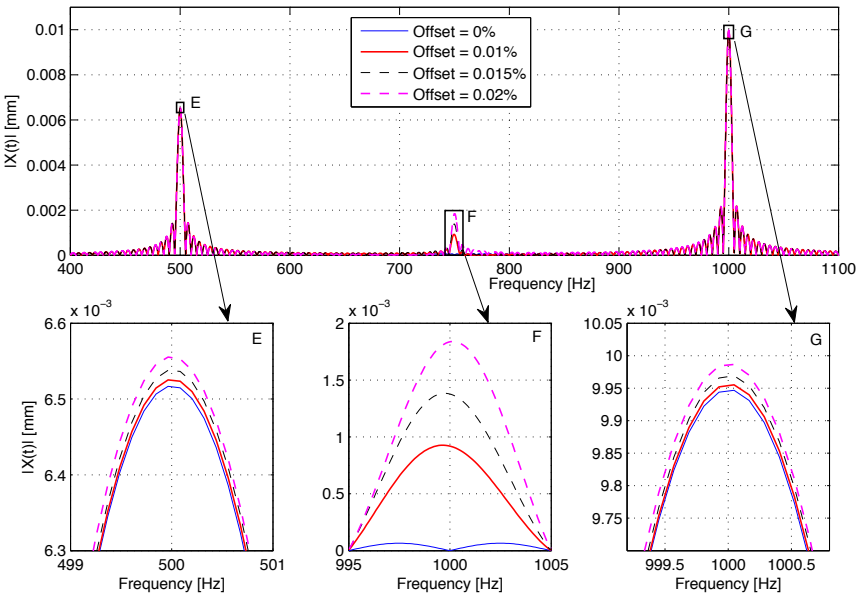

Fig. 53. Single-sided amplitude spectrum of the simulated $X(t)$ data given in Fig. 52. The peaks of frequency magnitudes near 500, 750, and 1000 Hz are magnified and labeled E – G, respectively.

at points A and B in Fig. 52. As discussed in Section 6.3, runout causes unequal forces on tooth #1 and #2, which results in a change in the magnitude of X at points A and B. The magnitude at 750 Hz can, therefore, be used as a reference to the amount of runout in the simulated milling process at Ω = 15,000 rpm.

Experimental tool deflection data in the x-direction, X, at b = 3 mm is given in Fig. 54 for 2 separate trials from T.P. #1, #2, and #3 in shown in Fig. 42 (6 tests total). Once again the tip of each oscillation is magnified and labeled A – D. The amplitude spectrum of $X(t)$ for each experimental result is given in Fig. 55 (the peak of the frequency magnitudes near 500, 750, and 1000 Hz are labeled E – G, respectively). By comparing points A and B and points C and D in Fig. 54, there are slight differences in the deflection magnitudes from test-to-test. This is expected when different testing procedures are used. For example, at a given depth of cut, the dynamics of the tool will inevitably be different when b is increased (i.e. when T.P. #1 or #2 is used) or decreased (i.e. when T.P. #3 is used) along the length of the workpiece. Furthermore, nonlinearities in the system such as slight changes in the workpiece material properties, workpiece surface finish, or changes in the model parameters will lead to slight differences in the deflection data between tests. Referring to point F in Fig. 55, the frequency magnitude at 750 Hz ranges from 0.7×10^{-3} to 1.6×10^{-3} mm for the 6 experimental tests. The exact amount of runout in the actual milling operation cannot be derived from this set of results. However, it can be concluded that runout is present in the experimental system for each test. The dynamics of the tool at Ω = 14,000 rpm are very similar to the results given here for Ω = 15,000 rpm. Therefore, experimental and simulated data at Ω = 14,000 rpm are not given for sake of brevity.

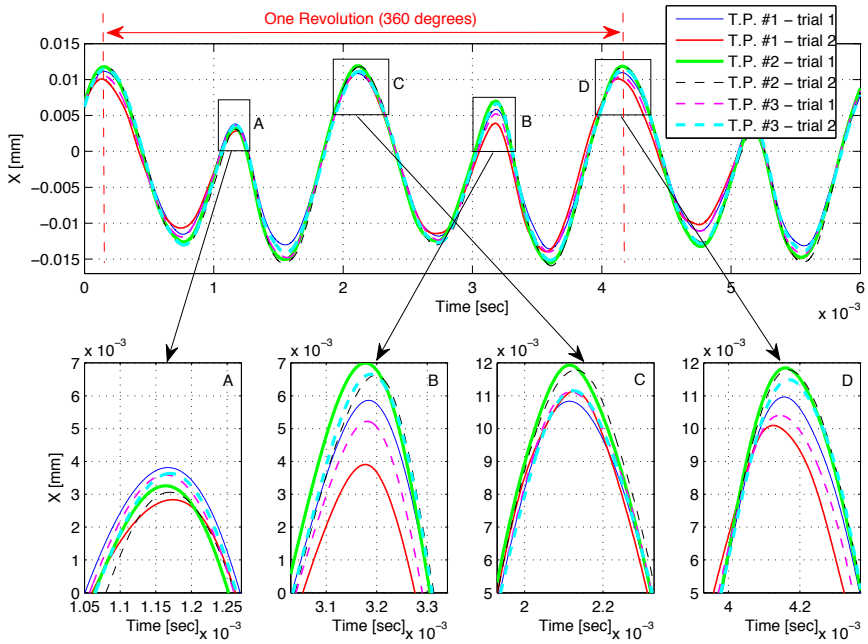

Fig. 54. Experimental tool deflection data in the *x*-direction, *X*, at *b* = 3 mm and *Ω* = 15,000 rpm for trials 1 and 2 of T.P. #1, #2, and #3 (6 results total). The peaks of selected oscillations are magnified are magnified and labeled A – D.

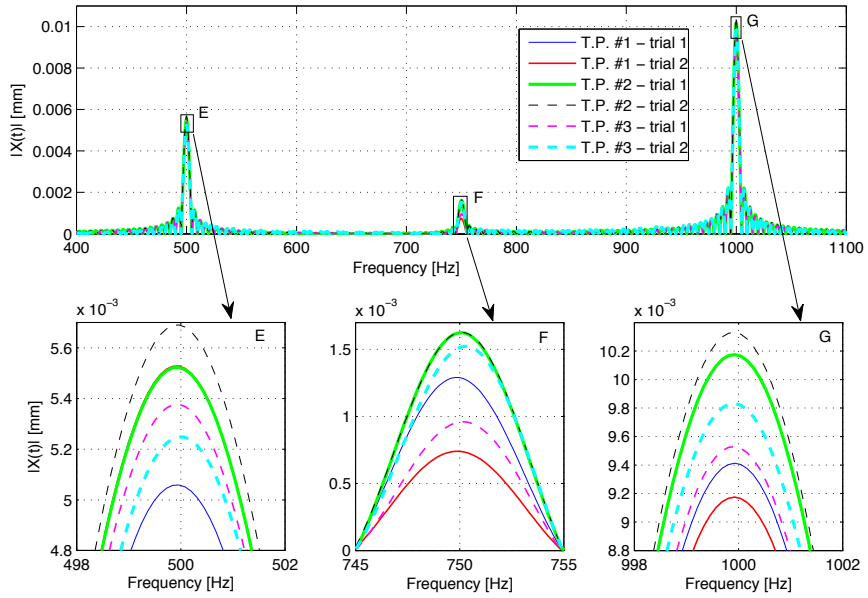

Fig. 55. Single-sided amplitude spectrum of the experimental *X*(*t*) data given in Fig. 54. The peaks of frequency magnitudes near 500, 750, and 1000 Hz are magnified and labeled E – G, respectively.

8.4.2 RESULTS FOR A SPINDLE SPEED OF 10,000 RPM

Simulated tool deflection data in the x-direction, X, is given in Fig. 56 at b = 3 mm for various degrees of runout (tooth radii offsets equal 0, 0.01, 0.015, and 0.02%). When Ω = 15,000 rpm, the tool oscillates 4 times per revolution (see Fig. 52). However, the tool oscillates 6 times per revolution when Ω = 10,000 rpm. Furthermore, the tool vibration magnitude is larger at 10,000 rpm than at 15,000 rpm. With all other parameters constant, decreasing the spindle speed, Ω, generally increases the tool vibration magnitude. For a simulated milling process without runout at b = 3 mm, the tool deflects in the x-direction over a range from -0.01413 to 0.01303 mm at Ω = 15,000 rpm and from -0.01629 to 0.01533 mm at Ω = 10,000 rpm. Referring back to Fig. 56, the tip of 4 of the 6 oscillations (labeled A – D) are magnified to show a detailed representation of the effects of runout at Ω = 10,000 rpm. The two oscillations that are not magnified behave similarly to points C and D. As in the 15,000 rpm case discussed in Section 8.4.1, the oscillation magnitude at points A and B and points C and D are the same when no runout exists (i.e. when the tooth radii offset is 0). Increasing runout causes a decrease and increase in the magnitudes at point A and B, respectively. Similarly, there is a respective magnitude increase and decrease at points C and D. There is also a slight phase shift at points A – D due to runout.

The amplitude spectrums of $X(t)$ are given in Fig. 57 for the simulated deflection data in Fig. 56. There are 4 main peak magnitudes at frequencies near 333, 666, 833, and 1000 Hz (there are only 3 frequency magnitudes for the 15,000 rpm case given in Fig. 53). The peak of each frequency magnitude in Fig. 57 is magnified and labeled E – H, respectively. From Eq. (48), frequencies at 333, 666, 833, and 1000 Hz represent 1/2,

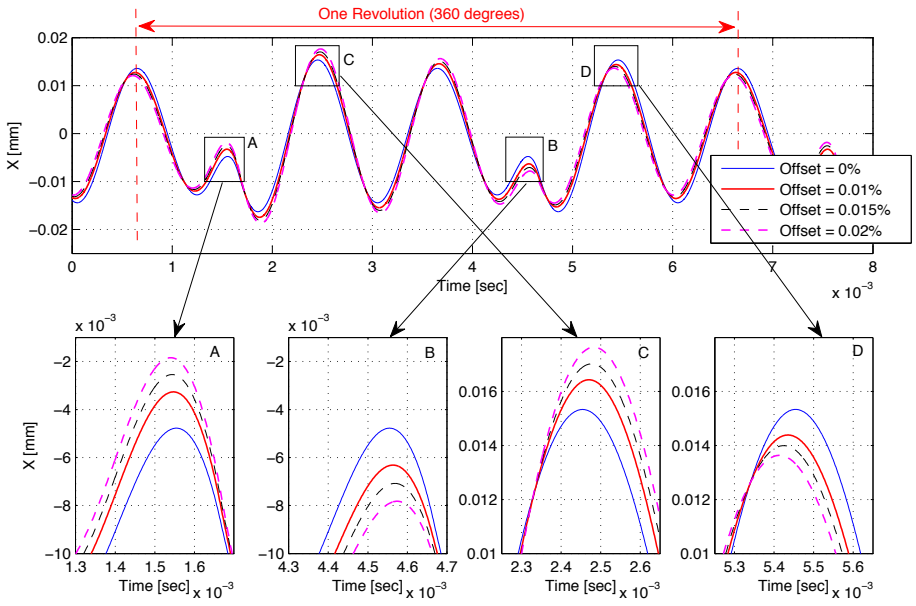

Fig. 56. Simulated tool deflection data in the *x*-direction, *X*, at *b* = 3 mm *Ω* = 10,000 rpm for various degrees of runout (tooth radii offsets equal 0, 0.01, 0.015, and 0.02%). The peaks of selected oscillations are magnified and labeled A – D.

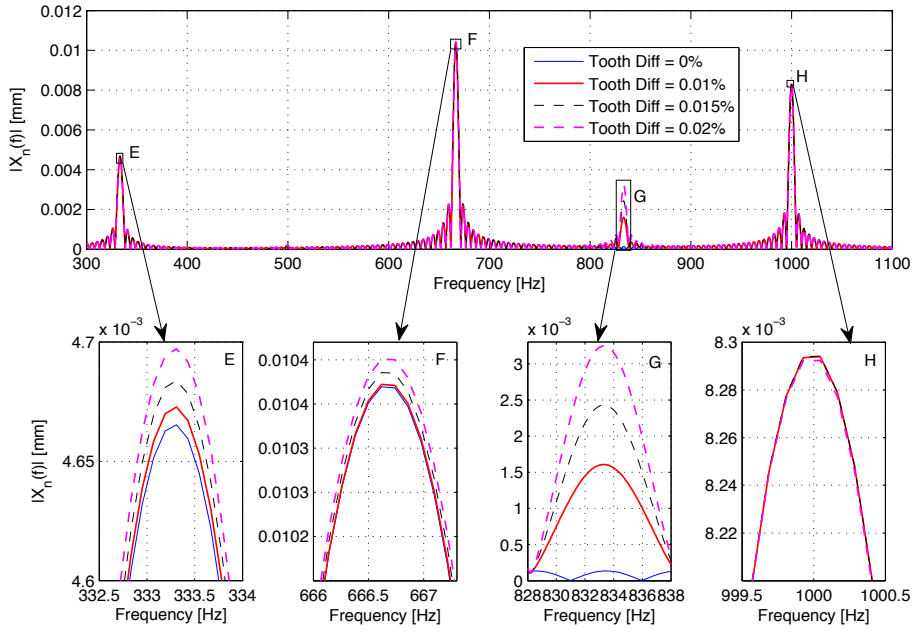

Fig. 57. Single-sided amplitude spectrum of the simulated *X*(*t*) data given in Fig. 56. The peaks of frequency magnitudes near 333, 666, 833, and 1000 Hz are magnified and labeled E – H, respectively.

1/4, 1/5, and 1/6 revolutions of the tool, respectively. The dominant frequency magnitude of the tool motion is at 666 Hz, which relates to 1/4 revolution of the tool. At Ω = 15,000 rpm, the dominant frequency (see plot Fig. 55) also corresponds to 1/4 revolution. Referring back to Fig. 57, the frequency magnitudes at 333, 666, 833 Hz (see points E – G, respectively) increase as runout increases (this is especially evident at 833 Hz). The magnitude at 1000 Hz (see point H) remains relatively constant as runout increases. The frequency magnitude at 1000 Hz corresponds to 1/6 revolution of the tool (there are 6 oscillations per revolution at Ω = 10,000 rpm). Referring to Fig. 56, runout causes a consistent increase and decrease in the oscillation magnitudes at points A and B and points C and D, respectively. As a result, the frequency magnitude for every ⅙ revolution of the tool (i.e. at 1000 Hz) is offset and therefore does not change as a result of runout. In other words, the changes in the frequency magnitudes at 333, 666 and 833 Hz offset any changes in the frequency magnitude at 1000 Hz. When no runout exists, the magnitude at 833 Hz (see point G in Fig. 57) is zero and increases as the offset in the tooth radii increase (i.e. as runout increases). The frequency magnitude at 833 Hz is directly related to the difference in the oscillation magnitudes of X at points A and B and points C and D in Fig. 52, which are a result of runout in the system. Therefore, the frequency magnitude at 833 Hz can be used as a reference to the amount of runout in the simulated milling process when Ω = 10,000 rpm.

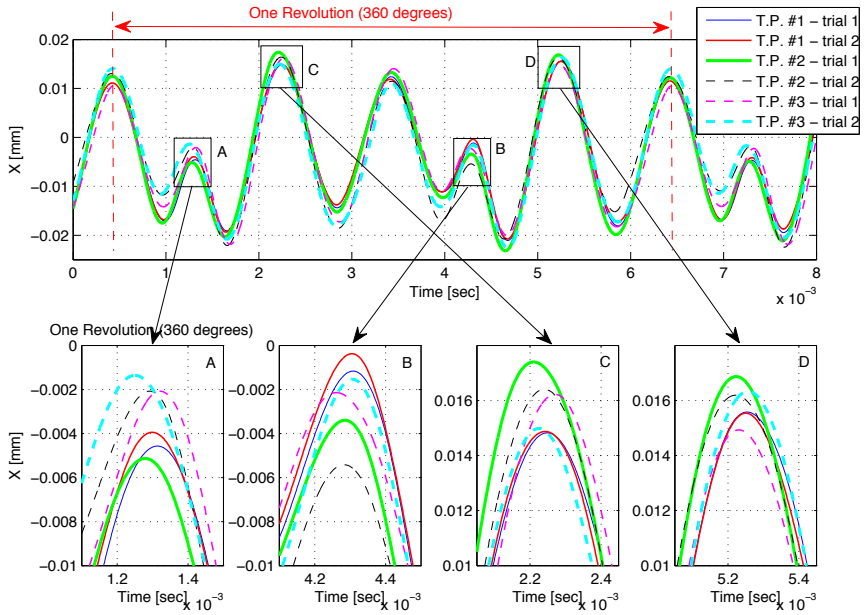

Fig. 58. Experimental tool deflection data in the *x*-direction, *X*, at *b* = 3 mm and *Ω* = 10,000 rpm for trials 1 and 2 of T.P. #1, #2, and #3 (6 results total). The peaks of selected oscillation are magnified and labeled A – D.

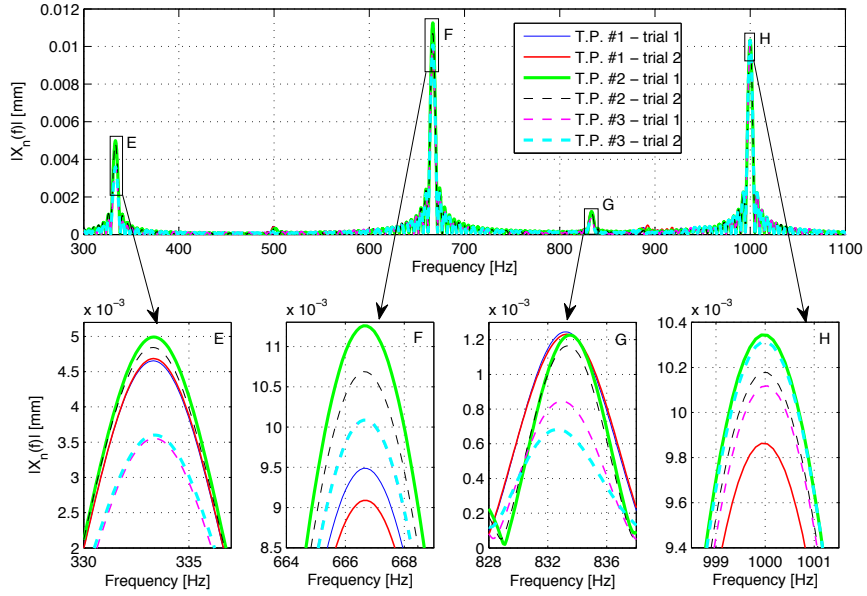

Fig. 59. Single-sided amplitude spectrum of the experimental *X*(*t*) data given in Fig. 58. The peaks of frequency magnitudes near 333, 666, 833, and 1000 Hz are magnified and labeled E – H, respectively.

The experimental tool deflection data in the x-direction, X, at b = 3 mm is given in Fig. 58 for 2 separate trials from T.P. #1, #2, and #3 in Fig. 42 (6 tests total). Once again the tip of 4 of the 6 tool oscillations are magnified and labeled A – D. The amplitude spectrum of $X(t)$ for each experimental result is given in Fig. 59. The peak of the frequency magnitudes near 333, 666, 833, and 1000 Hz are magnified and labeled E – H, respectively. Comparing points A and B and points C and D in Fig. 58, there are once again differences in the deflection magnitudes from test-to-test caused by the different testing procedures used and nonlinearities in the system. Referring to point G in Fig. 59, the frequency magnitude at 833 Hz ranges from 0.7×10^{-3} to 1.25×10^{-3} mm for the 6 experimental tests. Similar to the results at Ω = 15,000 rpm given in Section 8.4.1, the exact amount of runout cannot be derived from this set of experimental results. However, runout is present in all the experimental tests. The dynamics of the tool at Ω = 9,500 rpm are very similar to the results given above for Ω = 10,000 rpm. Therefore, experimental and simulated data at Ω = 9,500 rpm are not given for sake of brevity.

8.5 RESULTS AND CONCLUSIONS

In this chapter, six experimental tests (i.e. two experimental trials for T.P. #1, #2, and #3 in Fig. 42) are performed at spindle speeds of 15,000, 14,000, 10,000, and 9,500 rpm, for a total of 24 experimental results. When increasing b along the length of the workpiece, it is found that feeding the tool down into the workpiece material (i.e. using T.P. #1) decrease the range over which the system is chatter-free. It is assumed that the downward feed of the tool increases the forces on the tool, resulting in the formation of chatter vibrations at smaller depths of cut. Therefore, T.P. #2, which eliminates the downward feed of the tool, should be used when increasing b along the workpiece.

It is also found that EKF parameter estimates of experimental deflection data vary as the spindle speed and/or the depth of cut change. The model parameters change in order for the linear model to adapt to changes in the nonlinear system. Un-modeled dynamics of the system, whether they are linear or nonlinear, also contribute to changes in parameter estimates. Therefore, a single set of model parameter estimates cannot be used to accurately represent a milling operation over a range of Ω or b. For this reason, EKF parameter estimates must be updated to produce m, c, and k values that best represent the system at the current values of Ω and b. Finally, through further investigation of runout in simulated and experimental deflection data, it is found that frequency magnitudes at 750 and 833 Hz can be used as a reference to (or indication of) the amount of runout in the milling process at respective spindle speeds of 15,000 and 10,000 rpm. The exact amount of runout cannot be derived from the experimental results given here. However, it can be concluded that runout is present in the experimental milling system. Runout should, therefore, be considered in the analytical milling model to improve its ability to match the dynamics of an actual milling operation.

Chapter 9 STABILITY TRACKING

The stability analysis used in this research is based on the work of Weck [17] and Gather [18], where stability lobe diagrams are generated to indicate stable and unstable regions in the space defined by the depth of cut, b, and spindle speed, Ω. The process used in generating these stability diagrams is discussed in Section 9.1. A control system, which uses updated EKF parameter estimates to generate stability lobe diagrams, is designed and tested in Section 9.2. This control system varies the spindle speed and/or the feed rate of a simulated milling process to keep the current b versus Ω relation within the stable (i.e. chatter-free) region defined by the current stability bound of the system. An alternative method of tracking stability is presented in Section 9.3 that calculates the average root-mean-square of the once-per-tool-revolution tool deflection data. This method can determine the onset of chatter; however, it is unable to predict or prevent chatter vibrations entirely. Finally, a summary of the results are given in Section 9.4. All simulated and experimental results in this chapter are for an up-milling process with h = 0.382 mm and f = 0.0635 mm/tooth (the feed rate, f, is varied in some cases). Nominal model parameters for the simulated results are taken from the average EKF parameter estimates given in Section 8.2. The new milling model is used in generating all simulated results.

9.1 STABILITY LOBE DIAGRAMS

Stability lobe diagrams are considered one of the most important outcomes from the study of milling [51, 52]. These diagrams are used as a reference in choosing an

appropriate spindle speed for a given depth of cut that will result in a chatter-free milling process. The prediction of stability in an interrupted cutting operation (as in milling) is complicated by the fact that the equation of motion is different when the tool is cutting and when the tool is free of the workpiece. Furthermore, no exact analytical solution is known when the tool is in the cut [20]. One of the more successful ways of predicting the stability bound for milling is through the use of time finite element analysis (TFEA). Numerical methods can be used in determining stability; however, analytical methods (such as the TFEA method) are used given their ability to determine stability without simulating the system. The TFEA method forms an approximate solution by dividing the time in the cut (i.e. the time a given tooth is engaged in the workpiece) into a finite number of elements [8]. The approximate solution during the cut is matched with exact solution for free vibration to form a discrete linear map that relates the position and velocity at the beginning and end of each element to the corresponding values one period earlier. The approximate solution is required to match the exact solution at the beginning and end of each cut [20]. Eigenvalues of the discrete linearized system with a magnitude greater than one indicate instability (i.e. chatter).

The mathematical milling model shown in Eq. (49) is used in constructing the 2-DOF TFEA discrete time system (see tradition milling model in Chapters 2 and 3).

$$\begin{bmatrix} m_x & 0 \\ 0 & m_y \end{bmatrix}\begin{bmatrix} \ddot{X}(t) \\ \ddot{Y}(t) \end{bmatrix}+\begin{bmatrix} c_x & 0 \\ 0 & c_y \end{bmatrix}\begin{bmatrix} \dot{X}(t) \\ \dot{Y}(t) \end{bmatrix}+\begin{bmatrix} k_x & 0 \\ 0 & k_y \end{bmatrix}\begin{bmatrix} X(t) \\ Y(t) \end{bmatrix} = \boldsymbol{M}\ddot{\boldsymbol{x}}+\boldsymbol{C}\dot{\boldsymbol{x}}+\boldsymbol{K}\boldsymbol{x}=\begin{bmatrix} F_x \\ F_y \end{bmatrix} \tag{49}$$

The tangential and normal cutting forces, F_x and F_y, are functions of the current tool deflection, $\boldsymbol{x}(t)$, and the tool deflection of the previous tooth passage, $\boldsymbol{x}(t-\tau)$, where τ is

the time-delay in the system. When the tool is in the cut, there is no exact solution to the equation of motion because of the time-delay, τ. However, the time in the cut can be divided into multiple elements, and approximates of the vector displacement on a single element can be found as a linear combination of polynomial trial functions [3]. The displacement of the j^{th} element of the of the n^{th} period (i.e. the n^{th} tooth pass) is

$$\boldsymbol{x} = \sum_{i=1}^{4} \boldsymbol{a}_{ji}^{n} \phi_i(\varphi), \tag{50}$$

where φ is the "local" time in the j^{th} element and $\phi_i(\varphi)$ are the trial functions. The trial functions are defined such that their end conditions are either zero or unity, which allows the polynomials to directly correspond to the initial and final values of displacement, $\boldsymbol{x}$, and velocity, $\boldsymbol{v}$, of each element given by

$$\begin{aligned} &\boldsymbol{x}(t_{0j}^{n}) = \boldsymbol{a}_{j1}^{n}, \quad \boldsymbol{v}(t_{0j}^{n}) = \boldsymbol{a}_{j2}^{n}, \quad \sim \text{Initial Conditions} \\ &\boldsymbol{x}(t_{1j}^{n}) = \boldsymbol{a}_{j3}^{n}, \quad \boldsymbol{v}(t_{1j}^{n}) = \boldsymbol{a}_{j4}^{n}, \quad \sim \text{Final Conditions} \end{aligned} \tag{51}$$

where t_{0j}^{n} and t_{0j}^{n} are the times at the initial and final conditions of the j^{th} element [20]. The time-delayed displacement, velocity, and acceleration of the j^{th} element are given as

$$\boldsymbol{x}(t-\tau) = \sum_{i=1}^{4} \boldsymbol{a}_{ji}^{n-1} \phi_i(\tau), \tag{52}$$

$$\dot{\boldsymbol{x}} = \sum_{i=1}^{4} \boldsymbol{a}_{ji}^{n} \dot{\phi}_i, \tag{53}$$

$$\ddot{\boldsymbol{x}} = \sum_{i=1}^{4} \boldsymbol{a}_{ji}^{n} \ddot{\phi}_i. \tag{54}$$

The assumed solution given in Eqs. (50) and (52) – (54) is then substituted into the equation of motion in Eq. (49). Through the method of weighted residuals, two separate trial functions, which are a function of φ, are used to evaluate this expression with respect

φ. The resulting equations can be written in a single matrix expression for the j^{th} element during the cut.

$$\boldsymbol{N}\begin{Bmatrix} \boldsymbol{a}_{j1} \\ \boldsymbol{a}_{j2} \\ \boldsymbol{a}_{j3} \\ \boldsymbol{a}_{j4} \end{Bmatrix}^{n} = \boldsymbol{E} + \boldsymbol{P}\begin{Bmatrix} \boldsymbol{a}_{j1} \\ \boldsymbol{a}_{j2} \\ \boldsymbol{a}_{j3} \\ \boldsymbol{a}_{j4} \end{Bmatrix}^{n-1} \tag{55}$$

While the tool is in the cut, the position and velocity at the end of one element, $\boldsymbol{a}_{(j-1)3}$ and $\boldsymbol{a}_{(j-1)4}$, are equal to the position and velocity at the beginning of the next element, $\boldsymbol{a}_{j3}$ and $\boldsymbol{a}_{j4}$.

$$\begin{Bmatrix} \boldsymbol{a}_{j1} \\ \boldsymbol{a}_{j2} \end{Bmatrix}^{n} = \begin{Bmatrix} \boldsymbol{a}_{(j-1)3} \\ \boldsymbol{a}_{(j-1)4} \end{Bmatrix}^{n} \tag{56}$$

During free vibrations (i.e. when the tool is not cutting) an exact solution is know since the forces in Eq. (49) are zero. Therefore, a state transition matrix can relate the initial and final conditions during free vibration through the expression

$$\begin{Bmatrix} \boldsymbol{a}_{11} \\ \boldsymbol{a}_{12} \end{Bmatrix}^{n} = \left[e^{\boldsymbol{U}t_f} \right] \begin{Bmatrix} \boldsymbol{a}_{E3} \\ \boldsymbol{a}_{E4} \end{Bmatrix}^{n-1}, \tag{57}$$

where E is the number of finite elements in the cut, t_f is the free vibration time, and

$$\boldsymbol{U} = -\begin{bmatrix} 0 & \boldsymbol{M} \\ \boldsymbol{I} & 0 \end{bmatrix}^{-1} \begin{bmatrix} \boldsymbol{K} & \boldsymbol{C} \\ 0 & -\boldsymbol{I} \end{bmatrix}. \tag{58}$$

Combining Eqs. (55) – (57) results in the coefficients of the assumed solution, which describes a linear discrete system written as

$$\boldsymbol{A}\boldsymbol{a}_n = \boldsymbol{B}\boldsymbol{a}_{n-1} + \boldsymbol{C}_C, \tag{59}$$

or

$$\boldsymbol{a}_n = \boldsymbol{Q}\boldsymbol{a}_{n-1} + \boldsymbol{D}. \tag{60}$$

A full detailed derivation of this system is given by Bayly [3]. The stability of the system is determined by the eigenvalues of the matrix $\boldsymbol{Q}$. Eigenvalues with a magnitude greater than 1 correspond to instability (i.e. chatter).

A block diagram of the TFEA stability algorithm is given in Fig. 60. First, vectors of depth of cut and spindle speed are defined that provide the range over which the stability bound is calculated. Model, process, and numeric parameters are defined, and the Ω loop is then initiated. The time parameters (i.e. the time each tooth is in and out of the cut) and a state transition matrix, which is based on the model parameters and free vibration time, are defined for each spindle speed. The b loop is then initiated. The discrete time system is constructed into two separate matrices (matrices $\boldsymbol{A}$ and $\boldsymbol{B}$). These matrices include 3rd order polynomials and two trial functions. New $\boldsymbol{A}$ and $\boldsymbol{B}$ matrices are evaluated for each value of b and Ω. The eigenvalues of $\boldsymbol{Q}$ are then found, where $\boldsymbol{Q} = \boldsymbol{A}^{-1}\boldsymbol{B}$. If the maximum eigenvalue is greater than one, the system is unstable (i.e. the system contains chatter). Otherwise, the system is stable (i.e. chatter-free). A simulated 2-DOF TFEA stability diagram is given in Fig. 61 with b ranging from 1 to 10 mm and Ω ranging from 10,000 to 20,000 rpm. The area below the red line is the stable (chatter-free) region of the stability lobe diagram, and the area above the red line is the unstable (chatter) region. During a given milling process, it is desired to stay within the stable region for any given value of b. In most cases, if b is continually increased, the spindle speed, Ω, must be increased and/or decreased for the system to remain chatter-free.

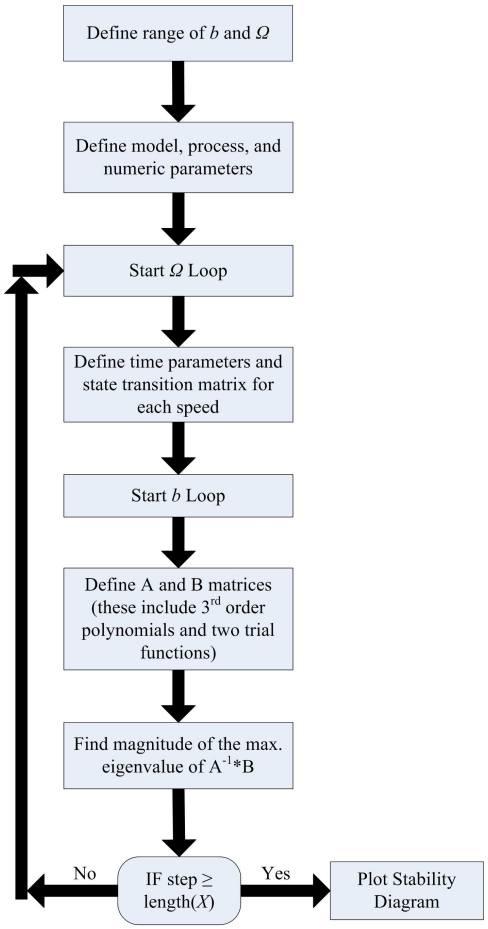

Fig. 60. Block diagram of the TFEA stability algorithm.

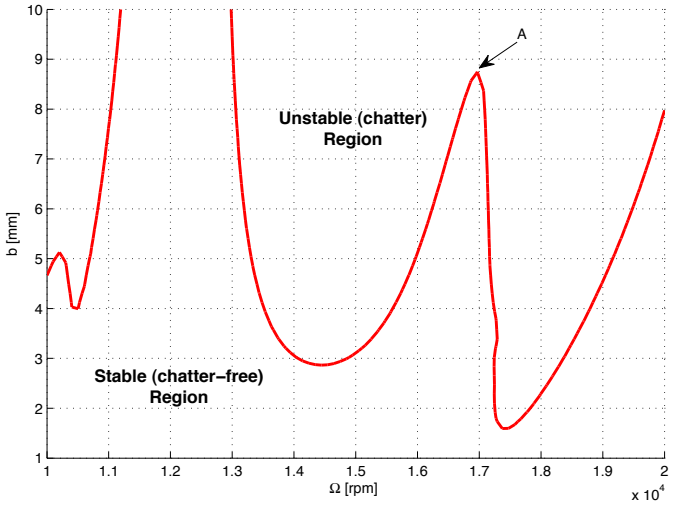

Fig. 61. TFEA stability lobe diagram.

9.2 AVOIDING CHATTER

To increase the range of b over which a simulated milling operation can remain chatter-free, a control system is designed that varies Ω to keep the current b versus Ω relationship within the stable region of the TFEA diagram in Fig. 61 (i.e. below the red line). During the simulated milling process, model parameter estimates are continually updated via the EKF given in Section 7.2. These parameter estimates are then used in generating a new TFEA stability bound, which provides knowledge of the stable cutting regions. The ability to update model parameters and stability bounds becomes much more important if a similar control system is to be implemented into an actual milling operation. As shown in Sections 8.2 and 8.3, nonlinearities and/or un-modeled dynamics in the experimental milling system cause parameter estimates based on the linear model to vary as b and Ω change. Therefore, updated parameter estimates are needed to provide a more accurate stability analysis of the system at the current depth of cut and spindle speed. Furthermore, this updating process allows the control system to account for tool wear over time. A description of the control system, and the process used to integrate the control system into a simulated milling process, is given in Section 9.2.1. The control system is then tested in Section 9.2.2 to show its ability to prevent chatter.

9.2.1 CONTROL SYSTEM

The block diagram in Fig. 62 shows the control system used in maintaining chatter-free vibrations for a simulated milling operation using the new milling model. Initially, process, model, and numerical parameters are defined within the main program. The milling simulation then begins with the start of the cutter revolution loop. For each

time step, the main program calls upon a subprogram that calculates the chip thickness using the new chip thickness model (see A in Fig. 62). A full description of the new milling model is given in Section 3.4. Once the simulation runs for a given number of seconds, t_{est}, the EKF subprogram is called (see B in Fig. 62) to estimate the model parameters from the simulated data produced by the main program. The time variable t_{est} is dependent on the current time step of the simulation not on the runtime of the simulation (i.e. t_{est} refers to the point in time currently being simulated).

Initial estimates of the model parameters (m_{est}, c_{est}, and k_{est}) and vectors of simulated deflection data, $\boldsymbol{X}$ and $\boldsymbol{Y}$, the depth of cut, $\boldsymbol{b}$, and time, $\boldsymbol{t}$, are passed into the EKF program. The first time the EKF program is called, m_{est}, c_{est}, and k_{est} are chosen at random within ±50% of their nominal values. See Section 7.2 for a detailed description of the EKF algorithm. Once new parameter estimates are found, those updated estimates are passed into the TFEA stability subprogram along with the current depth of cut, b_c, and spindle speed, Ω_c (see C in Fig. 62). The technique used in generating the TFEA stability curve is given in Section 9.1. The stability bound is generated over a given depth of cut and spindle speed range around b_c and Ω_c (i.e. the current values of b and Ω used in the simulation). If the location of b_c versus Ω_c is within a given distance, d, from the generated stability bound, the slope of the stability curve, $TFEA_{slope}$, at Ω_c is returned to the main program. Otherwise, a value of 0 is returned for $TFEA_{slope}$. For every simulated revolution of the tool, m, the spindle speed is adjusted within the main program using the following equation.

$$\Omega_m = \Omega_{m-1} + TFEA_{slope}(b_m - b_{m-1}) \tag{61}$$

Equation (61) is used to keep the b_c versus Ω_c relation away from the calculated stability bound (i.e. away from chatter vibrations). The variable d (i.e. the distance from the stability bound the current depth of cut and spindle speed must be for the control system to adjust the spindle speed) can be thought of as a safety factor in regards to the accuracy of the EKF estimates. For example, if the parameter estimates are thought to contain significant error, which will cause inaccuracies in the stability bound, d can be increased to ensure the system does not go unstable due to estimate errors.

If a concave down feature exists in the generated TFEA stability diagram, further increasing b will eventually cause the system to cross into the chatter region of the stability diagram. Such a concave down feature exists at point A in Fig. 61. In this situation, the feed of the tool, f, is stopped (i.e. the tool no longer engages the workpiece). The spindle speed is then increased or decreased until the b_c versus Ω_c relation is within a chatter free region of the stability diagram that does not contain a concave down feature. The feed rate is then incrementally increased until it reaches its original value. The feed is slowly increased so the tool does not feed into the workpiece too quickly at large depths of cut, which can cause the tool to momentarily experience chatter. The ability of the control system to recognize concave down features in the stability diagram, and adjust Ω and f accordingly, is not represented in the simplified block diagram in Fig. 62.

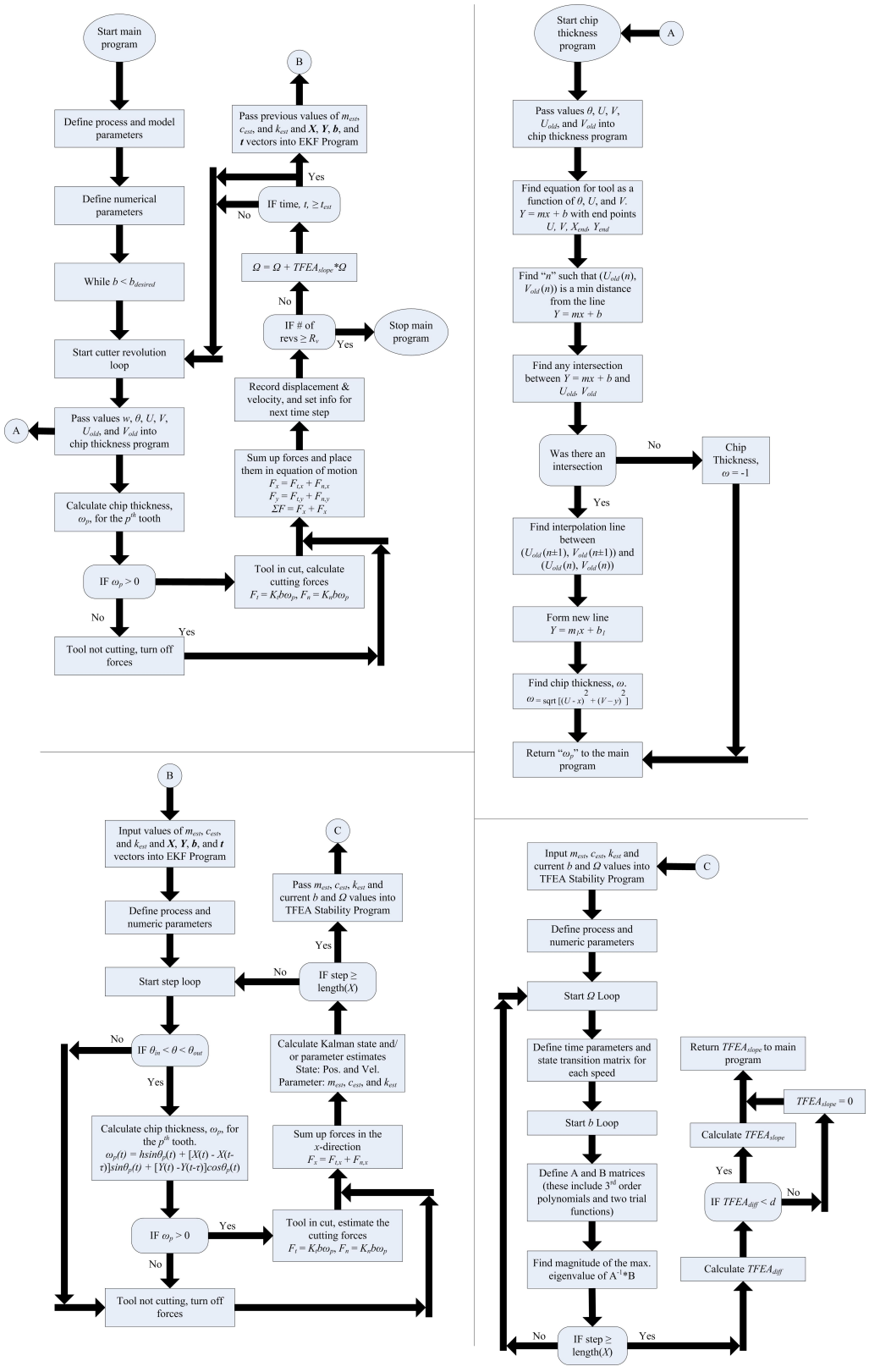

Fig. 62. Block diagram of the milling model and control system.

After the TFEA stability algorithm runs, the time variable, t_{est}, is updated to reflect the desired time for the next parameter estimation and stability diagram generation. The second time the EKF algorithm runs, initial guesses for m_{est}, c_{est}, and k_{est} are set equal to the parameter estimates found by the previous EKF estimation process (this is true for any consecutive estimate). The milling simulation continues to run until the current depth of cut, b_c, reaches its desired value, $b_{desired}$.

9.2.2 CONTROL SYSTEM TESTS

The control system described above is tested at four different initial sets of conditions. The initial spindle speeds, Ω_{start}, for tests 1 – 4 are 9,500, 10,000, 14,000, and 15,000 rpm, respectively. Nominal model parameter values are chosen for each test based on the average experimental EKF estimate results in Section 8.2 (see Table 6) for each corresponding Ω_{start} value. The TFEA stability diagrams generated from the nominal model parameters from tests 1 – 4 are given in plots (i – iv) of Fig. 63, respectively (see red lines). For each test, parameter estimates and stability curves based on those estimates are generated every 0.25 seconds (i.e. t_{est} initially equals 0.25 seconds and is then updated as $t_{est} = t_{est} + 0.25$ seconds each time a stability curve is generated). In each of the four tests, b linearly increases from its initial value of either 1 or 2 mm to a final value of 10 mm. Referring to Table 5 in Section 8.2, $b = 10$ mm is well outside the chatter-free range of all experimental and simulated results. The b versus Ω paths the control system follows for tests 1 – 4 are shown as blue dots in plots (i – iv) of Fig. 63, respectively. In each test, the control system keeps the milling operating below the stability line (i.e. within the chatter-free region).

The stability bounds found from each set of parameter estimates are given as black dots in Fig. 63. The stability bounds found from the estimated parameters lie very close to (if not on top of) the nominal stability bound, which verifies the EKF algorithm estimates are accurate. The TFEA stability algorithm only calculates the stability curve over a small window near the current b and Ω values. By minimizing this window, the calculation time in generating a stability curve is greatly reduced. The bounds of the window used in the 4 tests in Fig. 63 are b_c – 0.3 mm, b_c + 2.0 mm, Ω_c – 400 rpm, and Ω_c + 400 rpm (b_c and Ω_c are the current simulated depth of cut and spindle speed, respectively).

The error in the first set of EKF parameter estimates, m_{est}, c_{est}, and k_{est}, is higher than consecutive estimate due to the inaccuracy of the initial parameter guesses. The initial guess for each parameter is randomly chosen within ±50% of their nominal values. The inaccuracy in the parameter estimate correlates to an error in the TFEA stability curve. This is most evident in test 4, where the first calculated stability bound (see black dots) is well below the nominal stability bound (see red line) near point G in plot (iv) of Fig. 63. Since the initial parameter guesses for any consecutive estimate are based on the previous estimate, the error in the calculated stability curve is reduced after the first estimate. The tool deflection in the x-direction, X, and the once-per-tooth-pass deflection data, X_n, for each test is given in Fig. 64. As shown by the X_n data (see blue data points), the control system is able keep the simulated milling process chatter-free given the variety of initial spindle speeds and model parameters.

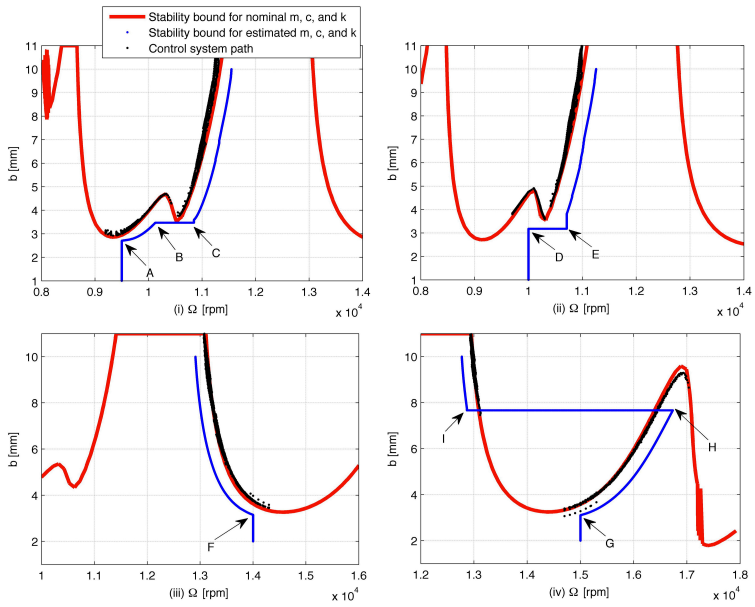

Fig. 63. Control system paths (see blue data points) for 4 separate initial spindle speeds, Ω_{start}: (i) Test 1: Ω_{start} = 9,500 rpm, (ii) Test 2: Ω_{start} = 10,000 rpm, (iii) Test 3: Ω_{start} = 14,000 rpm, (iv) Test 4: Ω_{start} = 15,000 rpm. Nominal model parameters are used in generating the nominal TFEA stability curve shown in red. The estimated stability bounds are shown as black dots.

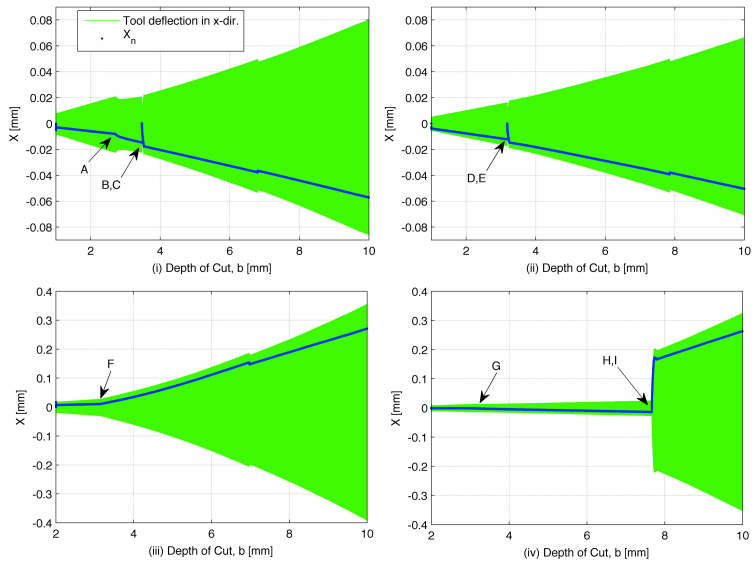

Fig. 64. Tool deflection in the *x*-direction, X, and once-per-tooth-pass deflection, X_n, for the 4 control cases shown in Fig. 63: (i) Test 1: Ω_{start} = 9,500 rpm, (ii) Test 2: Ω_{start} = 10,000 rpm, (iii) Test 3: Ω_{start} = 14,000 rpm, (iv) Test 4: Ω_{start} = 15,000 rpm.

Two of the more interesting control tests shown in Figs. 63 and 64 (specifically tests 1 and 4) are described in detail below.

- The following is a description of test 1 (see plot (i) in Figs. 63 and 64). Points of interest are labeled A – C in each figure.
  - The simulation begins at the following milling conditions: Ω = 9,500 rpm, b = 1 mm, f = 0.0635 mm/tooth, and h = 0.382 mm. The nominal model parameters are m = 0.0316 kg, c = 7.6810 N-s/m, and $k = 9.1036\times10^5$ N/m. The depth of cut linearly increases to a final value of 10 mm.
  - The spindle speed, Ω, remains constant as b increases from 1 mm to approximately 2.8 mm (i.e. point A). At point A, Ω begins to increase to keep the b versus Ω relations within the chatter-free region of the stability bound (Ω increases since the slope of the TFEA stability curve is positive). The spindle speed continues to increase as b increases from point A ($b \approx$ 2.8 mm) to point B ($b \approx$ 3.5 mm).
  - At point B, the control system recognizes that there is a concave down feature in the TFEA stability curve; therefore, further increasing b and/or Ω may result in the onset of chatter. At this point, the feed of the tool is completely stopped (i.e. f = 0 mm/tooth). Since b is dependent on the position of the tool, b remains constant at 3.5 mm when f = 0 mm/tooth. The spindle speed is increased by 10 rpm/rev until the b versus Ω relations are within a stable region near Ω = 10,800 rpm (i.e. point C).
  - At point C, the feed rate, f, is incrementally increased by f_i*0.005 for each revolution of the tool until the initial feed rate, f_i, of 0.0635 mm/tooth is reached.

This slow increase in the feed rate results in a smooth chatter-free tool response (see points B, C in plot (i) of Fig. 64).

- After point C, Ω is once again increased as b increases to keep the b versus Ω relations within the chatter-free region of the stability bound.
- The simulation ends when b reaches 10 mm.

➢ The following is a description of test 4 of the control system (see plot (iv) in Figs. 63 and 64). Points of interest are labeled G – I in each figure.

- The simulation begins at the following milling conditions: Ω = 15,000 rpm, b = 2 mm, f = 0.0635 mm/tooth, and h = 0.382 mm. The nominal model parameters are m = 0.0356 kg, c = 9.6982 N-s/m, and $k = 9.9150\times10^5$ N/m. The depth of cut linearly increases to a final value of 10 mm.
- The spindle speed, Ω, remains constant as b increases from 2 mm to approximately 3.1 mm (i.e. point G). At point G, Ω begins to increase to keep the b versus Ω relations within the chatter-free region of the stability bound (Ω increases since the slope of the TFEA stability curve is positive). The spindle speed continues to increase as b increases from point G ($b \approx$ 3.1 mm) to point H ($b \approx$ 7.8 mm).
- At point H, the control system recognizes that there is a concave down parabola in the TFEA stability curve. In this situation, further increasing b and/or Ω will ultimately result in chatter. At this point, the feed of the tool is completely stopped (i.e. f = 0 mm/tooth) and b remains constant at 7.8 mm. The spindle speed is decreased by 10 rpm/rev until the b versus Ω relations are within a stable region near Ω = 12,800 rpm (i.e. point I).

- At point I, the feed rate, f, is incrementally increased by f_i*0.005 for each revolution of the tool until the initial feed rate, f_i, of 0.0635 mm/tooth is reached. Referring to points H and I in plot (i) of Fig. 64, the deflection magnitude of the tool significantly increases when Ω is reduced from approximately 16,700 rpm at point H to 12,800 rpm at point I. This increased magnitude is a result of a change in the tool dynamics at lower spindle speeds. In general, the deflection magnitude of the tool increases as Ω decreases at a given b. Even though the deflection magnitude is increased, the milling operation remains chatter-free (see X_n data in plot (i) of Fig. 64).
- Since the slope of the stability curve is negative at point I, Ω begins to decrease as b increases to keep the b versus Ω relations within the chatter-free region of the stability bound.
- The simulation ends when b reaches 10 mm.

9.3 STABILITY TRACKING WITH AVERAGE RMS VALUES

The root-mean-square (RMS) is a statistical measure of the magnitude of a varying quantity [53]. For a milling process at a given depth of cut, the once-per-revolution tool deflection in the x-direction, $X_{m,}$ is constant for chatter-free vibrations and varies for chatter vibrations (this is true whether or not runout exists in the system). Therefore, calculating the RMS value of X_m (i.e. calculating the variance magnitude of X_m) can be used in determining if chatter vibrations are present in a given milling process. Specifically, if the system is chatter-free, the variance in X_m is zero (i.e. the RMS value of X_m is zero). Furthermore, if chatter vibrations exist, the variance in X_m is some positive number (i.e. the RMS value of X_m is greater than zero). Even during chatter-free

vibrations, some variation in the X_m data from experimental tests is expected due to sensor noise and sampling rate. By averaging the RMS value of the current tool revolution with the RMS values from previous revolutions, the effect of these factors can be reduced. The average RMS value of X_m for each tool revolution, *rev*, is calculated as

$$rms_{rev} = \left(\sum_{j=rev-p_r}^{rev-1} rms_j + \sqrt{\sum_{m=rev-p_r}^{rev} (X_m - X_{mean})^2} \right) / p_r \tag{62}$$

where p_r is the number of previous revolutions used in calculating rms_{rev}, X_m is the once-per-revolution tool displacement in the *x*-direction, and X_{mean} is the value of a first-order polynomial fit through [rev-p_r, rev-(p_r-1), … , rev] and [$X_{rev\text{-}p_r}$, $X_{rev\text{-}(p_r\text{-}1)}$, … , X_{rev}] and evaluated at each corresponding tool revolution. Values of X_m from the previous p_r tool revolution are used in calculating the average RMS value for the current revolution, rms_{rev}. As stated above, little-to-no variance in the X_m data exists during chatter-free vibrations; therefore, $X_m \approx X_{mean}$ and $rms_{rev} \approx 0$. Accordingly, when $rms_{rev} > 0$ (i.e. some variance in the X_m data exists), chatter vibrations exist. Larger values of rms_{rev} represent the onset of larger magnitude chatter vibrations.

Plots (ii) of Figs. 65 and 66 give rms_{rev} values for the respective simulated and experimental deflection data given in plots (i). In both cases, *b* is increased from 0 to 6 mm along the length of the workpiece at Ω = 15,000 rpm. Seven previous revolutions (i.e. p_r = 7) are used in calculating rms_{rev} for both simulated and experimental deflection data. Plots (ii) show how rms_{rev} changes as the simulated and experimental systems transitions from chatter-free to chatter vibrations. For the simulated result (see Fig. 65), rms_{rev} increases from a value near 0 to approximately 6.8×10^{-3} mm as the system passes through the bifurcation point at b = 3.99 mm. The values of rms_{rev} then begin to oscillate

as b continues to increase (this is due to the to the tool deflection oscillations specific to chatter). The mean values of these oscillations increase as b continues to increase (i.e. as the magnitude of the chatter vibrations increase). For the experimental result (see Fig. 66), rms_{rev} remains below 0.7×10^{-3} mm until the first bifurcation occurs at b = 3.55 mm. Values of rms_{rev} are not zero in the chatter-free range due mainly to noise in the experimental deflection data and the sampling rate at which the data is taken. The effects of these factors on the magnitude of rms_{rev} are reduced, but not eliminated, by calculating the average RMS value for each revolution. From b = 3.55 to 5.52 mm, rms_{rev} oscillates at a mean value of 3.2×10^{-3} mm. At b = 5.52 mm, rms_{rev} once again increases to a value near 6.0×10^{-3} mm as the system undergoes a second bifurcation.

The results given in Fig. 66 show that rms_{rev} can be experimentally used in detecting the onset of chatter vibrations. Tracking rms_{rev} on-line can lead to the implementation of various actions that can help warn against or stop chatter vibrations once they occur. The simplest action is to warn the operator with a light and/or alarm when rms_{rev} reaches a predetermined magnitude (i.e. when chatter vibrations are know to exist). The milling machine could also stop its feed rate completely if large enough rms_{rev} values are detected. However, neither of these options prevents chatter from occurring. To prevent chatter, a control system similar to the one discussed in Section 9.2 is required (this control system uses EKF estimates of m, b, and k to calculate and update stability bounds of the system). However, tracking rms_{rev} values can be used as a failsafe (i.e. a way to prevent excessive chatter) in situations where poor parameter estimates may cause the control system to fail in avoiding/preventing the onset of chatter.

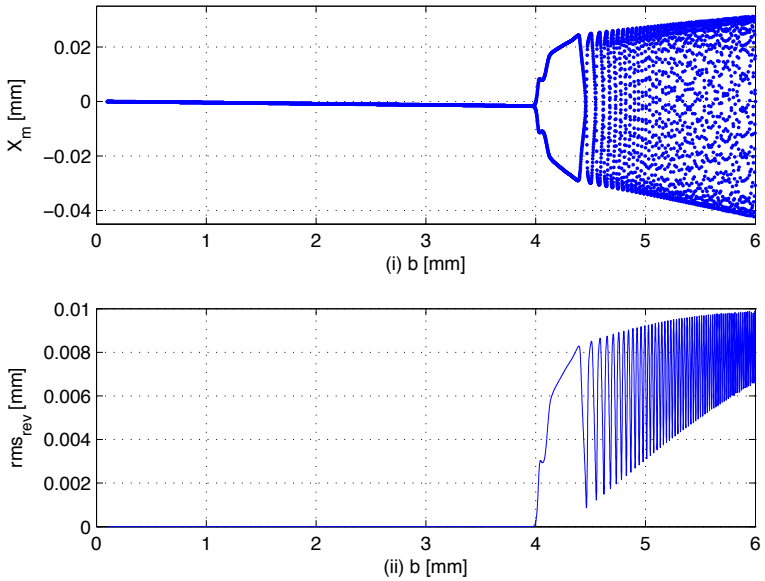

Fig. 65. (i) Simulated once-per-revolution deflection data, X_m, for and increasing b and Ω = 15,000 rpm. (ii) rms_{rev} values for the simulated X_m data given in (i). Bifurcation occurs at b = 3.99 mm.

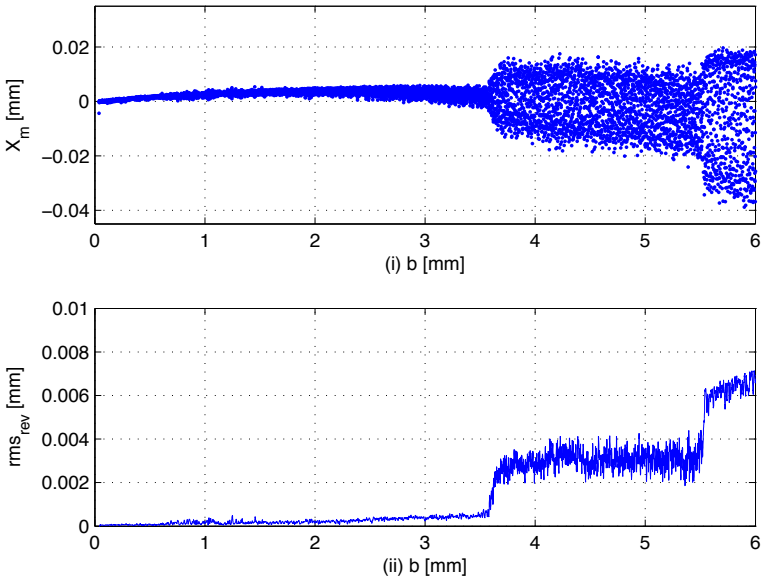

Fig. 66. (i) Experimental once-per-revolution deflection data, X_m, for and increasing b and Ω = 15,000 rpm. (ii) rms_{rev} values for the experimental X_m data given in (i). First bifurcation occurs at b = 3.55 mm, and second bifurcation occurs at b = 5.52 mm.

9.4 RESULTS AND CONCLUSIONS

In this chapter, a control system is presented that is capable of predicting and avoiding chatter vibrations in a simulated milling process. This control system uses updated EKF model parameter estimates to generate TFEA stability bounds that indicate stable and unstable relations between b and Ω. The ability of the control system to periodically update parameter estimates and stability bound information allows it to adapt to changes in the milling system. Once a stability bound of the system is known, the spindle speed and/or feed rate of the milling operation can then be varied to keep the current depth of cut versus spindle speed relation within the stable (i.e. chatter-free) region. This control system is shown to keep various simulated milling processes with different initial spindle speeds and model parameters completely chatter-free. An alternative method of tracking stability is also presented that calculates average RMS values of the once-per-tool-revolution deflection data in the x-direction. This method is shown to be effective in determining the onset of chatter for both simulated and experimental deflection data; however, it is unable to predict or prevent chatter vibrations entirely. Therefore, it should only be used as a failsafe in situations where poor parameter estimates may cause the control system to fail in avoiding/preventing the onset of chatter.

Chapter 10 PARAMETER INFLUENCE ON STABILITY

Parameter estimation is well recognized as a theoretically difficult problem; moreover, estimating a large number of parameters is often computationally very expensive. This has led to the development of techniques determining which parameters affect the dynamics of the system the most in order to choose the parameters that are important to estimate [30, 54]. As shown in Chapter 9, TFEA analysis can be used to find regions in parameter space where time-delay systems (such as the milling system) are stable and unstable. The stability of the milling model is affected by several parameters such as mass, damping, stiffness, depth of cut, and spindle speed. The cutting coefficients, K_t and K_n, also affect the stability of the milling system, but they are not considered in the following parameter analysis. The following is the result of a study using TFEA analysis to show how sensitive stability is to changes in parameters m, c, k, and Ω. The effect of each parameter on the TFEA stability bound is given in Section 10.1, and a summary of the results in presented in Section 10.2. The results given here are for an up-milling process with h = 0.382 mm and f = 0.0635 mm/tooth

10.1 PARAMETER SENSITIVITY ON TFEA STABILITY ANALYSIS

The solid black line in Fig. 67 represents the TFEA stability curve for the following set of model parameters (nominal values): m = 0.03528 kg, c = 9.6982 N-s/m, and $k = 9.9150\times10^5$ N/m. Three separate points (A, B, and C) along this nominal stability curve are chosen to test how changes in the model parameters and spindle speed affect the stability curve (i.e. affect the depth of cut at which the system becomes unstable, b^*).

Point A in Fig. 67 is located at a local minimum of the stability curve (Ω = 14,400 rpm), point C is located at a local maximum (Ω = 16,920 rpm), and point B is located between points A and C where the slope of the stability curve is positive (Ω = 15,800 rpm). At each point, the model parameters and spindle speed are independently increased and decreased over a range of -1.5% to 1.5% from their nominal values. Stability curves are given in Fig. 68 for the cases when each model parameter is increased 1.5% from its nominal value. Increasing m causes the stability curve to move to the left and slightly downward (8 o'clock direction), increasing c causes the curve to move upward (12 o'clock direction), and increasing k causes the curve to shift to the right and upward (2 o'clock direction). Decreasing each of these parameters results in the exact opposite shift in the stability curve as given above. The changes in b^* (i.e. the changes in the point at which the model will become unstable at a given Ω) resulting from varying m, c, k, and Ω over the full range (-1.5% to 1.5%) are shown in plot (i) of Figs. 68 – 70 for points A, B, and C, respectively.

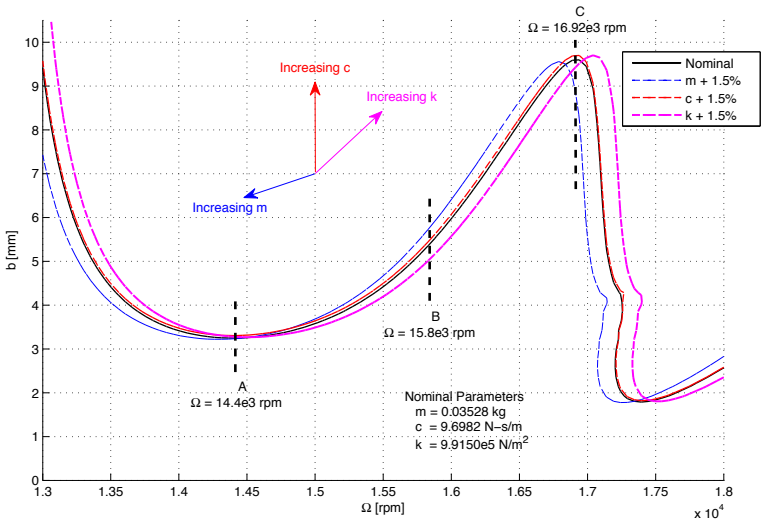

Fig. 67. TFEA stability diagram shift when model parameters (m, c, and k) are increased by 1.5% from their nominal values.

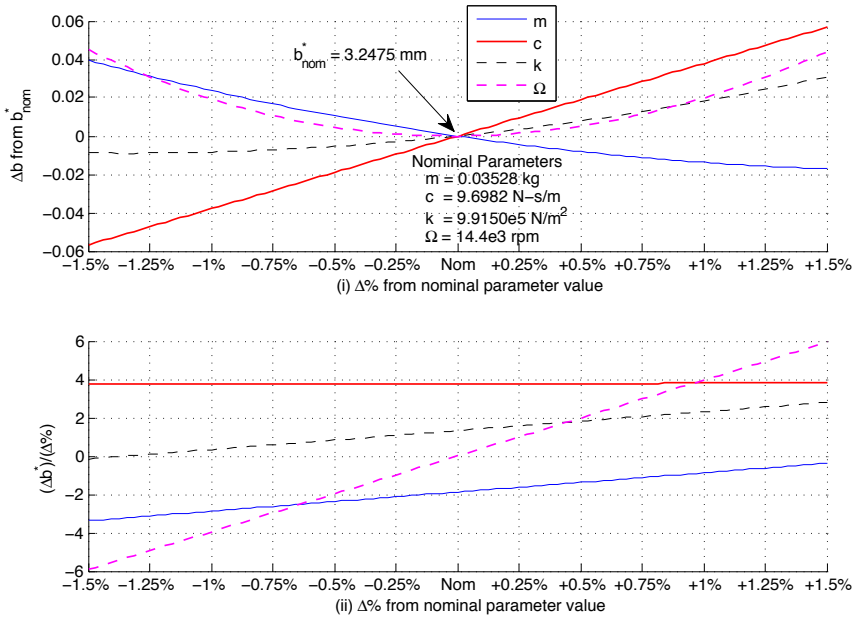

Fig. 68. Results are given at a nominal spindle speed, *Ω*, of 14,400 rpm (see point A in Fig. 67). (i) Change in b^* resulting from percent changes in *m*, *c*, *k*, and *Ω* from their nominal values. (ii) Derivative of the curves given in plot (i).

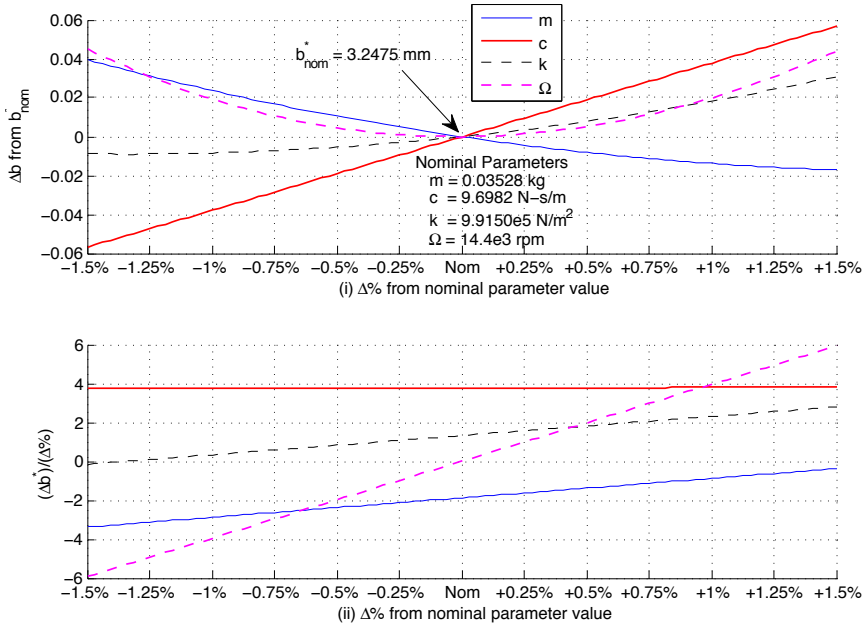

Fig. 69. Results are given at a nominal spindle speed, *Ω*, of 15,800 rpm (see point B in Fig. 67). (i) Change in b^* resulting from percent changes in *m*, *c*, *k*, and *Ω* from their nominal values. (ii) Derivative of the curves given in plot (i).

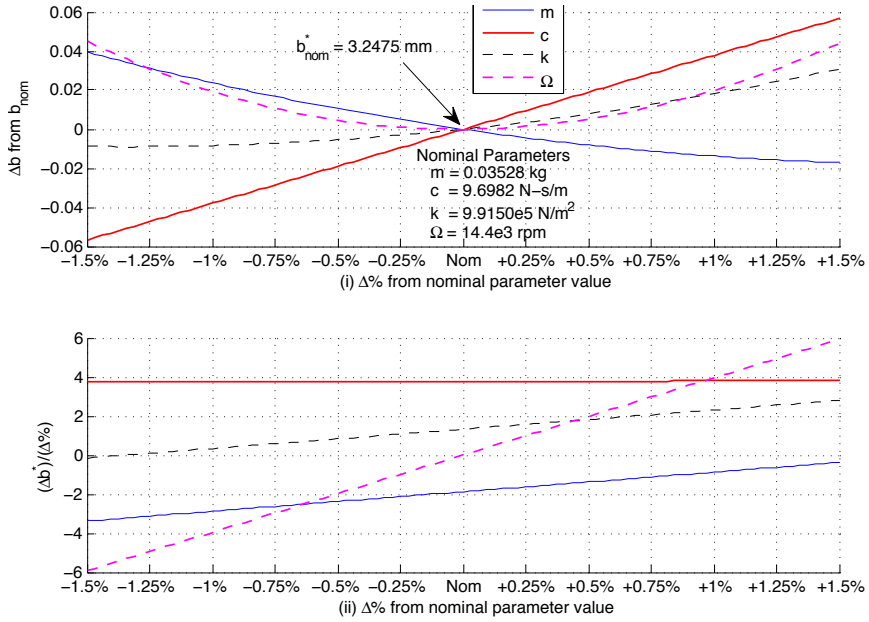

Fig. 70. Results are given at a nominal spindle speed, *Ω*, of 16,920 rpm (see point C in Fig. 67). (i) Change in b^* resulting from percent changes in *m*, *c*, *k*, and *Ω* from their nominal values. (ii) Derivative of the curves given in plot (i).

From plot (i) of Fig. 68, it is shown that *c* has the largest and *k* has the smallest affect on Δb^* at point A in Fig. 67. The spindle speed, *Ω,* and *m* cause similar changes in b^* when these parameters are decreased, yet *Ω* causes a slightly larger Δb^* when the parameters are increased. Plot (ii) of Fig. 68, gives the slope (i.e. derivative) of the curves in plot (i). The derivative of each curve is expressed as $\Delta b^*/(\Delta\%$ from nominal). From plot (ii), it is shown that varying the damping parameter, *c*, results in a linear change in b^* at point A in Fig. 67. Changes in parameters *Ω*, *m*, and *k* do not provide a linear relation in Δb^*. At point B in Fig. 67, the parameters that result in the largest to smallest Δb^* are *Ω*, *k*, *m*, and *c*, respectively (see plot (i) of Fig. 69 for parameter influence at point B). Plot (ii) of Fig. 69 shows a linear relation between Δb^* and changes in parameters, *m*, *c*, and *k* (*Ω* does not provide a linear relation). Finally, plot (i) of Fig. 70 shows that *Ω* and *c* have the largest and smallest affect on Δb^* at point C in

Fig. 67. When comparing parameters m and k, m results in a larger Δb^* when the parameters are increased, and k results in a larger Δb^* when the parameters are increased. Similar to point A in Fig. 67, the only parameter that results in a linear relation with Δb^* at point C is the damping, c (see plot (ii) of Fig. 70). Furthermore, c is the only parameter that maintains a linear relation with Δb^* at points A, B, and C in Fig. 67.

Table 7. Ranking the importance of changes in m, c, k, and Ω on Δb^* at points A, B, and C in Fig. 67 for when the parameters are increased and decreased. Rankings of 1, 2, 3, and 4 represent the parameters that cause the largest to smallest Δb^*, respectively.

		Model/Process Parameters			
		m	c	k	Ω
Point A	**Increasing Par.**	3	1	4	2
	Decreasing Par.	2	1	4	3
Point B	**Increasing Par.**	3	4	2	1
	Decreasing Par.	3	4	2	1
Point C	**Increasing Par.**	2	4	3	1
	Decreasing Par.	3	4	2	1
Total		**16**	**18**	**17**	**9**

Parameter m, c, k, and Ω are ranked in Table 7 on their affect on Δb^* as they are increased and decreased from their nominal values at points A, B, and C in Fig. 67. Rankings of 1, 2, 3, or 4 represent the parameters that cause the largest to smallest Δb^*, respectively. Inspecting Figs. 68 – 70, rank values for each parameter are found at points A, B, and C, respectively. Once rankings are obtained at each point, the ranking numbers for each parameter are added together to find the parameters with the largest overall affect on Δb^* (i.e. the largest change in the stability bound of the TFEA diagram over a range of Ω). Smaller summed values correspond to parameters that cause larger changes in b^*. From Table 7, it is shown that varying Ω has the largest overall affect on the stability bound of the system over a range of initial spindle speeds. As for the model

parameters, varying m, k, and c from their nominal values results in the largest to smallest change in b^*, respectively.

10.2 RESULTS AND CONCLUSIONS

As shown in Table 7, the damping parameter, c, is found to have the smallest overall effect on stability over a range of Ω (i.e. at points A, B, and C in Fig. 67). The damping does, however, have the largest affect on Δb^* at point A (Ω = 14,400 rpm). At point A, the magnitudes of Δb^* resulting from offsets in the nominal values of m, c, k, and Ω are smaller for each parameter than at points B or C (see plot (i) in Figs. 68 – 70). When varying the damping, c, from -1.5% to 1.5% of its nominal value, the slope and magnitude of Δb^* remains relatively consistent at points A, B, and C. In fact, the slope of Δb^* for parameter c is always positive, always linear, and has a value ranging from 3.75 to 6.6 mm/(% from nominal) (see plot (ii) in Figs. 68 – 70). On the other hand, the slopes of Δb^* for m, k, and Ω at points A, B, and C change sign, are not always linear, and have large changes in magnitude. Therefore, changes in b^* at a given Ω are more predictable for c than for m, k, or Ω. However, damping is typically by far the most uncertain parameter found in system parameter identification studies. In Section 7.2.2, the estimate of the damping is shown to be the only model parameter affected by runout in the milling system. This means that the parameter, c, still has great importance when attempting to predict stability. While it has the strongest influence on stability, the spindle speed, Ω, is the most easily found parameter with the least amount of uncertainty in the milling system since it is both directly measured and tightly controlled.

Chapter 11 SUMMARY

The notable findings and results from this research are summarized in Section 11.1. Suggestions for future work are presented in Section 11.2. The items discussed in the future work will expand upon the milling research given in this dissertation, providing an even better understanding of milling dynamics and bifurcations and also establish on-line chatter detection and prevention techniques. An on-line parameter estimation procedure and experimental results are given (this is the first step in integrating a control system based on parameter estimates into an actual milling/CNC machine). An on-line root-mean-square (RMS) method and experimental results are also given (this technique is capable of indicating the onset of chatter vibrations). Finally, A housing design is discussed that is capable of protecting the sensor package (i.e. the capacitance sensors and laser tachometer) from the machining environment.

11.1 COMPLETED WORK AND CONCLUSIONS

In this research, two mathematical models (a tradition and new model) are used in simulating a high-speed end-milling process. Both models use equations given by Altintas [6] for calculating the forces on the tool when it is engaged in the workpiece. The models differ in the way the uncut chip thickness is calculated (the force on the tool is a function of the chip thickness). The traditional milling model assumes a circular tool path with a built in time-delay (i.e. it takes into account the workpiece surface created by the previous tooth pass) in calculating the chip thickness. The new model calculates the chip thickness through the knowledge of multiple time-delays (i.e. it takes into account

the workpiece surface created by multiple tooth passes). The new model also accounts for the trochoidal motion of the tool, which is more representative of the actual milling operation. When compared to the traditional model, the trochoidal motion represented by the new model results in slightly larger simulated chip thickness magnitudes (this assumes chatter-free tool vibration). The new model is also capable of calculating the chip thickness at any rotational angle, θ, which is an obvious advantage over the traditional model. The traditional model only calculates the chip thickness within a defined range of θ values.

Simulated bifurcation diagrams from the new and traditional models are compared with experimental bifurcation results for an increasing and decreasing depth of cut, b. The new milling model is able to better predict the dynamics and bifurcation points of the experimental results. Through both simulated and experimental results, the milling system is shown to contain a subcritical bifurcation (i.e. shown to contain hysteresis). Within the hysteresis region, a stability jump (i.e. a jump from chatter-free to chatter equilibrium) is achieved through a disturbance input to the system. When increasing b along the length of the workpiece, it is found that feeding the tool down into the workpiece material (i.e. using T.P. #1 in Fig. 42) decreases the range over which the system is chatter-free. It is assumed that the downward feed of the tool increases the forces on the tool, resulting in the formation of chatter vibrations at smaller depths of cut. Therefore, T.P. #2 in Fig. 42, which eliminates the downward feed of the tool, should be used when increasing b along the workpiece.

Simulated results from the new milling model are performed with slight offsets in the tooth radii (this simulates runout in the system). Runout is shown to increase the

period of tool motion from 1/2 to 1 full revolution. Uneven force magnitudes applied to tooth #1 and #2 as they are in contact with the workpiece cause slight changes in the tool motion and result in an increase in the tool motion period. By comparing the simulated and experimental results, it is concluded that runout exists in the tool/spindle of the CNC machine used in collecting experimental data. The exact amount of runout cannot be derived from the experimental results given here. However, it can be concluded that runout is present in the experimental milling system. Therefore, runout should be considered in the analytical milling model to improve its ability to more closely match the dynamics of an actual milling operation.

A discrete Kalman filter algorithm and a discrete EKF algorithm are developed using the traditional milling model. Both algorithms are found to accurately estimate the milling states in the x-direction (specifically the tool displacement, X) given simulated and experimental deflection data and tool rotation angle. Runout causes noise in the parameter estimate of damping, c, and also increase its estimate error. It is also found that EKF parameter estimates of experimental deflection data vary as the spindle speed and/or the depth of cut change. The model parameters change in order for the linear model, which contains several assumptions, to adapt to changes in the nonlinear system. Therefore, a single set of model parameter estimates cannot be used to accurately represent a milling operation over a range of Ω or b. For this reason, EKF parameter estimates must be updated to produce m, c, and k values that best describe the system at the current milling conditions. Unlike the static and dynamic model parameter tests presented in Section 4.3, parameter estimation with the EKF algorithm is fast, accurate, repeatable, is not influenced by human error, and can be performed on-line.

A control system is presented that is capable of predicting and avoiding chatter vibrations in a simulated milling process. This control system uses updated EKF model parameter estimates to generate TFEA stability bounds that indicate stable and unstable regions in the space defined by depth of cut, b, and spindle speed, Ω. The spindle speed and/or feed rate of the milling operations are varied to keep the current b versus Ω relation within the stable (i.e. chatter-free) region defined by these stability bounds. This control system is able to keep various simulated milling processes with different initial spindle speeds and model parameters chatter-free. An alternative method of tracking stability is also presented that calculates average root-mean-square (RMS) values of the once-per-tool-revolution deflection data in the x-direction. This method is shown to be effective in determining the onset of chatter for both simulated and experimental deflection data; however, it is unable to predict or prevent chatter vibrations entirely. Therefore, tracking average RMS values should only be used as a failsafe in situations where poor parameter estimates may cause the control system to fail in avoiding/preventing the onset of chatter.

Through TFEA stability analysis, the damping parameter, c, is found to have the smallest overall effect on stability. Furthermore, parameter c is found to be the only parameter that provides a consistent, positive, and linear relation to stability bound of the system over the range of tested spindle speeds. Parameters m, k, and Ω do not provide a linear relation to the stability bound and have wide variances in their effect on stability depending on the tested location on the stability curve. Therefore, changes in the stability bound at a given nominal spindle speed are more predictable for c than for m, k, or Ω. However, damping is found to be the most uncertain parameter in the EKF parameter

estimation study. The EKF estimate of c is affected by runout in the system far more than any other parameter. Therefore, c still has great importance when attempting to predict stability in the milling system. The strongest influence on stability is the spindle speed, Ω. However, Ω has little-to-no uncertainty in the milling system since it is both directly measured and tightly controlled.

11.2 FUTURE WORK

The following is a list of items that will further expand the milling research given in this dissertation.

1. Add high-resolution tachometer for the sensor configuration for more accurate tool phase measurements.
2. Perform experimental tests similar to those given in Chapter 8 for a down-milling process. Simulations from the traditional and new milling models should be compared with the experimental results.
3. Investigate cutting edge effects on tool dynamics and stability.
4. Study mode shapes of the tool.
5. Estimate other model parameters within the EKF algorithm such as the cutting force coefficients, K_t and K_n, or the amount of runout in the system (i.e. the proper offset in the tooth radii).
6. Perform on-line EKF parameter estimation tests and document results.
7. Perform on-line root-mean-square (RMS) calculations to track stability.
8. Further investigate observability issue of EKF.
9. Develop methods to integrate chatter control algorithm into milling/CNC machine.

10. Design and build sensor housing for protecting the sensor package from the machining environment.

Items 6, 7, and 10 in the list above are partially complete. The progress of each item is given here. The methods for obtaining and analyzing experimental data for use in on-line parameter estimation and RMS calculations are given in Sections 11.2.1 and 11.2.2, respectively. A proposed sensor housing design is then given in Section 11.2.3.

11.2.1 ON-LINE PARAMETER ESTIMATION

Chatter in a milling process can bring about many undesirable effects such as poor surface quality, reduced dimensional accuracy, a reduction in tool life and production rate, and damage to the machine tool itself. On-line identification of model parameters can lead to the prevention of these unfavorable effects and, therefore, increase productivity and the quality of parts [55]. As shown in Sections 8.2 and 8.3, the ability to update the model parameter estimates is especially important given that experimental parameter estimates are found to vary depending on the spindle speed, Ω, and depth of cut, b. These changes in parameter values are a result of linear assumptions of the mathematical model used in calculating the model estimates. Tool wear and/or tool tooth chipping will also lead to changes in parameter values. Therefore, having the ability to periodically update parameter estimates is crucial when defining a system over a range of Ω, over a range of b, and/or over an extended period of time. Obtaining EKF estimates during the milling operation is the first step in integrating a control system (similar to the one given in Section 9.2) into a milling machine that is capable of generating stability load diagrams used to avoid chatter vibrations by varying Ω and/or the feed rate, f.

The preliminary on-line parameter estimation results are given here. To calculate EKF parameter estimates of m, c, and k, the DAC system given in Section 4.1 is used in collecting snapshots of experimental deflection and tachometer data during the milling operation. The Labview® VI shown in Fig. 71 is used for collecting and analyzing the experimental data. The block diagram in Fig. 72 shows the process used in obtaining experimental data and calculating parameter estimates for that data. First, the spindle speed of the milling machine is increased to the rpm value the milling operation is to be performed at. Before the tool engages the workpiece, data is collected and analyzed to find the free-vibration (or no-load vibration) in the x and y-directions. Once the average free-vibration of the tool is found, the milling operation and EKF parameter estimation process are initiated. As the tool engages into the workpiece, a section of deflection and tachometer data is collected. The average free-vibration of the tool is subtracted from this newly obtained deflection data. The deflection data is then extrapolated to a time step of 1e-6 seconds to be used within the EKF algorithm (a smaller time step results in more accurate parameter estimates). The extrapolated deflection data along with initial guesses for the model parameters are then sent to the EKF algorithm where model parameter estimates are found and displayed. Plots (i – iii) of Fig. 73 give the respective on-line parameter estimates of m, c, and k for experimental deflection data at b = 2.54 mm and Ω = 14,000 rpm (three sets of experimental test results are given). The estimates of the mass, m, and stiffness, k, are very similar for each of the three tests. However, the estimates of the damping, c, vary slightly. It is expected that improving the method used in obtaining the tool phase will solve this problem; however, further investigation is needed to determine the exact cause of the variance in the estimate of c.

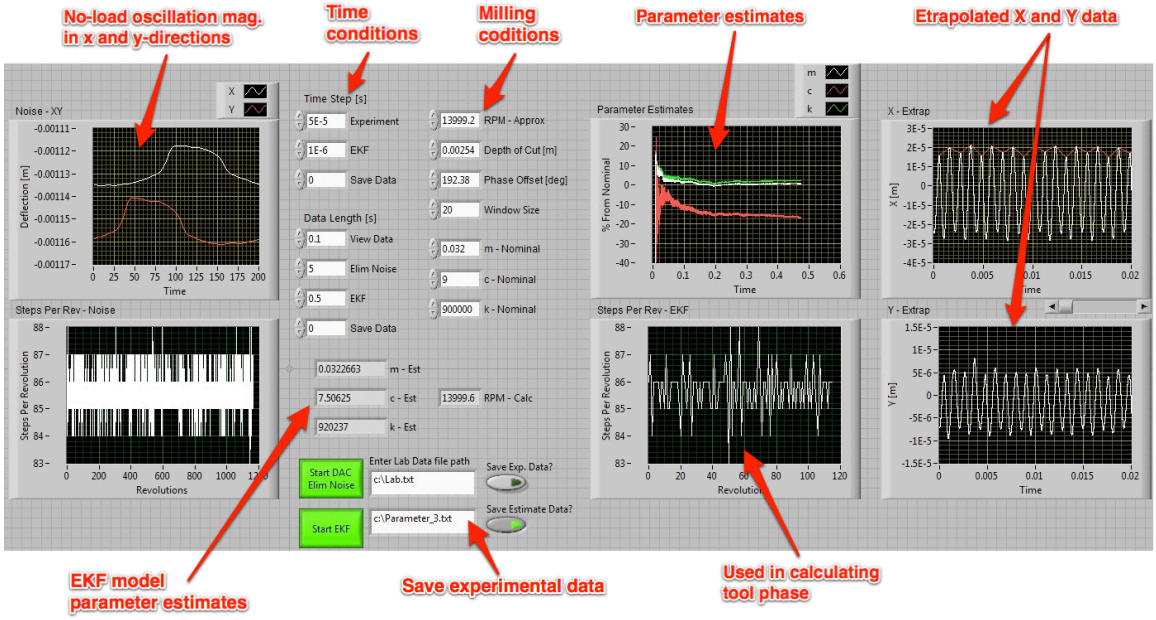

Fig. 71. Labview® VI used in collecting experimental data and estimating the model parameters online.

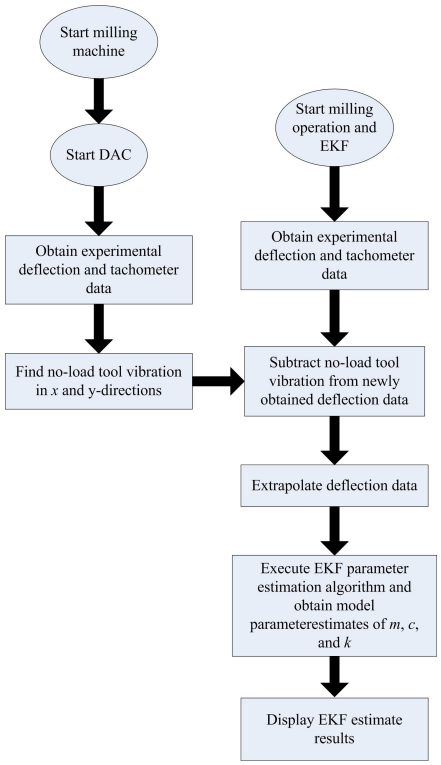

Fig. 72. Block diagram of the DAC system used in experimentally estimating model parameters during a milling operation.

Currently, the Labview® VI shown in Fig. 71 is only capable of estimating one set of parameter estimates. In future work, modifications should be made to allow estimates to be continually updated. In other words, after the first parameter estimation process is complete, a new section of experimental data should be collected and new estimates found. The second time the EKF algorithm runs, initial guesses for m, c, and k should be set equal to the parameter estimates found by the previous estimation process (this is true for any consecutive estimate). In addition, the Labview® VI in Fig. 71 should be optimized to reduce the computational time for a given set of parameter estimates, which will allow for more estimates to be calculated within a given time frame.

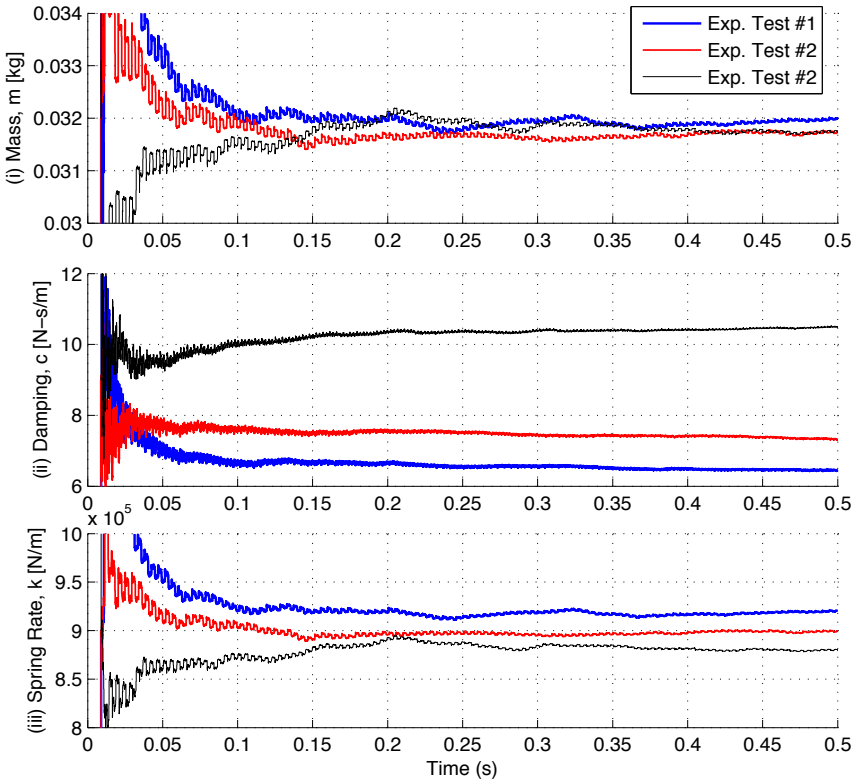

Fig. 73. On-line parameter estimates of (i) *m*, (ii) *c*, and (iii) *k* for experimental deflection data at *b* = 2.54 mm and *Ω* = 14,000 rpm. Parameter estimates for three experimental tests are given.

11.2.2 ON-LINE RMS CALCULATIONS

As discussed in Section 9.3, tracking the root-mean-square (RMS) value of the once-per-revolution tool deflection in the x-direction, X_m, can be used to indicate the onset of chatter vibrations. The average RMS value for a given revolution, rms_{rev}, is given in Eq. (62). When chatter does not exist, X_m values for each tool revolution at a given depth of cut, b, are the same (small variances do occur in experimental results); therefore, rms_{rev} is some small number. As chatter develops, the differences in the magnitude of X_m for each revolution begin to increase, resulting in a larger rms_{rev} value. Therefore, a threshold on the magnitude of rms_{rev} can be defined over which chatter vibrations are said to exist.

The Labview® VI given in Fig. 74 is used in collecting and analyzing small snapshots of experimental deflection and tachometer data to track rms_{rev} on-line. Once the average RMS value for the first snapshot of data is calculated, a new set of data is collected and an updated value of rms_{rev} is found (this process continues until the "STOP" button in Fig. 74 is pressed). For any value of rms_{rev} larger than the defined threshold value, a light (see Fig. 74) will turn from green to red indicating that chatter exists. Plots (i) and (ii) of Fig. 75 show the respective values of X_m and rms_{rev} for each RMS calculation over the length of an experimental test with an increasing b from 0 to 6 mm and Ω = 14,000 rpm. As shown from this figure, values of rms_{rev} increase as the variance in the X_m increase. In future work, proper threshold values for various spindle speeds should be found (the VI in Fig. 74 should also be optimized to reduce computational time). Once proper threshold values are found, tracking rms_{rev} on-line can indicate the onset of chatter for a variety of milling conditions. Preventive measures can

then be taken to reduce or eliminate the ill effects of chatter vibrations on the workpiece/tool.

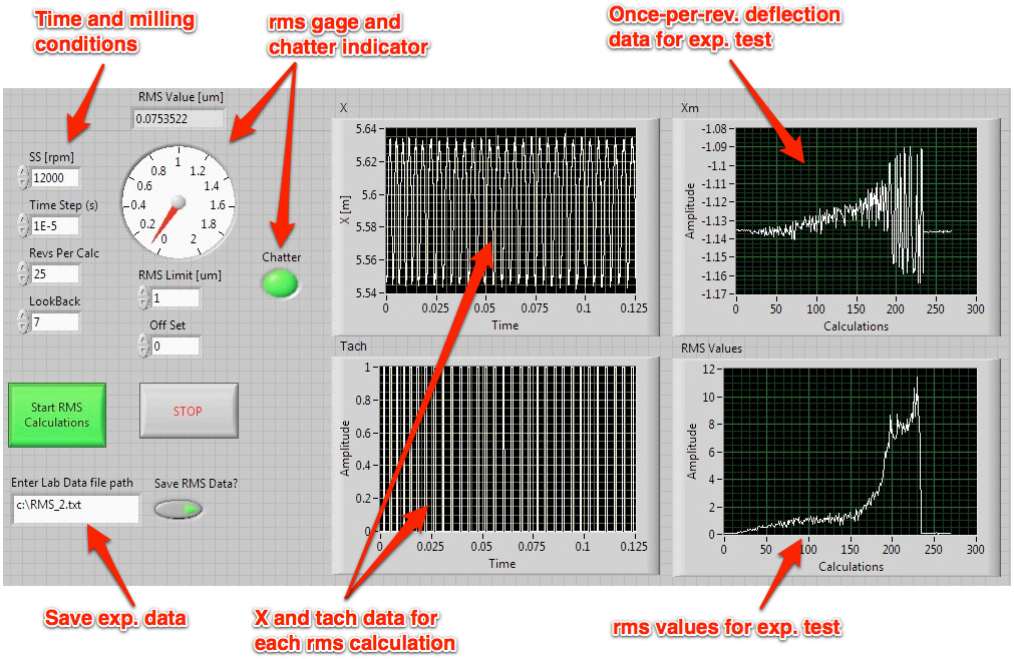

Fig. 74. Labview® VI used in tracking rms_{rev} on-line.

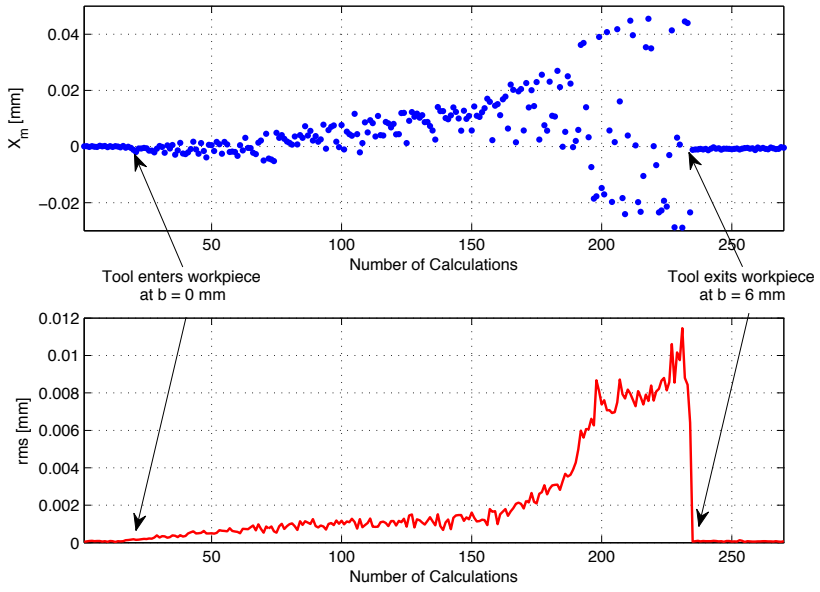

Fig. 75. (i) Experimental once-per-revolution deflection data, X_m, at each RMS calculation for and increasing b and Ω = 14,000 rpm. (ii) rms_{rev} values at each calculation.

11.2.3 PROPOSED SENSOR HOUSING

The sensor layout given in Section 4.1 is suitable for obtaining experimental tool deflections and the tool period in a lab setting. However, this layout cannot be used in any type of commercial machining operation. Aluminum chips cut from the workpiece during a milling operation can become attached to the capacitance sensors and/or tool causing errors in the sensor readings. Furthermore, most commercial machining operations use some type of coolant/oil to reduce tool and workpiece heat (this coolant could also affect sensor readings). Therefore, the sensors require protection from the machining environment. The schematic in Fig. 76 is a proposed sensor package capable of protecting the sensors from both metal chips and coolant. A metal housing is placed around spindle of the CNC machine and base of the milling tool. The capacitance and tachometer sensors are mounted inside this housing. The housing is to be air tight except for a small gap around the tool (see Fig. 76). The gap should be large enough so that the tool does not come in contact with the housing during large magnitude vibrations. The cavity of the housing is pressurized with air, resulting in high velocity air stream passing though the gap between the housing and the tool. This air stream will keep any chips and/or coolant away from the base of the tool where the sensor readings are taken. The distance the housing protrudes down from the base of the tool (i.e. where the tool and spindle meet) should be minimized so that the reach of the tool is not severely limited. The housing should also be designed such that the sensors and base of the tool can be easily accessed if needed. Furthermore, the schematic in Fig. 76 does not consider a method of grounding the tool, which is required when capacitance sensors are used in

measuring tool deflection. A more detailed design of this housing is required for proper integration into the CNC machine.

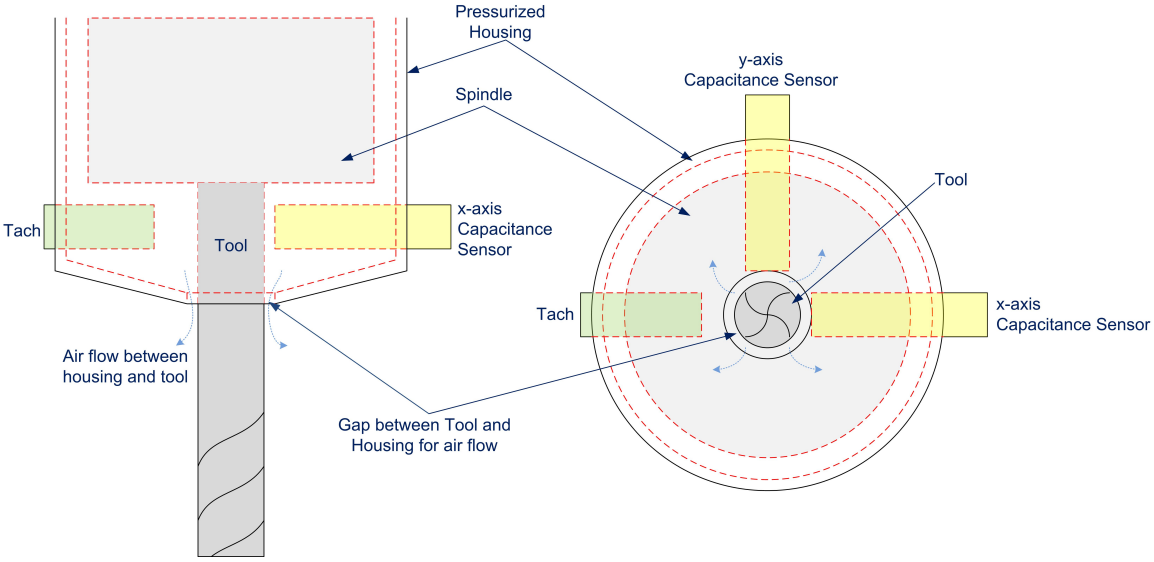

Fig. 76. Schematic of a proposed sensor package.

APPENDIX 1: BIFURCATION PLOTS

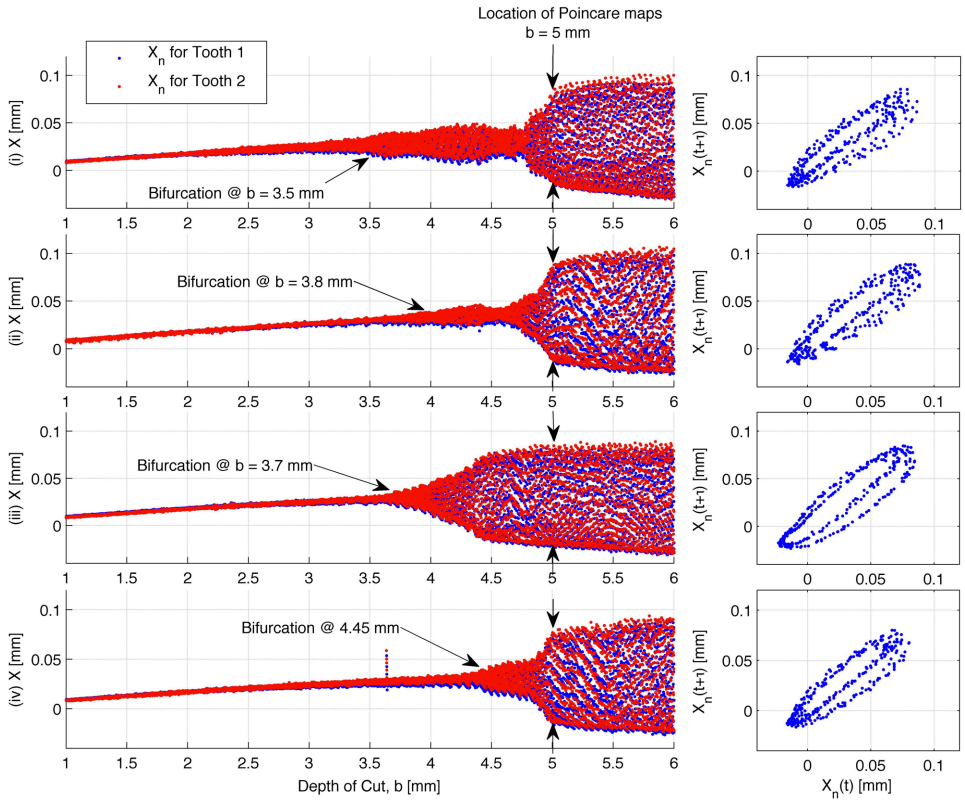

Fig. 77. Experimental once-per-tooth-pass tool displacement in the *x*-direction, X_n, for an increasing *b* and Ω = 14,000 rpm: (i) T.P. #1 - trial 1, (ii) T.P. #1 - trial 2, (iii) T.P. #2 - trial 1, (iv) T.P. #2 - trial 2. Poincaré maps at *b* = 5 mm are given to the right of each bifurcation diagram.

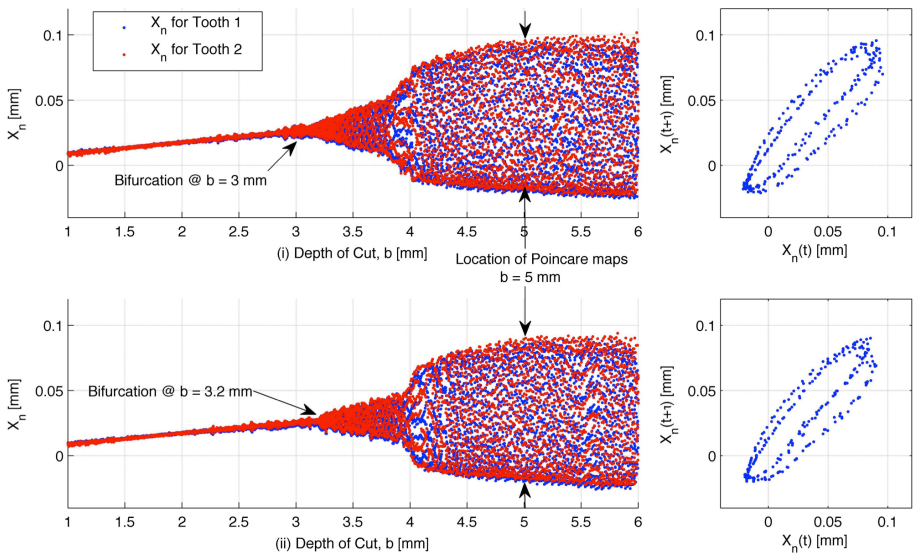

Fig. 78. Experimental once-per-tooth-pass tool displacement in the *x*-direction, X_n, for a decreasing *b* and Ω = 14,000 rpm: (i) T.P. #3- trial 1, (ii) T.P. #3 - trial 2. Poincaré maps at *b* = 5 mm are given to the right of each bifurcation diagram.

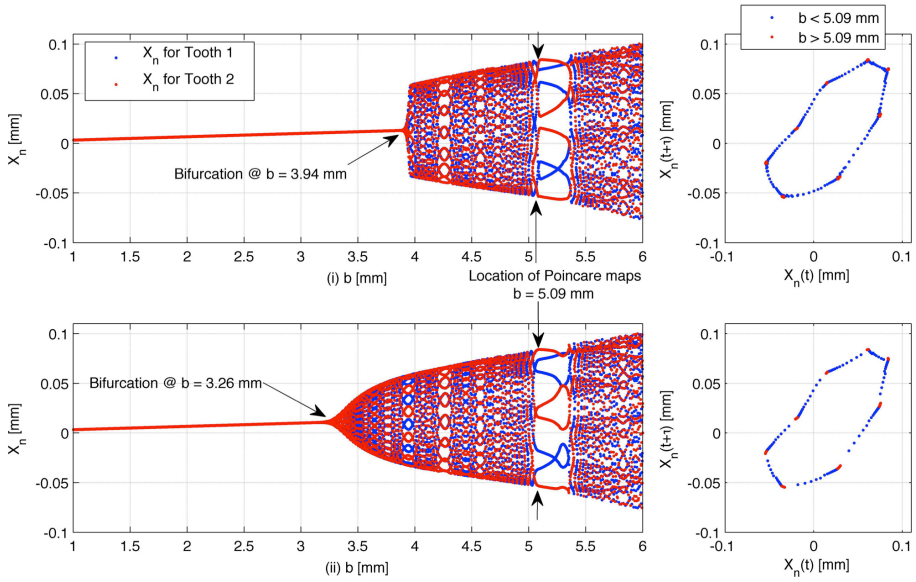

Fig. 79. Simulated once-per-tooth-pass tool displacement in the *x*-direction, X_n, with Ω = 14,000 rpm: (i) increasing *b* (ii) decreasing *b*. Poincaré maps at *b* = 5.09 mm are given to the right of the bifurcation diagrams. Model parameters used are the average EKF parameter estimates of the experimental results in Figs. 77 and 78 at *b* = 3 mm (*m* = 0.0287 kg, *c* = 9.4319 N-s/m, $k = 8.2671\times10^5$ N/m).

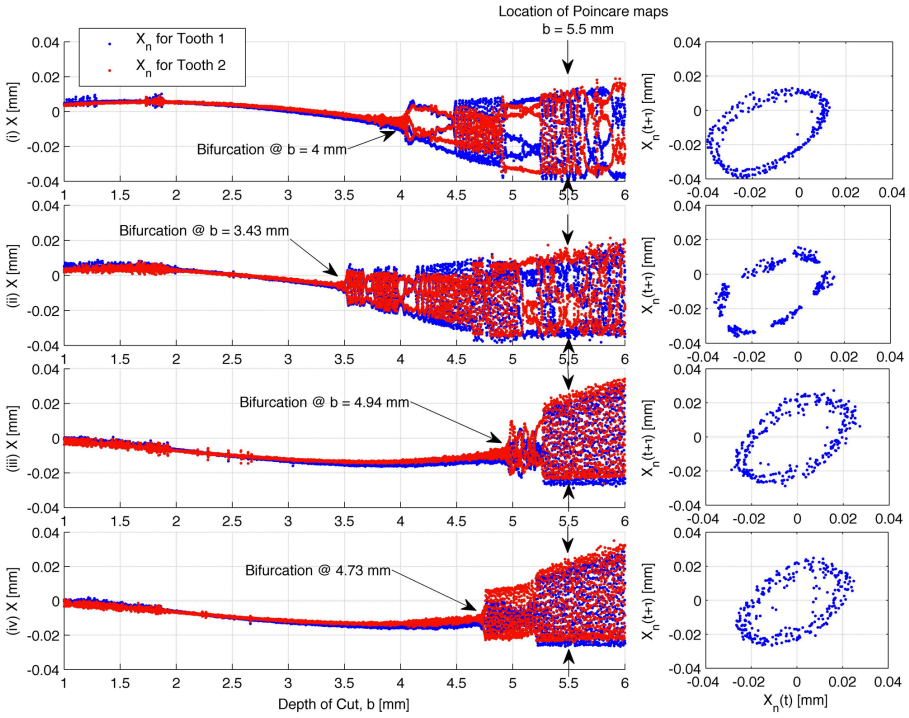

Fig. 80. Experimental once-per-tooth-pass tool displacement in the *x*-direction, X_n, for an increasing *b* and Ω = 10,000 rpm: (i) T.P. #1 - trial 1, (ii) T.P. #1 - trial 2, (iii) T.P. #2 - trial 1, (iv) T.P. #2 - trial 2. Poincaré maps at *b* = 5.5 mm are given to the right of each bifurcation diagram.

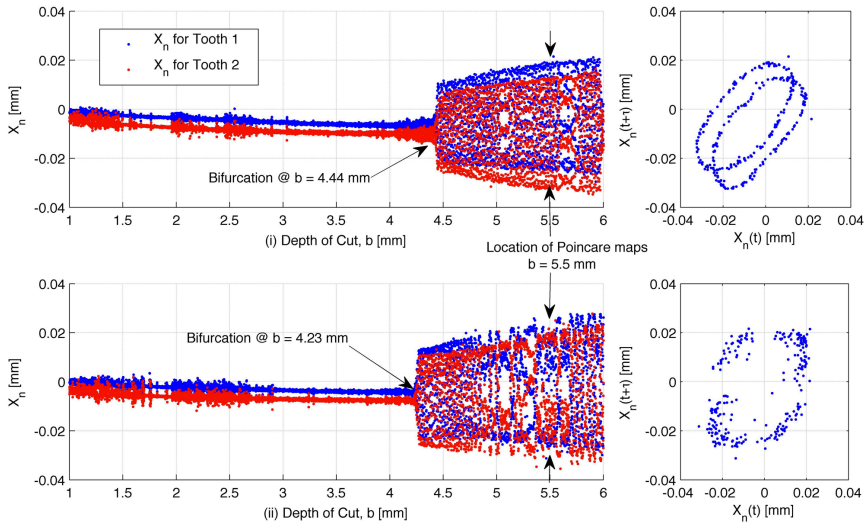

Fig. 81. Experimental once-per-tooth-pass tool displacement in the *x*-direction, X_n, for a decreasing *b* and Ω = 10,000 rpm: (i) T.P. #3- trial 1, (ii) T.P. #3 - trial 2. Poincaré maps at *b* = 5.5 mm are given to the right of each bifurcation diagram.

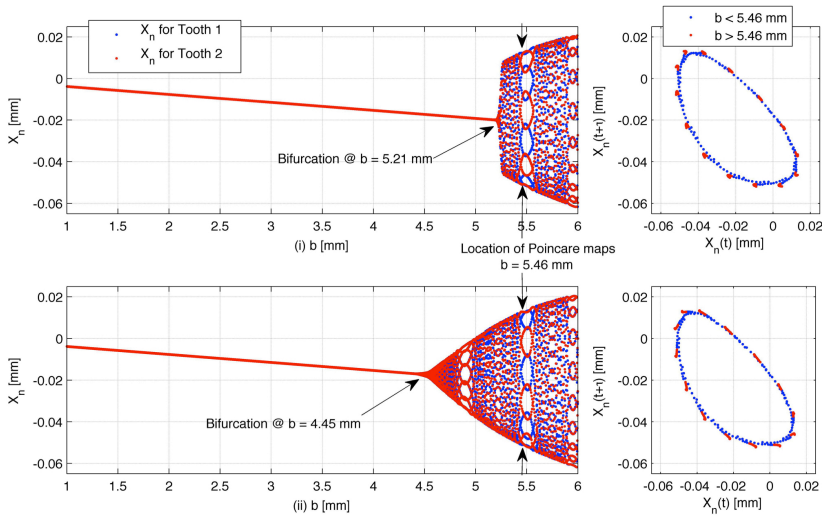

82. Simulated once-per-tooth-pass tool displacement in the *x*-direction, X_n, with Ω = 10,000 rpm: (i) increasing *b* (ii) decreasing *b*. Poincaré maps at *b* = 5.46 mm are given to the right of the bifurcation diagrams. Model parameters used are the average EKF parameter estimates of the experimental results in Figs. 80 and 81 at *b* = 3 mm (*m* = 0.0382 kg, *c* = 7.732 N-s/m, *k* = 10.540×10^5 N/m).

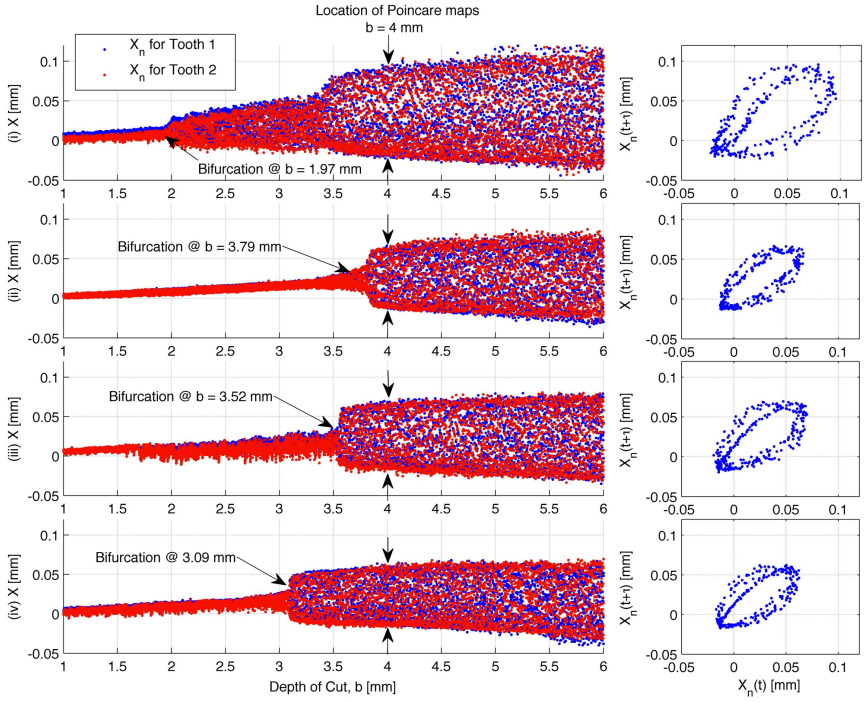

Fig. 83. Experimental once-per-tooth-pass tool displacement in the *x*-direction, X_n, for an increasing *b* and Ω = 9,500 rpm: (i) T.P. #1 - trial 1, (ii) T.P. #1 - trial 2, (iii) T.P. #2 - trial 1, (iv) T.P. #2 - trial 2. Poincaré maps at *b* = 4 mm are given to the right of each bifurcation diagram.

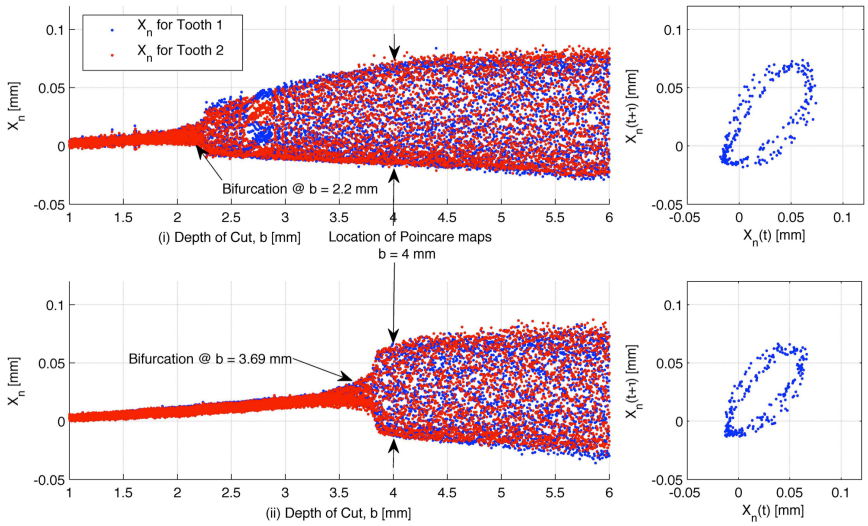

Fig. 84. Experimental once-per-tooth-pass tool displacement in the *x*-direction, X_n, for a decreasing *b* and Ω = 9,500 rpm: (i) T.P. #3- trial 1, (ii) T.P. #3 - trial 2. Poincaré maps at *b* = 4 mm are given to the right of each bifurcation diagram.

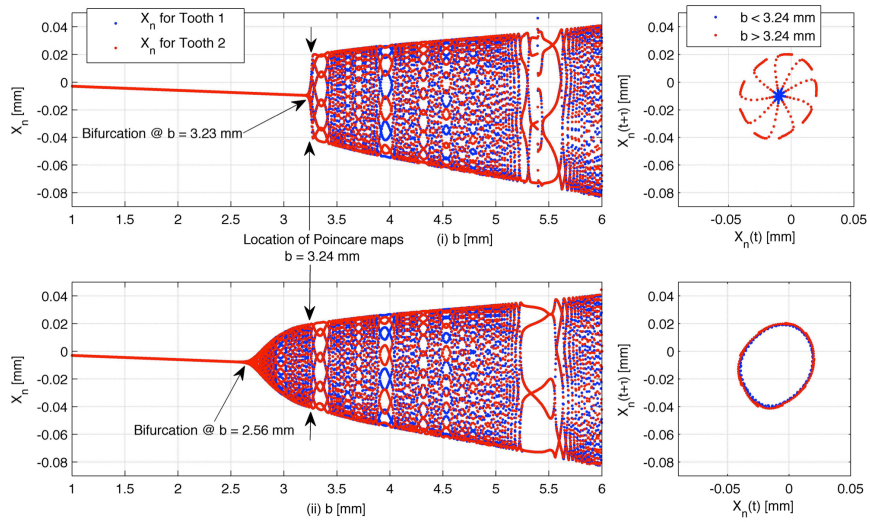

Fig. 85. Simulated once-per-tooth-pass tool displacement in the *x*-direction, X_n, with Ω = 9,500 rpm: (i) increasing *b* (ii) decreasing *b*. Poincaré maps at *b* = 3.24 mm are given to the right of the bifurcation diagrams. Model parameters used are the average EKF parameter estimates of the experimental results in Figs. 83 and 84 at *b* = 3 mm (*m* = 0.0316 kg, *c* = 7.6810 N-s/m, $k = 9.1036\times10^5$ N/m).

APPENDIX 2: EXP. PARAMETER ESTIMATES

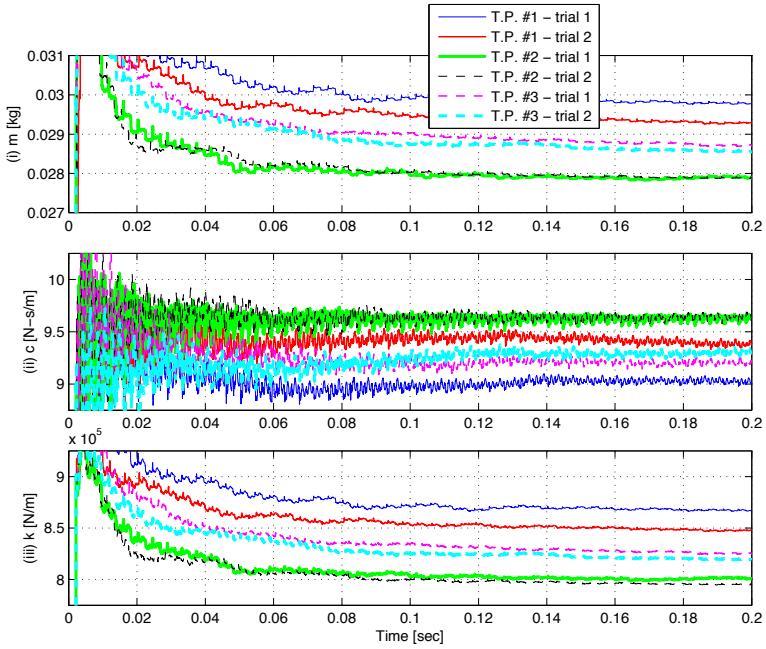

Fig. 86. Parameter estimates of *m*, *c*, and *k* from experimental deflection data at Ω = 14,000 rpm. Parameter estimates are given for two experimental trials from T.P. #1, #2, and #3 in Fig. 42 (6 tests total).

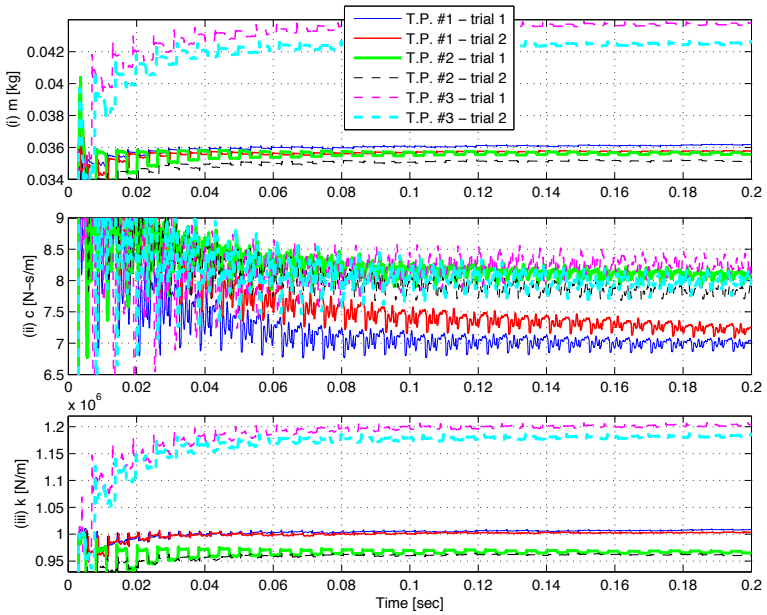

Fig. 87. Parameter estimates of *m*, *c*, and *k* from experimental deflection data at Ω = 10,000 rpm. Parameter estimates are given for two experimental trials from T.P. #1, #2, and #3 in Fig. 42 (6 tests total).

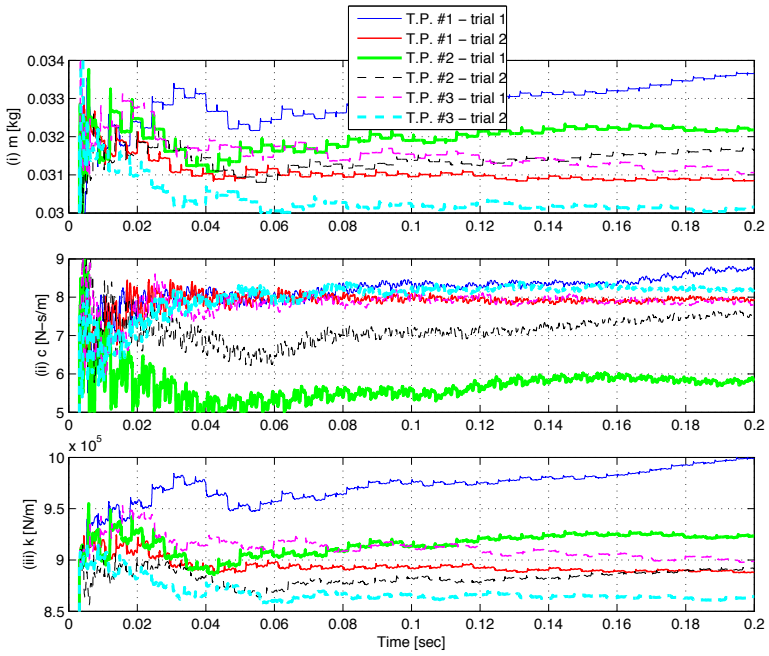

Fig. 88. Parameter estimates of *m*, *c*, and *k* from experimental deflection data at Ω = 9,500 rpm. Parameter estimates are given for two experimental trials from T.P. 1, 2, and 3 in Fig. 42 (6 tests total).

Bibliography

[1] J. Tlusty, A. Polacek, C. Danek, and J. Spacek, "Selbsterregte Schwingungen and Werkzuegmaschinen," *VEG Verlag Technik,* 1962.

[2] S. A. Tobias, *Machine Tool Vibration*. New York, NY: Wiley, 1965.

[3] P. V. Bayly, and B. P. Mann, "Effect of Radial Emersion and Cutting Direction on Chatter Instability in End-Milling," *ASME International Engineering Congress & Exposition,* Nov. 2002.

[4] E. Budak, and Y. Altintas, "Analytical Prediction of Chatter Stability in Milling – Part 1: General Formulation," *Journal of Dynamic Systems, Measurement, and Control,* vol. 120, pp. 22-30, 1998.

[5] Y. Altintas, and E. Budak, "Analytical prediction of stability lobes in milling," *CIRP Annals,* vol. 44, pp. 357-365, 1995.

[6] Y. Altintas, *Manufacturing Automation*, 1 ed. New York, NY: Cambridge University Press, 2000.

[7] Y. Altintas, "Analytical prediction of three dimensional chatter stability in milling," *JSME International Journal,* vol. 44, pp. 717-723, 2001.

[8] B. P. Mann, P. V. Bayly, M. A. Davies, and J. E. Halley, "Limit cycles, bifurcations, and accuracy of the milling process," *Journal of Sound and Vibration,* vol. 227, pp. 31-48, 2004.

[9] B. P. Mann, K. A. Young, T. L. Schmitz, and D. N. Dilley, "Simultaneous Stability and Surface Location Error Predictions in Milling," *Journal of Manufacturing Science and Engineering,* vol. 127, pp. 446-453, 2005.

[10] B. P. Mann, N. K. Gary, K. A. Young, and A. M. Helvey, "Milling Bifurcations from Structural Asymmetry and Nonlinear Regeneration," *Nonlinear Dynamics,* vol. 42, pp. 319-337, 2005.

[11] T. Insperger, B. P. Mann, G. Stépán, and P. V. Bayly, "Stability of up-milling and down-milling, part 1: Alternative analytical methods," *International Journal of Machine Tools and Manufacture,* vol. 43, pp. 25-34, 2003.

[12] A. Radhakrishnan, B. T. Edes, and B. P. Mann, "An experimental study of subcritical bifurcations in milling," in *in Proceedings of ASME Design Engineering 108 Technical Conferences & Computers and Information in Engineering Conference, DETC2007-34808, ASME*, Las Vegas, NV, 2007.

[13] A. Radhakrishnan, R. Fales, and B. P. Mann, "Milling Bifurcations: A Numerical Study," in *in Proceedings of ASME Design Engineering Technical Conferences & Computers and Information in Engineering Conference, no. DETC2009-86852, ASME*, San Diego, CA, 2009.

[14] A. Radhakrishnan, J. Kennedy, and R. Fales, "Experimental Study of Milling Bifurcations," presented at the SAMPE Fall Technical Conference, Wichita, KS, 2009.

[15] A. Radhakrishnan, "Effect of Chip Thickness, Sub-Critical Bifurcations and Process Parameters in High-Speed Milling," PhD Dissertation, Machanical and Aerospace Engineering, University of Missouri, Columbia, Columbia, MO, 2010.

[16] H. Merritt, "Theory of self-excited machine tool chatter," *Journal of Engineering for Industry,* vol. 87, pp. 447-454, 1965.

[17] W. Weck, E. Verhaag, and M. Gather, "Adaptive Control ofor Face-Milling Operation with Strategies for Avoiding Chatter-Vibrations and for Automatic Cut Distribution," *Annals of CIRP,* vol. 24-1, 1975.

[18] M. Gather, "Adaptive Grenzregelung Fur Das Strirnfrasen," Dr. Sc., Technischen Hochschule, Aachen, 1976.

[19] M. A. Davies, J. R. Pratt, B. Dutterer, and T. J. Burns, "Interrupted Machining: A Doubling in the Number of Stability Loabs, Part 1, Theoretical Development," *Journal of Manufacturing Science and Engineering,* 2001.

[20] P. V. Bayly, J. E. Halley, B. P. Mann, and M. A. Davies, "Stability of interrupted cutting by temporal finite element analysis," in *Proceedings of ASME Design Engineering Technical Conference, DETC/2001 VIB-21581*, Pittsburgh, PA, 2001.

[21] E. Budak, and Y. Altintas, "Analytical Prediction of Chatter Stability in Milling – Part 2: Application of the General Formulation to Common Milling Systems," *Journal of Dynamic Systems, Measurement, and Control,* vol. 120, pp. 31-38, 1998.

[22] J. Tlusty, and G. Andrews, "A Critical Review of Sensors for Unmanned Machining," *CIRP Ann.,* vol. 32, pp. 563-571, 1983.

[23] T. Delio, J. Tlusty, S. Smith, "Use of Audio Signals for Chatter Detection and Control," *Journal of Engineering for Industry,* vol. 114, pp. 146-157, May 1992 1992.

[24] S. Smith, and T. Delio, "Sensor-Based Control for Chatter-Free Milling by Spindle Speed Selection," in *Proceedings of the ASME 1989 Winter Annual Meeting*, 1989, pp. 107-114.

[25] S. Braun, "Signal Processing for the Determination of Chatter Threshold," *CIRP Ann.,* vol. 42, pp. 315-320, 1975.

[26] M. Rahman, "In-Process Detection of Chatter Threshold," *ASME J. Ind.,* vol. 110, pp. 44-50, 1988.

[27] J. W. Liang, "Damping Estimation via Energy-Dissipation Method," *Journal of Sound and Vibration,* vol. 307, pp. 349-364, 2007.

[28] N. D. Oliveto, G. Scalia., and G. Oliveto, "Dynamic Identification of Structural Systems With Viscous and Friction Damping," *Journal of Sound and Vibration,* vol. 318, pp. 911-926, 2008.

[29] T. Raïssi, N. Ramdani., and Y. Candau, "Set Membership State and Parameter Estimation for Systems Described by Nonlinear Differential Equations," *Automatica,* vol. 40, pp. 1771-1777, 2004.

[30] E. D. Blanchrd, A. Sandu, and C. Sandu, "A Polynomial Chaos-Based Kalman Filter Approach for Parameter Estimation of Mechanical Systems," *Journal of Dynamic Systems, Measurement, and Control,* vol. 132, Dec. 2010 2010.

[31] R. E. Kalman, "A New Approach to Linear Filtering and Prediction Problems," *Transactions ASME Journal of Basic Engineering,* vol. 82, pp. 35-45, 1960.

[32] R. E. a. R. S. B. Kalman, "New Results in Linear Filtering and Prediction Theory," *Transactions ASME Journal of Basic Engineering,* vol. 83, pp. 95-108, 1961.

[33] D. Simon, *Optimal State Estimation*. Hoboken, New Jersey: John Wiley & Sons, Inc, 2006.

[34] B. J. Brunell, D. E. Viassolo, and R. Prasanth, "Model Adaptation and Nonlinear Model Predictive Control of an Aircraft Engine," in *Proceedings of ASME Turbo Expo: Power for Land, Sea, and Air*, Vienna, Austria, 2004.

[35] P. a. O. L. Dewallef, "On-Line Performance Monitoring and Engine Diagnostic Using Robust Kalman Filtering Techniques," in *Proceedings of ASME Turbo Expo: Power for Land, Sea, and Air*, Atlanta, Georgia, USA, 2003.

[36] G. a. O. P. P. Jonsson, "An Application of Extended Kalman Filtering to Heat Exchanger Models," *Journal of Dynamic Systems, Measurement, and Control,* vol. 116, pp. 257-264, June 1994.

[37] K. D. Sebesta, N. Boizot, E. Busvelle, and J. Sachau, "Using an Adaptive High-Gain Extended Kalman Filter With a Car Efficiency Model," in *ASME Dynamic Systems and Control Conference*, Cambridge, Massachusetts, USA, 2010.

[38] V. A. a. S. D. Sujan, "Metric Based Dynamic Parameter Identification for Mobile Field Manipulator Systems," presented at the Design Engineering Technical Conferences and Computer and Information in Engineering Conference, Montreal, Canada, 2002.

[39] J. Tlusty, *Manufacturing Processes and Equipment*, 1 ed. Upper Saddle River, NJ: Prentice Hall, 2000.

[40] M. H. Kurdi, T. L. Schmitz, R. T. Haftka, and B. P. Mann, "Simultaneous Optimization of Removal Rate and Part Accuracy in High-Speed Milling," in *Proceedings of ASME International Mechanical Engineering Congress and Exposition, IMECE04*, Anaheim, CA, 2004.

[41] F. W. Taylor, "On the Art of Cutting Metal," *in Transactions of ASME,* vol. 28, pp. 31-350, 1907.

[42] F. C. Moon, *Dynamics and Chaos in Manufacturing Processes*. New York, NY: Wiley, 1998.

[43] D. J. Seagalman, and E. A. Butcher, "Suppression of Regenerative Chatter Via Impendance Modulation," *Journal of Vibration and Control,* vol. 6, pp. 243-256, 2000.

[44] G. Stépán, "Modeling Nonlinear Regenerative Effects in Metal Cutting," *Philosophical Transactions of the Royal Society,* vol. 259, pp. 739-757, 2001.

[45] S. a. K. Doi, S., "Chatter Vibration of Lathe Tools," *Transactions of the ASME,* vol. 78, pp. 1127-1134, 1956.

[46] H. K. Khalil, *Nonlinear Systems*. Upper Saddle River, NJ: Prentice Hall, 2002.

[47] M. A. Davies, J. R. Pratt, B. Dutterer, and T. J. Burns, "Stability Prediction for Low Radial Immersion Milling," *Journal of Manufacturing Science and Engineering,* vol. 124, pp. 217-225, 2002.

[48] B. P. Mann, T. Insperger, P. V. Bayly, and G. Stépán, "Stability of Up-Milling and Down-Milling, Part 2: Experimental Verification," *Int. J. Mach. Tools Manuf.,* vol. 43, pp. 35-40, 2003.

[49] W. J. Palm, *Mechanical Vibration*. Hoboken, NJ: John Wiley & Sons Inc., 2007.

[50] M. S. a. A. P. A. Grewal, *Kalman Filtering: Theory and Practice Using MATLAB*. Hoboken, New Jersey: John Wiley & Sons, Inc., 2008.

[51] E. Budak, "An Analytical Design Method for Milling Cutters With Non-constant Pitch to Increase Stability, Part 1: Theory," *ASME,* vol. 125, pp. 29-34, 2003.

[52] E. Budak, "An Analytical Design Method for Milling Cutters With Non-constant Pitch to Increase Stability, Part 2: Application," *ASME,* vol. 125, pp. 35-38, 2003.

[53] B. G. Lipták, *Instrument Engineers' Handbook: Process Measurement and Analysis*, 4th ed. vol. 1. New York: CRC Press, 2003.

[54] B. Sohns, J. Allison, H. K. Fathy, and J. L. Stein, "Efficient Parameterization of Large-Scale Dynamic Models Through the Use of Activity Analysis," in *Proceedings of the ASME IMECE 2006*. Chicago, IL, 2006.

[55] C. Taejun, Y. C. Shin, "On-Line Chatter Detection Using Wavelet-Based Parameter Estimation," *Journal of Manufacturing Science and Engineering,* vol. 125, pp. 21-28, Feb. 2003.

VITA

Joseph L. Kennedy was born November 19th, 1983 in St. Joseph, Missouri. He attended North Andrew R-6 High School in Rosendale, Missouri. In 2002 he entered Northwest Missouri State University in Maryville, Missouri and in 2004 transferred to the University of Missouri in Columbia, Missouri. He received a degree of Bachelor of Science in Mechanical Engineering with a minor in Mathematics from the University of Missouri in May, 2007. In August, 2007 He entered Graduate School at the University of Missouri. In May, 2009, he received a degree of Master's of Science from the University of Missouri. He then received a degree of Doctorate of Philosophy in Mechanical Engineering from the University of Missouri in May, 2011.

Permanent Address: 1414 County Rd. 125; Bolckow, MO; 64427

Phone Number: (573) 239-6015

Email: jlkz67@mail.missouri.edu